AN EUV SELECTED SAMPLE OF DA WHITE DWARFS FROM THE *ROSAT* ALL SKY SURVEY

Thesis submitted for the degree of
Doctor of Philosophy
at the University of Leicester.

by

Matthew C. Marsh
X-ray Astronomy Group
Department of Physics and Astronomy
University of Leicester

October 10, 1995

Declaration

I hearby declare that no part of this thesis has been previously submitted to this or any other University as part of the requirement for a higher degree. The work described herein was conducted by the undersigned except for contributions from colleagues as acknowledged in the text.

Matthew C. Marsh,
October 10, 1995

AN EUV SELECTED SAMPLE OF DA WHITE DWARFS FROM THE *ROSAT* ALL SKY SURVEY

Matthew C. Marsh

ABSTRACT

A detailed study of the sample of hot DA white dwarfs detected in the EUV and soft X-ray bands of the ROSAT all-sky survey is presented. Interpretation of the ROSAT data requires a priori knowledge of the temperature, gravity and visual brightness of all the white dwarfs detected. This information was obtained by a series of optical photometric and spectroscopic follow-up observations which are presented in detail. A by-product of this work is the mass distribution of the EUV selected sample of white dwarfs which shows an unexpectedly large proportion of high mass objects when compared with the optically selected population. It is suggested that this bias arises from the fact that hot white dwarfs with high gravities have lower heavy element abundances and are, therefore, more luminous (and easier to detect) than the lower gravity stars.

In keeping with earlier results, it is found that the majority of stars $< 40,000$K have more or less pure H atmospheres, while those above this temperature contain significant quantities of heavy elements. However, the increase size of the sample yields some important new results. A number of stars in the 40,000K to 50,000K range have nearly pure H atmospheres, a result at odds with the predictions of radiative levitation calculations. Furthermore, the dispersion in the observed EUV/X-ray opacity at a given temperature is much larger than expected from theory. An additional mechanism is then needed, other than radiative levitation and gravity, that can modify the atmospheric abundances. Finally, the expected strong dependence of opacity with surface gravity is not seen, except for very high mass stars.

Publications

Barstow, M.A., Fleming, T.A., Diamond, C.J., Finley, D.S., Sansom, A.E., Rosen, S.R., Koester, D., Marsh, M.C., Holberg, J.B. & Kidder, K., 1993, *Mon. Not. R. ast. Soc.,* **264**, 16
"ROSAT studies of the composition and structure of DA white dwarf atmospheres"

Barstow, M.A., Fleming, T.A., Diamond, C.J., Finley, D.S., Sansom, A.E., Rosen, S.R., Koester, D., Marsh, M.C., Holberg, J.B. & Kidder, K., 1993, In: *White Dwarfs: Advances in Observation and Theory*, Barstow, M.A., ed., Kluwer, Dordrecht, p. 147
"Photospheric composition and structure in DA white dwarfs"

Holberg, J.B., Barstow, M.A., Chen, A., Dreizler, S. Marsh, M.C., O'Donoghue, D., Sion, E.M., Tweedy, R.W., Vauclair, G. & Werner, K., 1993, *Astrophys. J.,* **416**, 806
"Two extrmely iron-rich hot DA white dwarfs and the nature of the EUV opacity"

Barstow, M.A., Holberg, J.B., Fleming, T.A., Marsh, M.C., Koester, D. & Wonnacott, D, 1994, *Mon. Not. R. ast. Soc.,* **270**, 499
"A ROSAT survey of hot DA white dwarfs in non-interacting binary systems"

Barstow, M.A., Holberg, J.B., Marsh, M.C., Tweedy, R.W., Burleigh, M.R., Fleming, T.A., Koester, D., Penny, A.J., Sansom, A.E., 1994, *Mon. Not. R. ast. Soc.,* **271**, 175
"RE 1738+665, the hottest DA white dwarf detected by ROSAT"

Barstow, M.A., Burleigh, M.R., Fleming, T.A., Holberg, J.B., Koester, D., Marsh, M.C., Rosen, S.R., Rutten, R.G.M., Sakai, s., Tweedy, R.W. & Wegner, G., 1995, *Mon. Not. R. ast. Soc.,* **272**, 531
"The orbital period of the pre-cataclysmic binary RE 2013+400 and a study of the atmosphere of the DAO white dwarf primary"

Marsh, M.C., Barstow, M.A., Holberg, J.B., O'Donoghue, D., Buckley, D.A., Fleming, T.A., Koester, D. & Burleigh, M.R., 1995, In: *White Dwarfs*, Koester, D & Werner, K, eds., Springer-Verlag, p. 328
"An EUV selected sample of DA white Dwarfs"

Marsh, M.C., Barstow, M.A., Holberg, J.B., Buckley, D.A., Penny, A.J., Sansom, A.E. & Koester, D., 1995, *in preparation,*
"An EUV selected sample of DA white dwarfs from the ROSAT all-sky survey. I: Optically derived stellar Parameters."

Marsh, M.C., Barstow, M.A. & Koester, D., 1995, *in preparation,*
"An EUV selected sample of DA white dwarfs from the ROSAT all-sky survey. II: Studies of the photospheric structure and composition."

Contents

List of Figures

List of Tables

Chapter 1

The Structure and Evolution of White Dwarfs

1.1 Introduction

White dwarfs constitute the most common end stage of non-explosive stellar evolution. They are formed when a progenitor star ceases burning helium and is not massive enough to induce carbon burning giving rise to gravitational collapse. Studies of globular cluster turn off points, (Reimers & Koester 1982; Weidemann & Koester 1983) have suggested an upper limit of $8M_{\odot}$ to the mass below which progenitors may lose enough material during their subsequent evolution for the stellar remnant to remain below the Chandrasekhar limit of $1.4M_{\odot}$ (Chandrasekhar 1931) and hence to enable non violent evolution into a white dwarf. If this is also the case for the disk population, the vast majority of stars in the Galaxy ($\approx$ 90% have masses $< 8M_{\odot}$; Koester & Weidemann 1980) will become white dwarfs. As they are by far the most dominant evolutionary channel, understanding the structure and compositional evolution of white dwarfs is therefore of great importance as they have the whole history of stellar formation imprinted on them.

As the star contracts toward the white dwarf stage the temperature rises dramatically with the very hottest white dwarfs being almost 200,000K and extensive mass loss, during several wind phases, results in a narrow peak in the white dwarf mass distribution of $\approx 0.6M_{\odot}$. The star is prevented from further collapse only when the core (which contains 99% of the white dwarf mass) becomes completely degerate at a radius $\sim 10^{-2}R_{\odot}$ resulting in a very high density and therefore high surface gravity (typically log g= 8.0). The white dwarfs then cool rapidly as there is no major source of energy production, taking around 5 million years to cool to 50,000K, and a further 5 billion years to reach 5,000K. In doing so, the core will first liquify and then, after about 3 billion years, will begin to crystallise, eventually fading beyond detection thresholds into obscurity for the remaining lifetime of the Universe.

Interestingly, the white dwarf luminosity function (the number density of white dwarfs observed per unit absolute luminosity) shows a shortfall in the numbers of the coolest, oldest white dwarfs at luminosities in the region $-4.2 \geq \log(L/L_{\odot}) \geq -4.6$ (Liebert, Dahn & Monet 1988). Modelling this absence of the faintest objects with white dwarf cooling models provides an estimate of the Galactic age of $7 - 10$Gyrs (Winget *et al.* 1987; Wood 1992) which is difficult to reconcile with the age of $13 - 18$Gyrs derived for globular clusters, from fitting theoretical isochrones to globular cluster colour-magnitude diagrams. Thus, white dwarfs not only provide constraints on previous stages of stellar evolution but as they are among the oldest objects, they also provide a historical record of the evolution of the local region of the Galaxy.

In addition to their important role in the understanding of stellar and Galactic evolution, white dwarfs provide a platform in which to investigate the behaviour of matter under extreme physical conditions, particularly high pressure. In comparison to normal main sequence stars the composition of all hot white dwarf photospheres (which are non-degenerate) appears rather peculiar in that they are predominantly hydrogen and/or helium with only minute traces of heavier elements present. The main process causing this effect is gravitational separation (Schatzmann 1958) where the extremely high gravitational field, in the absence of competing processes, causes the heavier elements to sink below the photosphere on a very short timescale. However, the launch of the *International Ultraviolet Explorer* (IUE) revealed that, at least in some stars, heavier elements were more abundant than was first thought. In reality, gravitational stratification may be slowed or stopped by radiation pressure. Other physical processes such as diffusion, convection, mass-loss and accretion from the interstellar medium (ISM) can all change the composition of the outer layers, even after trace elements have sunk below the photosphere.

A thorough understanding of the affects of these processes on the compositional evolution of white dwarfs requires measurements of the abundances of trace elements in their atmospheres. EUV ($\approx 100 - 1000$ Å) and X-ray ($\approx 0.1 - 100$ Å) observations are crucial in this field as hot white dwarfs have the peak of their emission in these energy bands. Also, many important absorption lines and edges occur at these energies making the presence of an opacity source in a hydrogen rich atmosphere, be it helium or heavier elements, readily apparent in the EUV/X-ray region of the spectrum. Due to the relatively low opacity of hydrogen in the EUV, photons at these energies come from much deeper layers in the atmosphere than optical photons (Shipman 1976). Hence, these high energy observations could also be used to probe the structure of the atmosphere. Previous studies of EUV observations from the *Einstein* (Kahn *et al.* 1984; Petre, Shipman & Canizares 1986) and *EXOSAT* (Jordan *et al.* 1987; Paerels & Heise 1989) satellites demonstrated that some opacity source, assumed to be helium was present in the atmospheres of some hydrogen rich white dwarfs with higher abundances in the hotter stars. However, these works were limited in detail due to the small samples of objects available. Also, the spectral resolution of these instruments was insufficient to distinguish between models with different physical structures. An alternative interpretation is a stratified atmosphere, where a thin layer of hydrogen lies on top of a helium layer. The opacity then arises from the helium at the diffusion boundary as the EUV/X-ray photons originate in this region. Alternatively, the hydrogen layer may be very thick ($\geq 10^{-4}M_{\odot}$) as predicted by evolutionary calculations (Iben & Tutukov 1984) with processes such as radiative levitation lifting trace elements into the hydrogen layer. The thickness of the hydrogen layer is a very important parameter as the observed changes in the ratio of hydrogen-rich to helium-rich objects descending the cooling sequence can only be explained by some DAs having extremely thin layers ($\leq 10^{-15}M_{\odot}$).

The launch of ROSAT in 1990 provided an important opportunity to investigate in more detail the nature of trace elements in hydrogen rich white dwarf atmospheres. During the first six months of operation it performed the first EUV/X-ray all-sky-survey resulting in over a four fold increase in the number of DA white dwarfs detected in this spectral range with more than 50 new identifications. Such a large sample selected purely on the criteria of detection in the EUV gives the best opportunity to date for studying the behaviour of the opacity sources and significantly improves the statisitical basis of any composition/T_{eff} correlation. Also, the photometric bands available during the ROSAT survey have improved spectral resolution over the EXOSAT low energy instrument, yielding tighter constraints on the physical structure.

Presented here is a detailed analysis of 89 of the 110 DAs detected in the ROSAT survey, details of which together with the reduced EUV/X-ray count rates are presented in the next chapter. In order to utilize the ROSAT data, accurate estimates of the effective temperature and surface gravity, together with the apparent visual magnitude are required for each object. Unlike previous works (e.g. Barstow *et al.* 1993) which only selected detections of stars for which these optically derived parameters were already known, a follow up program of spectroscopic and photometric observations ensured that the sample presented here was a complete EUV sample limited only in optical brightness down to V $\approx$ 17. The optical observations and reductions are described in chapter 3. The bulk of the investigation into the structure and composition of the atmospheres by computer modelling is then given in chapter 4 with the final chapter being a summary of the results and an insight into the future work that is required.

1.2 Basic Structure of White Dwarfs

White dwarfs consist of a degenerate core containing carbon and oxygen (from earlier nuclear burning stages, Paczynski 1970) which accounts for 99% of the white dwarf mass. For all but the coolest white dwarfs, the core is a plasma consisting of ions and degenerate electrons. The degeneracy pressure of the electrons is the main force balancing gravitational collapse as the thermal pressure of the ions is negligible in comparison (Fowler 1926). Thus, when considering the pressure balance and hence the physical structure, to a first approximation the ions may be ignored. As the electrons are degenerate, and hence their pressure is only a weak function of temperature are much less massive than the ions they hold very little of the thermal (kinetic) energy. The majority of the thermal energy is due to the non-generate ions. Therefore, the gross physical structure may be separated from the problem of cooling which involves calculating the energy release through the non-degenerate atmosphere. As a result of this, the gross physical structure of the core was well understood over half a century ago (Chandrasekhar 1939). Subsequent work has been in the form of minor corrections to the equation of state. A detailed description of the core physics is out of the scope of this thesis but for a review see Shapiro & Teukolsky (1983).

In the very hottest part of the cooling sequence, shortly after the white dwarf has formed, neutrino loss is the dominant cooling process with about twice as much energy being lost than through normal radiation. By $\log(L/L_\odot) \approx -2.2$ and $T_{eff} \approx 15,000$K, the neutrino flux will have fallen to about 1% of the total (Wood 1990). When the star has cooled to around $4,000 <$

$T_{eff} < 10,000$K at $-4.5 < \log(L/L_{\odot}) < -3.0$ the core undergoes crystallisation which slows the cooling rate temporarily until the phase change is complete. However, ROSAT is only sensitive to objects hotter than $\approx 20,000$K so the major loss of energy for the sample of white dwarfs presented here is through the release of electromagnetic radiation.

The remaining 1% of the mass which comprises the non-degenerate outer layers consists of hydrogen and helium left over after the star ejected most of its atmosphere during pre-white dwarf evolution. Paradoxically, while all that can be seen of a white dwarf is its photosphere, it is the photosphere which is the least understood. The photon energy distribution of the radiation from the core is essentially that of a blackbody. However, the shape of the observed spectrum is dictated by the structure and composition of the atmosphere. Hence, in theory, observations in any waveband may be used to reveal these parameters. In practice, as the greatest redistribution of energy occurs in the EUV due to the presence of many absorption features in this region, EUV observations have proved useful in revealing the presence of trace elements.

1.3 Spectral Classification

The increasing discovery of hybrid compositions in what was previously thought to be pure hydrogen or pure helium atmospheres, mainly through the advent of ultra-violet spectroscopy, led to a revision of the system of spectral classification first presented by Greenstein (1960). The new nomenclature in accepted use today, which is a formalised and more logical version of the old system, was introduced by Sion *et al.* (1983). The white dwarfs are classified according to the presence and strength, of absorption lines in their spectra. All the spectral classes are prefixed by an upper-case D which stands for degenerate. Following this is another upper-case letter representing the primary or dominant spectroscopic features observed in the optical spectrum. There may then follow a series of upper-case letters denoting secondary and then any other notable spectral features in order of significance from any part of the electromagentic spectrum. The criteria for the letters is that the spectral class they describe should be close to the main sequence class of the same letter. For example, DAO describes white dwarfs with strong Balmer lines in their optical spectrum (Main Sequence class A) but also weak HeII lines (Main Sequence class O). Following the letters there may also be a temperature index from

Table 1.1: Summary of Major White Dwarf Classifications

Spectral Class	Temperature Range* (K)	Spectral Characteristics
DA	$6,000 - 88,000$	Only Balmer lines; no HeI or metal features
DAZ	$6,000 - 80,000$	Balmer lines; weak metal features present
DAO	$> 50,000$	Balmer lines; weak HeII lines also present
DO	$45,000 - 100,000$	HeII strong; HeI or H present
DOZ	$45,000 - 100,000$	HeII lines; weak metal features present
DB	$12,000 - 28,000$	HeI lines; no H or metals present
DBZ	$12,000 - 28,000$	HeI lines; weak metal features present
DBA	$12,000 - 30,000$	HeI lines; weak Balmer lines present
DQ	$6,000 - 12,000$	C features (atomic or molecular), in any part of spectrum
DZ	$< 6,000$	Metal lines only; no H or He features
DC	$< 6,000$	Featureless – no lines deeper than 5% in any part of spectrum

* *Approximate* temperature range each class has been observed in.

0 to 9 defined by $10 \times \theta_{\rm eff}$ (where $\theta_{\rm eff} = 5040/T_{eff}$) with the temperature most often being determined from broad band colour measurements (e.g. Greenstein 1984). Any degenerate star cooler than 5,500K would have the index 9 for temperature. Appropiate symbols may also be present indicating magnetic fields/polarization, variability and spectral peculiarites. The main spectral calsses are summarised in table 1.1 which also shows the approximate range in T_{eff} over which the classes have been observed.

1.4 Evolution from the Main Sequence

As outlined in the introduction, white dwarf progenitors are believed to include all stars with an initial mass less than $\approx 8M_\odot$. When the hydrogen in the core becomes depleted for a main sequence star, shell burning of hydrogen becomes the main energy source. Since the core no longer produces significant luminosity this naturally results in its collapse (Schönberg & Chandrasekhar 1942). The onset of shell burning may provide ~ 100 times the luminosity of the core and the star expands by a factor between one hundred and one thousand. This results in cooling of the outer layers and it becomes a red giant. This is illustrated in figure 1.1 which shows a schematic of the Hertzprung-Russell diagram detailing the post Main Sequence evolutionary

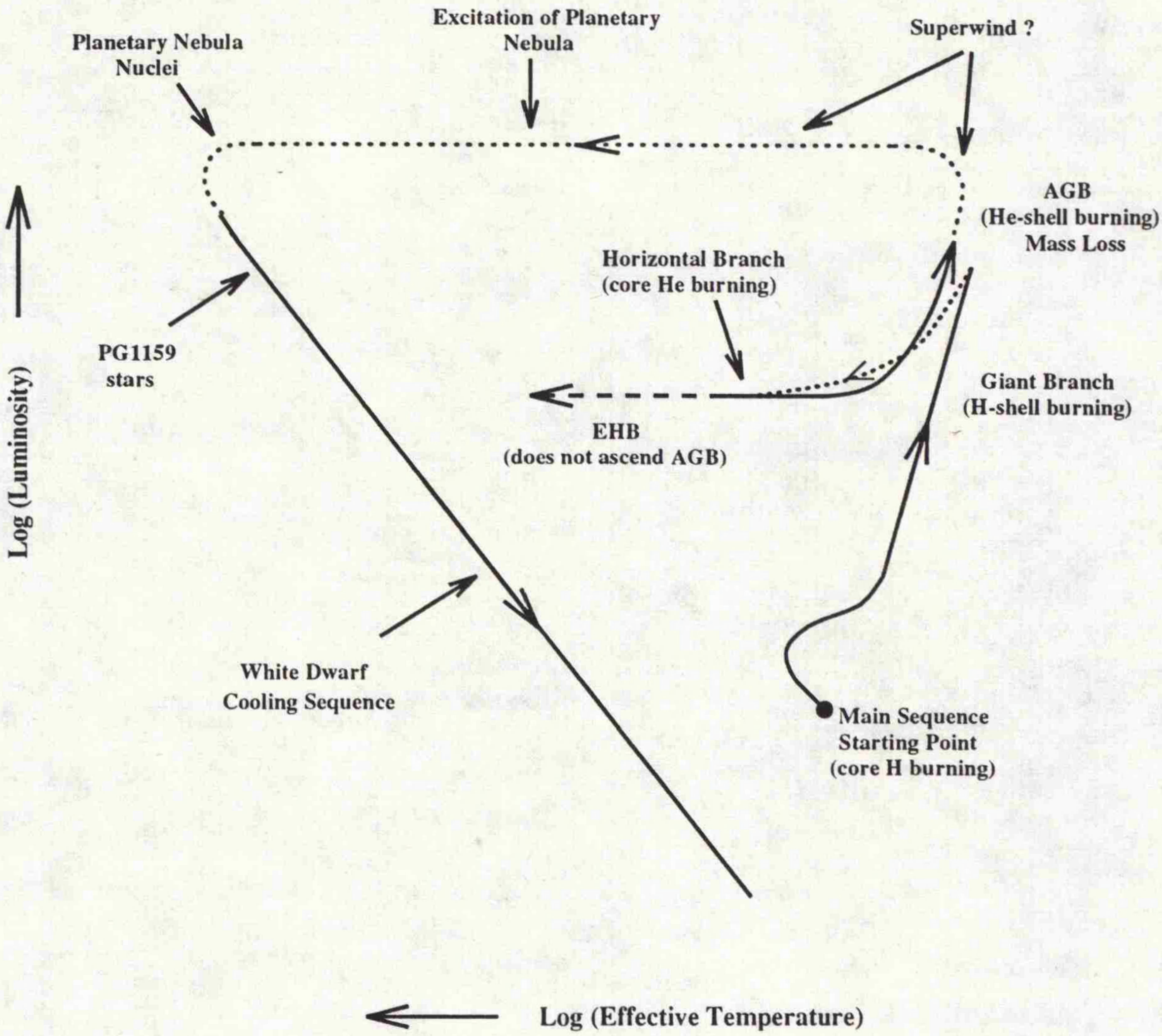

Figure 1.1: Schematic view of the Hertzsprung-Russell Diagram showing the evolutionary paths of stars from the Main Sequence to the white dwarf stage. Labels show various important stages as discussed in the text. (AGB = Asymptotic Giant Branch; EHB = Extended Horizontal Branch).

paths of stars toward the white dwarf stage. During this phase, the core ceases to collapse once it reaches a high enough temperature to initiate the fusion of helium into carbon and oxygen. In intermediate sized stars, this occurs before the core has collapsed to a density high enough to become degenerate. However, for low mass stars the density of the core has risen sufficiently that it is partially degenerate before helium ignition occurs. As pressure is only weakly dependent on temperature for non-relativistic degenerate matter, the core does not readily expand as it would if it were a perfect gas and this leads to a thermal 'runaway' effect (the helium flash) which only ceases when the temperature rises sufficiently to lift the degeneracy. The core then expands, slowing the fusion rate and causing the atmosphere to shrink rapidly, thus moving onto the horizontal branch.

After a prolonged period of stability, a similar process occurs once the core helium is exhausted. Helium burns in a shell around a carbon/oxygen core and the star moves to the right of the HR-diagram onto the Asymptotic Giant Branch (AGB). However, near the top of the AGB the shell helium becomes depleted and the star begins to undergo radial thermal pulsations and residual hydrogen again begins fusing in the outer atmosphere. Subsequently, for reasons that are not well understood, the star becomes unstable and much of the remaining atmosphere is ejected (to be later observed as a planetary nebula). First attempts to explain this focussed on an almost instantaneous ejection $\sim 1-10$ yrs caused by large scale envelope instabilities. However, later dynamical studies failed to produce quantitative agreement with observations. Instead, the growing view in recent years is that the atmosphere is removed via one or more types of stellar wind. Several observational lines of evidence indicate that red giants can support a stellar wind mass loss rate (MLR) up to $\sim 10^{-6} M_{\odot}\,yr^{-1}$, although the physical mechanisms driving the winds are poorly understood (Reimers 1981). From estimates of the mass, radius and expansion velocity of planetary nebulae, Renzini & Voli (1981) estimated a lower limit to the MLR during nebula formation of $\sim 10^{-5} M_{\odot}\,yr^{-1}$, an order of magnitude higher than that indicated above. To account for this difference, Iben & Renzini (1983) postulated the existence of a 'superwind' which operates on a very short timescale ($\sim$ 1000 yrs) and is assumed to be caused by a different mechanism to the wind which operates for most of the AGB phase. While producing models of the evolution of white dwarfs from the AGB, Schönberner (1983) also found it necessary to include a superwind in order to reduce the predicted lifetime on the AGB to observed values.

As the above processes provide the material which will become a planetary nebula, the core of the star contracts under gravity until it is halted by degeneracy pressure. During contraction, it heats up and, therefore, moves to left of the HR diagram at constant luminosity. During this time the surface gravity increases by a factor of over 10^4 and the temperature rises to $\sim 100,000$K. Once the photosphere has heated to a sufficient temperature ($\approx 30,000$K) the emergent flux significantly ionizes the ejected envelope rendering it observable as a planetary nebula with the degenerate core being the planetary nebula nucleus (PNN). The surrounding nebula continues to expand until after $\approx 25,000$ yr it becomes so sparse that it is no longer visible which formally ends the PNN stage and the core has essentially becomes a hot white dwarf.

Assuming the main energy source during the evolution from the high luminosity phase PNN to the white dwarf stage is due to hydrogen shell burning, Iben (1984) has shown that the remnant hydrogen layer mass must be greater than $\approx 10^{-4}M_{\odot}$. If less than this, the lifetime of the high luminosity – high surface temperature phase would be reduced to no more than a few hundred years. Hence, all DA white dwarfs should be born with hydrogen layer masses greater than $\approx 10^{-4}M_{\odot}$ according to 'standard' evolutionary calculations. Hydrogen shell burning may then continue to contribute to the white dwarf luminosity, the magnitude depending on the thickness of the surface hydrogen layer (see Koester & Schönberner 1986). Once residual nuclear burning ceases there is no energy release to maintain the temperature and the hot core will cool into obscurity on a thermal timescale taking $\sim 10^5$yrs.

1.4.1 Evolution Along the EHB (Subdwarfs)

The course of evolution described above is that for the majority of main sequence stars ($\approx 1 - 8$ $M_{\odot}$). However, for the lowest mass stars which are still capable of core helium burning (subdwarfs) the situation is somewhat different. Once the core helium is exhausted, these stars do not ascend the AGB as they have not retained enough envelope mass ($M_e \gg 0.02M_{\odot}$) to support a double shell source phase. Instead they contract at constant luminosity (along the Extended Horizontal Branch EHB, Heber 1986; Caloi 1989) due to release of gravitational energy until degeneracy pressure halts the collapse and they become a white dwarf.

Subdwarfs are observed to have either hydrogen rich atmospheres (sdB), helium rich atmospheres (sdO) or an intermediate composition (sdOB, Hunger *et al.* 1981). The sdBs have temperatures up to $\approx 35,000$K while the sdOs are considerably hotter ($T_{eff} < 100,000$K). Observationally, the main observational difference between white dwarfs and subdwarfs is that the surface gravity of subdwarfs is lower (log g=5-6 cf. log g=7-8), producing narrower Balmer lines in their spectra, and they have higher absolute magnitudes due to their larger radii.

The absence of helium in many subdwarfs is presumably due to gravitational settling in their relatively high gravity (log g $\sim 5-6$) atmospheres (Greenstein & Sargent 1974). They therefore seem to be direct progenitors of low mass DAs. However, based on space densities, Drilling & Schönberner (1985) showed that the birthrate of sdBs and sdOBs suggests that they account for only 2% of all DA white dwarfs, and even then only contribute to the lowest mass tail of the white dwarf mass distribution. However, helium rich sdO stars do exist and are possible progenitors of DO white dwarfs. Since they are the hottest subdwarfs, mass loss may play a significant role in removing any remaining surface hydrogen. Once again, however, the derived birthrate of these objects is significantly lower than that for helium rich PNN suggesting they play a minimal role in DO formation (Drilling & Schönberner 1985; Heber 1986). However, the space densities and birth rates for subdwarfs are deduced from small, incomplete samples. While the birthrates of PNN and white dwarfs are estimated to be comparable, the most common objects found in colour selected, magnitude limited surveys such as the Palomar Green (Green, Schmidt & Liebert 1986) are the hot subdwarfs suggesting their contribution to the numbers of white dwarfs could possibly be larger.

1.5 The White Dwarf Cooling Sequence

One of the major outstanding problems in the study of white dwarfs is their division into two distinct categories, having either hydrogen-rich atmospheres (DA) or helium dominated atmospheres (non-DA), and the routes by which they evolve from possible progenitors. Although the evolutionary channels appear independant there are several observational facts which suggest that some interaction between the two must occur. Figure 1.2 shows a schematic of the whole of the white dwarf cooling sequence highlighting some of this evidence together with possible physical processes which have been suggested to explain the changes from one branch to the other.

Studies of the luminosity function of PNN show that He-rich objects are approximately as common as H-rich stars whereas the white dwarf luminosity function indicates that in the region above $\approx 40,000$K the DA:non-DA ratio is $\approx 7:1$ (Fleming, Liebert & Green 1986). This can only be accounted for by DO stars turning into DAs.

The hottest DA yet discovered (as a by-product of this work) is RE1738+665 with a temperature of $85,400\text{K} - 90,400\text{K}$ (see Barstow *et al.* 1994; chapter 3). This is significantly cooler than the hottest known helium rich white dwarfs (known as the PG1159 stars after the prototype PG1159-035) which have $T_{eff} \geq 10^5\text{K} - 10^{5.2}\text{K}$. These objects are all of the class DOZ and exhibit OVI absorption features at 3311Å, 3434Å, 3811Å and 3834Å together with features of CIV at 3689Å, 3934Å and 4658Å. Such spectral features are associated in strong emission with the OVI class of PNN suggesting a direct link between the two. The evidence for such a link is strengthened by the identification of several PNN as PG1159 stars (Napiwotzki & Schönberner 1991). For the DA stars, there is no similar class of object connecting them to their progenitors, the H-rich PNN, giving rise to the 'DA gap'. Although RE1738+66 has a temperature high enough to be considered a direct descendant of H-rich PNN (which have temperatures $> 100,000$K) it is the only DA within this temperature range. The next hottest DAs all have temperatures less than $\approx 70,000$K and even then are relatively few. However, there are several hot stars, the DAOs, with hydrogen dominated atmospheres but which also show spectroscopically detectable abundances of helium. They have temperatures up to $\approx 80,000$K suggesting they could be the evolutionary link between the DO and the DA stars. However, Bergeron *et al.* 1994 suggest that this is not so, and that most DAOs evolve from the horizontal branch.

The most compelling evidence for transitions between the DA and non-DA cooling channels is the apparent absence of He-rich stars between the coolest known DO at $\approx 45,000$K and the hottest known DB at $\approx 28,000$K giving the 'DB gap'. This gap is almost certainly real and not a result of observational selection effects (Wesemael, Green & Liebert 1985; Liebert *et al.* 1986). Even though HeII line strengths decrease with decreasing temperature, there is theoretically no temperature at which neither HeII or HeI lines will be visible. At $T_{eff} < 25,000$K, the DB white dwarfs are numerous, accounting for $20-25\%$ of all white dwarfs hotter than 12,000K. Below 10,000K the non-DA degenerates are of the order of half the entire population of white dwarfs (Sion 1984; Greenstein 1986).

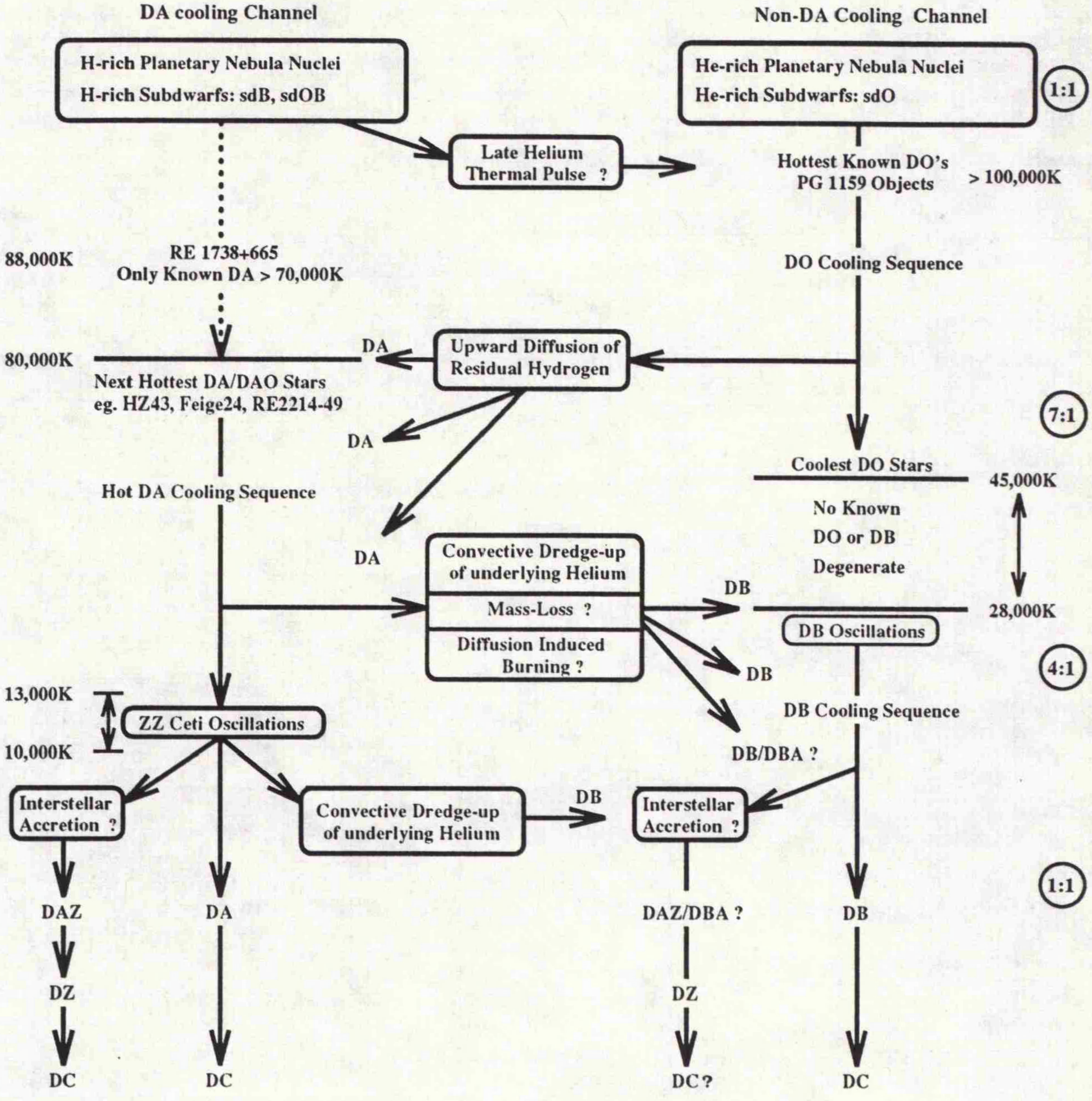

Figure 1.2: Schematic view of the White Dwarf cooling sequence. The hydrogen rich channel is on the left and the helium rich on the right. Important physical processes which may account for changing photospheric composition and hence white dwarf class are displayed in boxes. Characteristic temperatures along each channel are indicated. The circles to the right of the non-DA channel highlight important points in the changing DA:non-DA ratio as the stars cool.

There are two main theories as to why the bifurcation of the cooling sequence exists, which are summarised by Shipman (1989). The primordial theory assumes that the two cooling channels are separate and result from events in the pre-white dwarf stage of evolution. Iben (1984) has shown that the timing of a superwind during the thermal pulse cycle of a post-AGB star can dictate whether the star will evolve into a DA or a non-DA. If the superwind develops after a helium shell flash (for a small fraction of time the star is severely out of thermal equilibrium because of a 'flash'-like instability of the helium burning shell), all of the surface hydrogen will be lost allowing subsequent non-DA evolution. However, if it develops before the helium shell flash, the star will retain enough surface hydrogen to evolve into a DA with a thick hydrogen layer $\sim 10^{-4}M_{\odot}$. There is some evidence to support this theory in the existence of both H-rich and He-rich PNN. However, Iben & Macdonald (1985) predict that DAs should be detected as hot as 150,000K and take about 10^5yrs to cool down to 80,000K which is comprable to the time He-rich objects are hotter than 80,000K. Therefore the lack of very hot DAs cannot be explained in terms of shorter cooling times. The existence of the DB gap is explained within the primordial theory by the DO stars accreting material from the ISM to transform them into DAs by the time they cool to 45,000K. MacDonald & Vennes (1991) show that this is feasible in principle, but the existence of DOs at $\approx 50,000$K places limits on the possible accretion rate four orders of magnitude lower than required to make the transformation.

The alternative idea, known as the 'mixing theory', partly arose from soft X-ray observations of hot DA stars, which indicated the presence of trace amounts of helium (or heavier elements) providing a source of opacity at those wavelengths. Vennes *et al.* (1988) argued that radiative levitation cannot support enough helium in the atmosphere to account for the opacity. Instead, they suggested that hot DAs are stratified objects with a very thin layer of hydrogen ($\approx 10^{-14}M_{\odot}$) which is sufficiently thick that optical radiation escapes only from the pure hydrogen outer regions yet is sufficiently thin that the X-rays escape from deeper helium polluted regions. This lead Fontaine & Wesemael (1987) to propose that both DA and non-DA stars form by a single route from PNN, possibly via the very hot DO type PG1159 stars which only have a little hydrogen. Various physical processes may then be invoked to explain how DOs can evolve into DAs and at least some DAs into DBs, details of which are given below. Although this theory in isolation cannot account for the observed bifurcation in PNN, it does provide a natural way of explaining the observed DA and DB gaps in the cooling sequence.

1.6 The Case for Thin Hydrogen Layers

In the very hot PG1159 stage of the cooling sequence, minute quantities of residual hydrogen may be mixed in the outer helium envelope. Due to the very high gravitational field, as the star cools, in the absence of any competing effects such as a wind or accretion, the small amount of hydrogen diffuses upward to give a thin ($< 10^{-8}M_{\odot}$) hydrogen layer and hence the surface of a DA star. This is viable even for initial abundances as small as H/He = 10^{-10} and naturally leads to a stratified structure with a thin hydrogen layer overlying a helium envelope. The time taken for the transformation from DO to DA will depend on the surface gravity and the amount of residual hydrogen in the atmosphere. By the time the surface temperature has dropped to $\approx 45,000$K, all DOs have changed into DAs giving the break in the non-DA sequence. An attractive feature of this hypothesis is that the diffusion time scale for the hydrogen to accumulate on the surface is nearly equal to the cooling time scale of the DO stars down to 45,000K. This also explains why there are no DAs (with the exception of RE1738+66) with $T_{eff} \gtrsim 70,000$K as they are still DO stars awaiting the upward migration of hydrogen. If the hydrogen layer is too thick, the transition to DA would occur too early. The DAO stars would then be the intermediate stage where the helium is settling out of the photosphere.

The emergence of DBs below the break in the non-DA sequence is then accounted for within the 'thin hydrogen layer' DA theory by the onset of convection at $\approx 30,000$K as indicated in figure 1.2, which mixes the surface hydrogen back into the helium envelope. This can only occur with a thin hydrogen layer of $< 10^{-15}M_{\odot}$ (Liebert *et al.* 1986). Even a mass of hydrogen this small will still give the optical spectra of a DA due to the high opacity of hydrogen at optical wavelengths (see section 2.1). However, this is in conflict with the theoretical evolutionary calculations which predict that DA white dwarfs should be formed with massive hydrogen layers ($\geq 10^{-4}M_{\odot}$) in order to account for the observed luminosity function (e.g. Iben & Tutukov 1984; Iben & Macdonald 1985; Koester & Schönberner 1986). To establish layers thinner than $10^{-4}M_{\odot}$ Bruhweiler & Kondo (1986) proposed the presence of weak stellar winds in the hottest DAs. Alternatively, diffusion-induced nuclear burning in the helium envelope, occurring when the high energy equilibrium diffusion tail of carbon, extending upward from the core, encounters the hydrogen diffusion tail causing destruction of protons via $^{12}C(p,\gamma)^{13}N$ is a possible explanation (Michaud & Fontaine 1984). However, this has largely been ruled out by the study of the reaction rates (Iben & Macdonald 1985). If the white dwarf has a hydrogen layer thicker than $10^{-15}M_{\odot}$ it will remain a DA. It is assumed that the amount of hydrogen left after the ejection of a planetary nebula is variable resulting in some 'thick' layers and some 'thin' layers. This would explain the decrease in the DA:non-DA ratio from $\approx 7:1$ above the DB gap to $\approx 4:1$ below it. It is then possible that the observed hydrogen rich PNN account for the 'thick' layered DAs which remain DAs throughout the cooling sequence. Consequently, one would expect to detect hydrogen layer masses from $10^{-16} - 10^{-4}M_{\odot}$ for DAs with $T_{eff} > 28,000$K, but for DAs with $T_{eff} < 28,000$K only hydrogen layer masses greater than $10^{-15}M_{\odot}$.

As the observed DA:non-DA ratio decreases from $\approx 4:1$ at $T_{eff} > 20,000$K to roughly 1:1 at $T_{eff} \approx 6,000$K, not all the DAs which will become DBs undergo the transformation at 28,000K. The predictions of most models indicate that in DAs, a second convection zone develops at about 15,000K increasing in depth dramatically below 10,000K. If this reaches into the helium layer (as it will for hydrogen layer masses $\approx 10^{-10}M_{\odot}$; Koester 1976; Vauclair & Reisse 1977) then the DA will become a DB. The presence of this convection zone together with the one at $\approx 30,000$K is strong evidence that many DAs may have thin hydrogen layers.

Additional evidence that not all DAs have hydrogen layers $\sim 10^{-4}M_{\odot}$ comes from studies of the ZZ Ceti pulsating DAs (e.g. Winget *et al.* 1982; Winget 1993). The variability of these stars is due to various stellar oscillations which depend on the star's mass, temperature, radius and atmospheric structure. From modelling the power spectra of these stars (DAVs), it is found that the hydrogen layer mass cannot exceed $10^{-8}M_{\odot}$. Thus, white dwarf oscillations also appear inconsistent with thick hydrogen layers in all DAs. However, the most recent examination of pulsation theory by Fontaine *et al.* (1994) contradicts these results. Using new non-adiabatic models, they find that DA stars may have thick hydrogen layers, in keeping with standard evolutionary theory, yet still pulsate as observed in the ZZ Ceti instability strip. As the two theories clearly disagree they suggest an urgent and thorough re-examination of pulsation theory is called for.

One problem for the transformation of DA to DB by convective mixing is the appearance of the DBA class of white dwarfs below $\approx 30,000$K. The additional hydrogen features in the predominantly helium optical spectra of these objects implies hydrogen abundances of H/He $\approx 10^{-4}$ (Shipman, Liebert & Green 1987). If the hydrogen was simply the result of the convective mixing process one would expect most of the DBs to be DBAs when observed at high resolution. However, Shipman *et al.* (1991) failed to detect any hydrogen in the spectra of a statistically significant sample of DBs. Also, the estimated mass inside the helium convection zone of a DB is $\approx 10^{-6}M_{\odot}$. As the typical measured hydrogen abundance of a DBA is H/He $\approx 10^{-4}$ this implies a hydrogen layer mass of $\approx 10^{-10}M_{\odot}$ which is above the limit ($\approx 10^{-15}M_{\odot}$) where the helium convection zone occurs and a DA becomes a DB at $T_{eff} \approx 30,000$K. A possible explanation for the existance of DBAs is that the hydrogen present results from accretion of the ISM. A reasonable accretion rate of $10^{-15}M_{\odot}\,yr^{-1}$ (Aannestad & Sion 1985) can, in a cloud crossing time of 10^5yr (well within the cooling timescale) produce the required $10^{-10}M_{\odot}$ of hydrogen.

In summary, the changing DA:non-DA population ratios with temperature on the white dwarf cooling sequence may be accounted for within the mixing theory by the majority of DA stars having thin hydrogen layers. Apart from a minority of DAs which evolve directly from H-rich PNN, all remaining white dwarfs are initially of type DO. As they cool the residual hydrogen in the atmosphere diffuses to the surface. The more hydrogen the white dwarf has, the faster (and hence at higher temperature) it will become a DA. By the time the temperature has dropped to 45,000K, all DOs have become DAs giving rise to the DB gap. At $\approx 28,000$K, the first convection zone develops and DAs with hydrogen layer masses less than $10^{-15}M_{\odot}$ are turned into DBs. At 15,000K, the second convection zone develops, turning all those remaining DAs with layer masses less than $10^{-10}M_{\odot}$ into DBs. Those DAs with layer masses greater than $10^{-10}M_{\odot}$ once formed, remain as type DA throughout the cooling sequence.

1.7 Previous EUV Observations of Hot DA White Dwarfs

Over two decades ago Cruddace *et al.* (1974) showed that with a low density, non-uniform ISM, it would be possible to observe in the EUV/X-ray over considerable distances. This lead to the first soft X-ray observations of white dwarfs. In explaining the observed emission from Sirius B, Shipman (1976) first pointed out that at the temperatures of hot DAs, the outer layers would be highly ionized and so transparent to radiation from deeper in the atmosphere and could therefore emit copious amounts of thermal EUV/soft X-ray radiation. Due to the energy dependence of the opacity of hydrogen, observations in the EUV and soft X-ray hold great potential for examining the changes in composition with depth in the atmosphere. Hence they can provide direct evidence for the presence of thin hydrogen layers. Even though a DA appears optically as pure hydrogen, in the EUV and X-ray a thin layer DA would show the presence of helium as a deficit in the expected EUV/X-ray flux.

Based on the hypothesis that there is some interchange between the two branches of the cooling sequence, with DO stars turning into DA stars through gravitational settling of helium, it should be possible to observe some residual helium in the hottest DAs. The earliest rocket born EUV observations of the hot DA HZ43 showed the atmosphere to be consistent with pure hydrogen (Margon *et al.* 1976; Lampton *et al.* 1976; Holberg *et al.* 1980). However, with the advent of the X-ray observatory *Einstein*, the presence of an opacity source was discovered in most hot DAs and was widely interpreted as being due to helium, homogeneously mixed throughout the atmosphere with an abundance of He/H $\geq 10^{-6}$ (Kahn *et al.* 1984). Furthermore, Petre, Shipman & Canizares (1986) found evidence for increasing opacity with increasing effective temperature as would be expected if the DO stars were transforming into DAs with thin hydrogen layers. Subsequent observations with the *EXOSAT* sattelite (Jordan *et al.* 1987; Paerels & Heise 1989) found slightly weaker but significant trends of increasing opacity with increasing T_{eff}.

Kahn *et al.* (1984) proposed two possible mechanisms as explanations for the finite observed abundances: accretion from the ISM or selective radiative levitation of helium. The discovery of higher abundances in hotter stars lead Petre, Shipman & Canizares (1986) to favour radiative levitation as this was the only mechanism which could give rise to such a correlation. However, Jordan *et al.* (1987) noted that, in the absence of competing effects, a stratified structure would be physically more realistic due to the high gravitational field. In light of the work by Vennes *et al.* (1988) who demonstrated that the amount of helium which could be supported in the atmosphere by radiative forces is too small by at least two orders of magnitude to account for the EXOSAT observations, Koester (1989) utilised model atmospheres which assumed a stratified structure to analyse an EXOSAT sample of DAs. He discovered the count rates could be modelled equally well by such a structure but found no strong correlation between the hydrogen layer mass and temperature other than a general tendancy for thinner layers in the hotter stars. Thus, the data were not of sufficient quality to be able to distinguish whether the stars have thin layers or whether they have standard thick layers with the opacity source spread throughout.

Besides the inability to distinguish between physical models (homogeneous or stratified), an added problem in the work outlined above is that they all make the implicit assumption that helium is the only significant opacity source in the EUV/X-ray region. This is not necessarily true. Kahn *et al.* (1984) mention that helium remains the dominant opacity source below 227Å only if abundances of heavier elements are maintained below 10^{-3} of their solar values. Vennes *et al.* (1989) showed that the *EXOSAT* grating spectrum of the hot DA Feige 24 (which has a similar temperature and surface gravity to HZ43) cannot be explained by either homogeneous or stratified H + He models. However, they showed that a photospheric model with trace elements heavier than helium can fit the observations. Furthermore, Wesemael, Henry & Shipman (1984) had reported absorption lines due to CIV, NIV and SiIV in the IUE spectrum. Many other DAs have now been spectroscopically observed in the UV to reveal a host of heavy elements. For example, Vennes, Thejll & Shipman (1991) also found C, N, and Si features in several hot DAs. An EUV spectrum of the hot DA G191−B2B obtained from a sounding rocket flight revealed features thought to be due to OIII and FeV (Wilkinson, Green & Cash 1992). UV observations of newly identified white dwarfs in the ROSAT survey resulted in the discovery of two of the hottest and most contaminated DA atmospheres yet known, RE0623-37 and RE2214-49. The spectra of these stars not only displayed many features due to C, N, O, Si, Al but also Fe and Ni (Holberg *et al.* 1993; Holberg *et al.* 1994). Vennes *et al.* (1992a) also detected Fe species in the IUE spectra of the hot DAs Feige24 and G191−B2B.

Interestingly, Wilkinson, Green & Cash (1992) found no sign of the HeII edge at 228Å in their spectrum of G191−B2B. More recently, Barstow, Holberg & Koester (1994) have studied the *Extreme Ultraviolet Explorer* (EUVE) spectra of four hot DAs (including G191−B2B and Feige 24) and also found no sign of photospheric He, suggesting that helium in fact plays a minimal, if any role in the atmospheres of the DA stars which is contrary to the view of DOs transforming into DAs.

1.7.1 Opacity from Heavy Elements

A thorough understanding of the compositional evolution of white dwarfs requires measurements of the abundances of trace elements. Whether a population of heavy elements can be sustained in a predominantly hydrogen or helium atmosphere depends critically on the balance between gravitational settling and competing processes that can hypothetically support them. Possible mechanisms include diffusion, convective dilution, accretion, stellar winds and more obviously radiative levitation due to the intense radiation field present in these hot stars. Prompted by the identification of species such as C, N, O and Si in some of the hotter stars, detailed calculations by various groups showed early on that radiative levitation could effectively compete against the gravitational field and support significant quantites of these elements in the photosphere for a prolonged period (Morvan, Vauclair & Vauclair 1976; Vauclair 1989; Chayer, Fontaine & Wesemael 1989). From the subsequent discovery of a preponderance of species of heavier elements such as Fe and Ni, further calculations have been performed including many of their transitions (of which there are thousands) to show that in the hot DA temperature range, all the identified species may be supported above their solar values at specific values of T_{eff} with surface gravity dictating the observed abundances (see e.g. Chayer, Fontaine & Wesemael 1995).

However, as already mentioned, similar calculations for the levitation of helium by Vennes *et al.* (1988) showed that the process was not efficent enough to sustain the abundances needed to absorb enough of the EUV/X-ray flux in order to explain the observed EXOSAT and Einstein count rates. Thus, once a DO has transformed into a DA, the residual helium may very quickly sink out of the part of the photosphere where the EUV/X-ray flux originates. This would provide a possible explaination as to why helium was not observed in the EUV spectra examined by Barstow, Holberg & Koester (1994).

The growing body of evidence for the presence of elements heavier than helium in hot DA atmospheres lessens the need to invoke thin hydrogen layers as an explanation of many observations. A number of authors have shown that radiative levitation of a complex of heavy elements with low individual abundances may be more appropiate in some and, perhaps, most cases than a thin layer of hydrogen on top of a helium atmosphere (Vennes, Thejll & Shipman 1991; Vennes & Fontaine 1992). If the investigation into pulsation theory reveals that thick hydrogen layers are possible this would seriously call into question the thin hydrogen layer hypothesis. Moreover, a recent analysis of a sample of DAO white dwarfs (Bergeron *et al.* 1994) which were believed to represent the best case for stratification due to the spectral visibility of helium (see e.g. MacDonald & Vennes 1991), indicates that the atmospheres are homogeneously mixed rather than stratified with a thin hydrogen layer. This implies that they are not an evolutionary link between the DO and DA stars with the hydrogen diffusing upward in the atmosphere. Bergeron *et al.* (1994) suggest that instead the DAO stars are possibly descendants of subdwarfs rather than those which have evolved through the AGB phase.

1.8 ROSAT Observations

The ROSAT all-sky survey provides a unique opportunity to examine some of the major questions concerning the structure, composition and evolution of DA white dwarfs. If thin hydrogen layers provide an adequate representation of the majority of DA atmospheres this will add support to theory that DOs transform into DAs above $\approx 45,000$K and some DAs turn into DBs below $\approx 28,000$K. However, all previous works have been unable to distinguish between a stratified atmosphere and an atmosphere where the helium is homogeneously distributed. Barstow *et al.* (1993) examined a sample of 30 well known DAs from the ROSAT survey and also could not distinguish physical structures. The work presented here utilises the full sample of DAs observed in the entire sky and hence the only selection criteria are that they are EUV bright enabling a more comprehensive analysis.

In order to investigate the role of helium in hot DA atmospheres, only H + He model atmospheres are used. If the majority of stars may be represented in this way it is possible that helium may be a dominant opacity source. However, in light of the observational and theoretical evidence described above, and the fact that ROSAT data are photometric rather than spectroscopic, a H + He representation of the observed count rates may be misleading with opacity from elements heavier than helium accounting for the reduced fluxes. The presence of heavier elements can be inferred from the data if some DAs cannot be modelled satisfactorily by hydrogen and helium alone.

Finally, independent of the actual absorbing material, be it helium or heavier elements, with such a large sample of objects we have the best opportunity to date of examining how the opacity varies with temperature and gravity. This may provide valuable observational evidence for theoretical radiative levitation calculations. Any such correlation with the stellar parameters T_{eff} and log g may be found by simple examination of the relative emergent fluxes for different stars.

Chapter 2

Observations of Hot White Dwarfs from the ROSAT All-Sky Survey

2.1 The EUV/X-ray emission from Hot White Dwarfs

The photospheric composition of hot white dwarfs is predominantly hydrogen and/or helium. The observed spectral energy distribution is therefore primarily dependent on the absorption characteristics of these elements and their relative abundances, together with the atmospheric structure and temperature gradient defining a specific spectral shape. Figure 2.1 shows the variation in the absorbtion coefficient for the species HI, HeI and HeII at a temperature of 25,000 K as a function of energy from the optical to soft X-ray. It is immediately evident that for helium white dwarfs (DOs, DBs) the EUV cross-section per He atom k_{EUV}/He, for HeI and HeII, at 25,000 K, is many orders of magnitude greater than the optical cross-section k_{OPT}/He. This means that whatever the degree of ionisation, helium white dwarfs show very little emission in the EUV compared to the optical. However, as the number of atoms in excited states (quantum energy level $n > 1$) increases with increasing temperature according to the Saha-Boltzmann equation, this difference between k_{OPT}/He and k_{EUV}/He decreases with increasing temperature. It is possible to calculate minimum detectable temperature limits for the ROSAT bandpasses as a function of interstellar column by convolving model white dwarf spectra through the instrument responses. Prior to the ROSAT launch, Barstow (1989) found that DO white dwarfs observed through a column density of 10^{19} cm^{-2} would require a temperature in excess of 60,000K in order to be detected in all the survey bandpasses. He noted that the space density of DOs with temperatures substantially in excess of this are very low and so predicted that very few would be observed (in fact 10 were detected in the survey).

The situation for the DA stars is very different. From figure 2.1 it can be seen that at temperatures as low as 25,000K, k_{EUV}/H is $\approx$ 30 times less than k_{OPT}/H. Thus, the EUV radiation originates from much deeper in the photosphere than optical radiation. At higher effective temperature, increasing ionisation reduces the bound-free opacity generally, but the rising population of the n = 2 and n = 3 states increases optical opacity compared to the EUV, suggesting the limiting temperature for DA detection is substantially lower than for DOs. Barstow (1989) found a limiting temperature of 20,000K for detection in all bands of a pure hydrogen DA with an intervening column density of $10^{19}\,\mathrm{cm}^{-2}$. From known DA space densities (Fleming, Liebert & Green 1986) one would expect to detect of the order of 1000 DAs above 20,000K in all survey bandpasses (Finley 1988; Barstow & Pounds 1988).

However, a DA will only be EUV bright if the atmosphere is pure hydrogen. Due to the large difference between k_{OPT}/H and k_{OPT}/He a white dwarf could appear as a DA optically but in fact have significant amounts of helium deeper in its atmosphere. If helium is present, then it is evident from the difference in the EUV cross-section between HI and HeI or HeII that the EUV opacity will increase significantly for even small abundances. This is demonstrated in figure 2.2 which shows four model DA spectra each with an effective temperature of 30,000K and logg = 8, but with hydrogen layers of varying thickness. Also plotted are the mean energies of the PSPC, S1a and S2a survey bands (see next section). The continuous line shows a pure hydrogen spectrum, with line features due to the Balmer series terminating at the Balmer discontinuity (3646 Å), and the Lyman series terminating at the Lyman limit (912 Å). The three other spectra are for DAs with hydrogen layers thin enough for the EUV photons to originate from deeper layers where there is trace helium present from the H/He diffusion boundary. The line features visible are due to HeI. If homogeneously mixed, an abundance as low as He/H > 10^{-5} at $T_{eff} = 30,000$K begins to affect the EUV fluxes. Hence, figure 2.2 shows that the survey bands cover a spectral region where trace helium has a significant effect on the spectral shape and therefore clearly demonstrates how the ROSAT detectors are ideally suited to studying opacity in hot DA atmospheres.

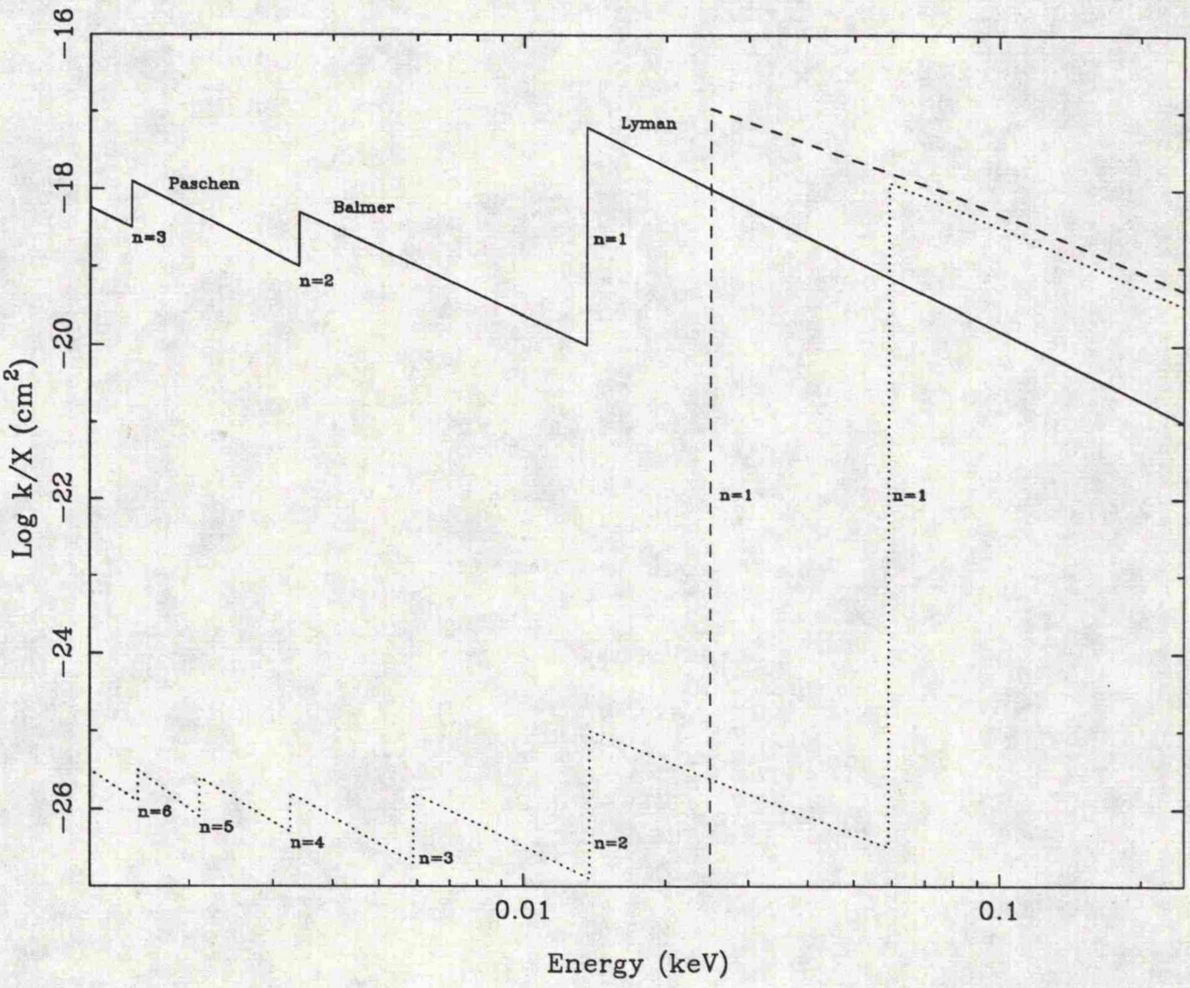

Figure 2.1: Absorption coefficients per absorber k/X, for HI, HeI and HeII as a function of energy from the optical to the EUV. Also shown are the principal quantum numbers for each ionisation edge and the names of the H edges. HI - solid line, HeI - dashed line, HeII - dotted line. (Data is from Böhm-Vitense (1989) and Cruddace *et al.* (1974))

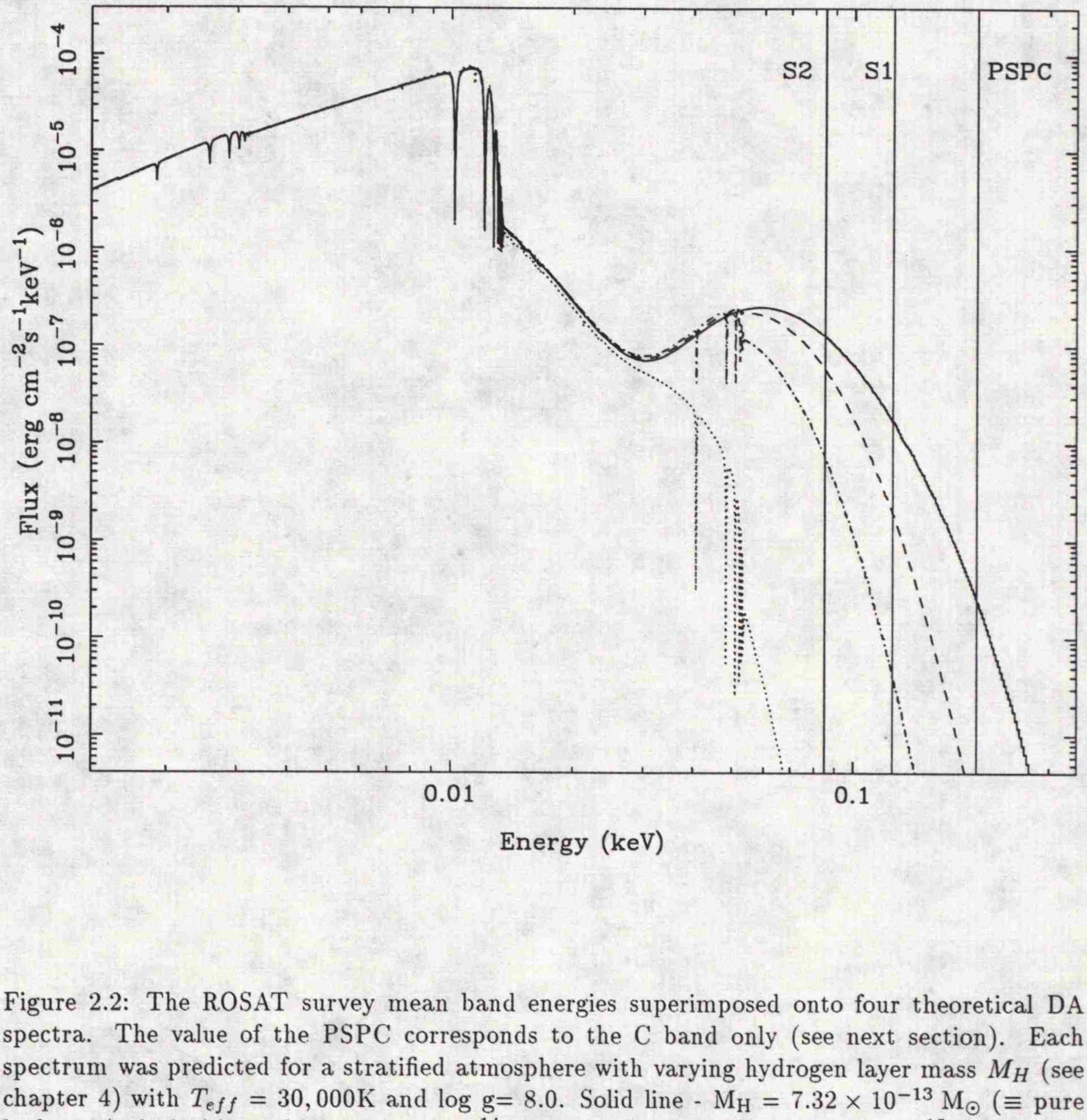

Figure 2.2: The ROSAT survey mean band energies superimposed onto four theoretical DA spectra. The value of the PSPC corresponds to the C band only (see next section). Each spectrum was predicted for a stratified atmosphere with varying hydrogen layer mass M_H (see chapter 4) with T_{eff} = 30,000K and log g= 8.0. Solid line - $M_H = 7.32 \times 10^{-13}$ $M_\odot$ ($\equiv$ pure hydrogen), dashed line - $M_H = 3.21 \times 10^{-14}$ $M_\odot$, dash-dot line - $M_H = 9.16 \times 10^{-15}$ $M_\odot$, dotted line - $M_H = 2.89 \times 10^{-15}$ $M_\odot$.

2.2 The ROSAT Observatory

The ROSAT satellite was launched on a Delta II rocket from Cape Canaveral on June 1^{st} 1990, into a circular orbit at an altitude of 580 km, giving an orbital period of 96 minutes. The orbital inclination of 53° provides 5 or 6 spacecraft contacts (each of $\approx$ 10 minutes) per day with the groundstation at Weilheim, Germany. The observatory consists of two co-aligned imaging instruments, the German X-ray telescope (XRT: Aschenbach 1988) and the British EUV telescope, the Wide Field Camera (WFC: Sims *et al.* 1990). A schematic view of the ROSAT spacecraft and its major components, together with a cut away diagram of the WFC are given in figure 2.3.

The spacecraft is a three-axis stabilised satellite using gyroscopes and high torque momentum wheels (which allow fast slews of up to 180° in $\sim$ 15 minutes) with a 3σ pointing accuracy of 1 arcminute. Two CCD star sensors on the XRT are used for position sensing of guide stars and spacecraft attitude determination (the WFC carries its own star sensor for independent attitude determination but this is not used for spacecraft control). These allow attitude determination to be reconstructed at the groundstation to an accuracy of 6 arcseconds.

The objectives of the mission (Trümper 1984) were to carry out the first survey of the entire sky in both the EUV and X-ray during the first 6 months of operation and then to provide a facility for more detailed observations of pre-selected targets with longer exposure times, which is now entering its 6^{th} phase.

2.2.1 The XRT

The X-ray mirror assembly (XMA) of the XRT is a grazing incidence four-fold nested Wolter type I configuration (Wolter 1952). All of the 8 mirror shells are made out of Zerodur, a glass ceramic with an almost negligable thermal expansion coefficient, and are coated with a thin gold layer in order to increase X-ray reflectivity. Typical grazing angles are between one and two degrees, depending on the mirror subshell considered. The total geometric collecting area of the XMA is $1141 \mathrm{cm}^2$ on axis and is a strong function of energy. The focal length is 240 cm with an

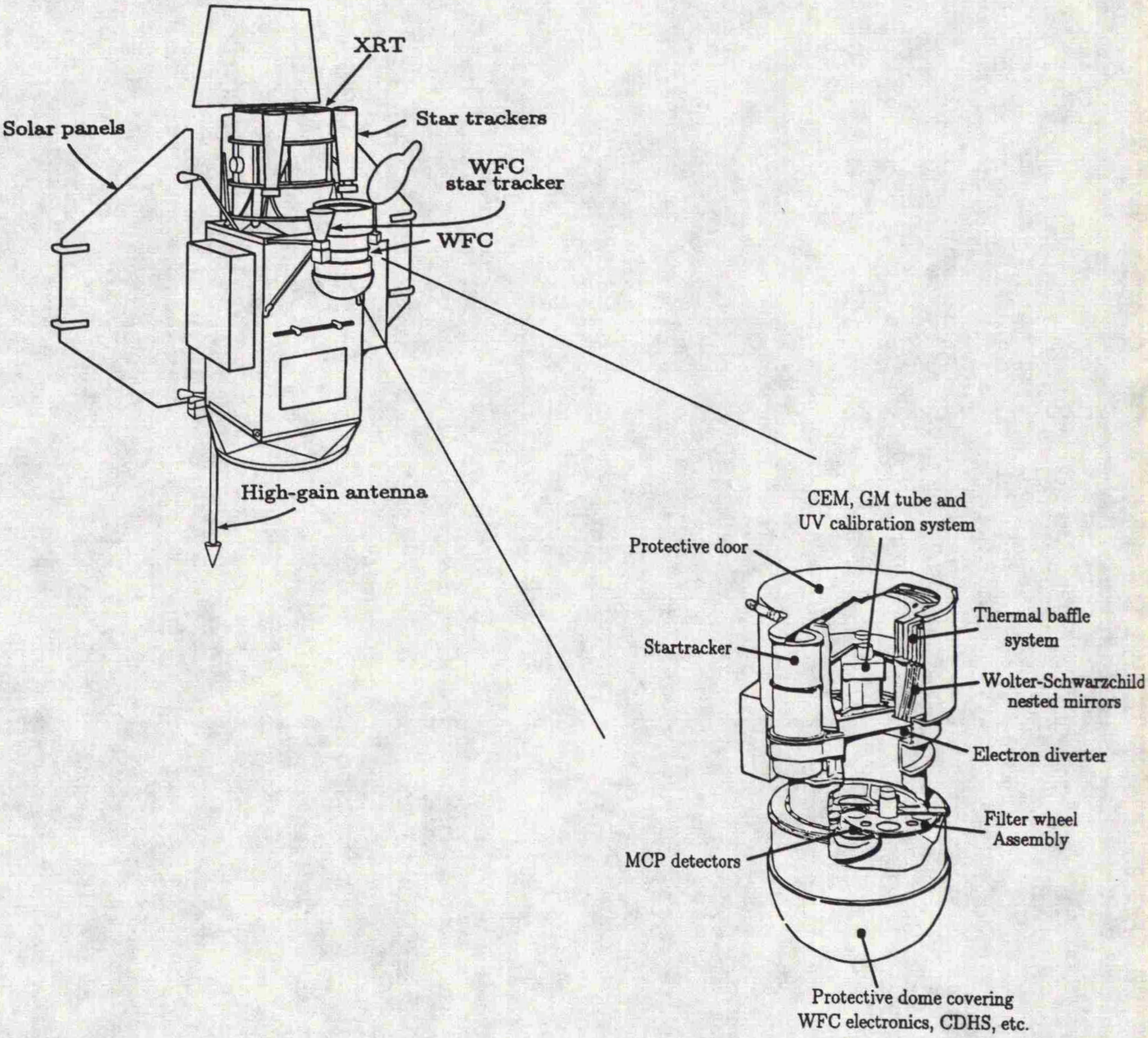

Figure 2.3: Schematic diagram showing the ROSAT satellite and a cutaway of the WFC with the primary components indicated.

aperture of 84cm diameter yielding a total field of view of 2°.

At the focus of the XRT are three interchangeable detectors, two Position Sensitive Proportional Counters (PSPCs) and the High Resolution Imager (HRI). As only the PSPC 'C' detector was used during the all-sky survey (Pfeffermann *et al.* 1987), the data from which are utilized in this thesis, the HRI shall not be considered further. The PSPC is a multi-wire gas filled proportional counter with a cathode strip readout scheme for position determination. It has an 8cm diameter sensitive area which subtends the full 2° field of view of the XMA. The X-ray absorption of the counter gas (a mixture of Argon, Xenon and Methane) is close to 100% up to ≈ 2 kev which is the mirror reflectivity high energy cut off. The quantum efficiency of the detector is therefore determined by the transmission of the entrance window which maintains the gas pressure. This polypropylene window has a thin carbon/lexan coating in order to decrease UV transmission. As a consequence, the window is opaque to energies just above the carbon edge at 0.28 keV, but has a transmission of $\sim 50\%$ just below this. Due to the steep fall off in flux toward higher energy in the X-ray region of the spectrum, white dwarfs are only detected below the carbon edge (known as the C band; $0.1 - 0.28$keV). A detection above this energy suggests radiation from another source is present. Although the PSPC posseses some spectral capability, the energy resolution was not utilized in this work. Instead, the total integrated flux detected in the C band was used as a photometric data point.

2.2.2 The WFC

The WFC optics consist of a nested set of 3 Wolter-Schwarzchild Type I mirrors, fabricated from aluminium and coated with gold for maximum reflectance. The mirrors provide a geometric collecting area of 456 cm^2 with a common focal length of 525 mm. The grazing incidence angles chosen (typically $\approx 7.5°$) allow the collecting area to be optimised whilst retaining a wide (5° diameter) circular field of view with a high energy reflectivity cut-off at 210 eV.

The focal plane detector (of which there are two) is a micro-channel plate (MCP: Barstow & Sansom 1990) curved to match the optimum focal surface. Each MCP consists of an array of $\sim 10^7$ close packed channels, drawn and etched from a lead glass matrix. A CsI photocathode is deposited directly onto the front face of the MCP to enhance the EUV quantum efficiency.

Table 2.1: Summary of XRT+PSPC and WFC Filter Characteristics

Instrument	Detector or Filter Name	Composition	Mode	Field Of View (°)	Mean Energy (eV)	Bandpass (eV)
XRT	PSPC	—	S + P	2.0	206	158-281
	S1a	C + B + Lx	S + P	5.0	124	90-185
	S1b	C + Lx	S + P	5.0	124	90-210
WFC	S2a	Be + Lx	S + P	5.0	90	62-111
	S2b	Be + Lx	S + P	5.0	90	62-111
	P1	Al + Lx	P	2.5	69	56-83
	P2	Sn + Al	P	2.5	20	17-24

Notes:
Composition: C=Carbon, Al=Aluminium, B=Boron, Be=Beryllium, Sn=Tin, Lx=Lexan
Mode: S=Survey, P=Pointed
Bandpass measured at 10% of peak efficiency

Thus, each channel of the MCP behaves as a photomultiplier tube under high voltage. The detector has a 4.5 cm diameter sensitive area, utilizing the full 5° diameter field of view. On axis the spatial resolution is 1 arcminute (FWHM), degrading to 3 arcminutes at the edge.

Unlike the PSPC, the WFC detector posseses no intrinsic energy resolution. Therefore a filter wheel was provided in conjunction with the MCP in order to constrain the passbands. During the survey, two filters (S1a and S2a) were used on alternate days with another two (S1b and S2b) providing redundancy. After completion of the survey, two more filters (P1 and P2) were made available for use in the pointed phase of the mission. Details of the filter characteristics (together with a description of the XRT+PSPC) are given in table 2.1. Although several P1 and P2 observations are available, detection at these energies is difficult due to high absorption from the ISM. Hence, only survey detections were utilised in the work presented here. Both the S1a and S2a filters were made from a lexan substrate and had a coating of carbon/boron and beryllium respectively. The effective areas of the filter + detector/optics combinations are shown in figure 2.4 together with those of the PSPC + XMA. The shape of the filter responses are due to various absorption edges in the filters (or the entrance window for the PSPC) and the increasing absorption cross-section with energy, inherent in the material. The hard roll off in the S1a efficiency is due to the WFC optics. The cut-off energies are then determined by the edges of boron and then carbon. The S2a response is cut off by the Beryllium edge. As in the case of the PSPC, the presence of lexan effectively renders the filters opaque in the UV.

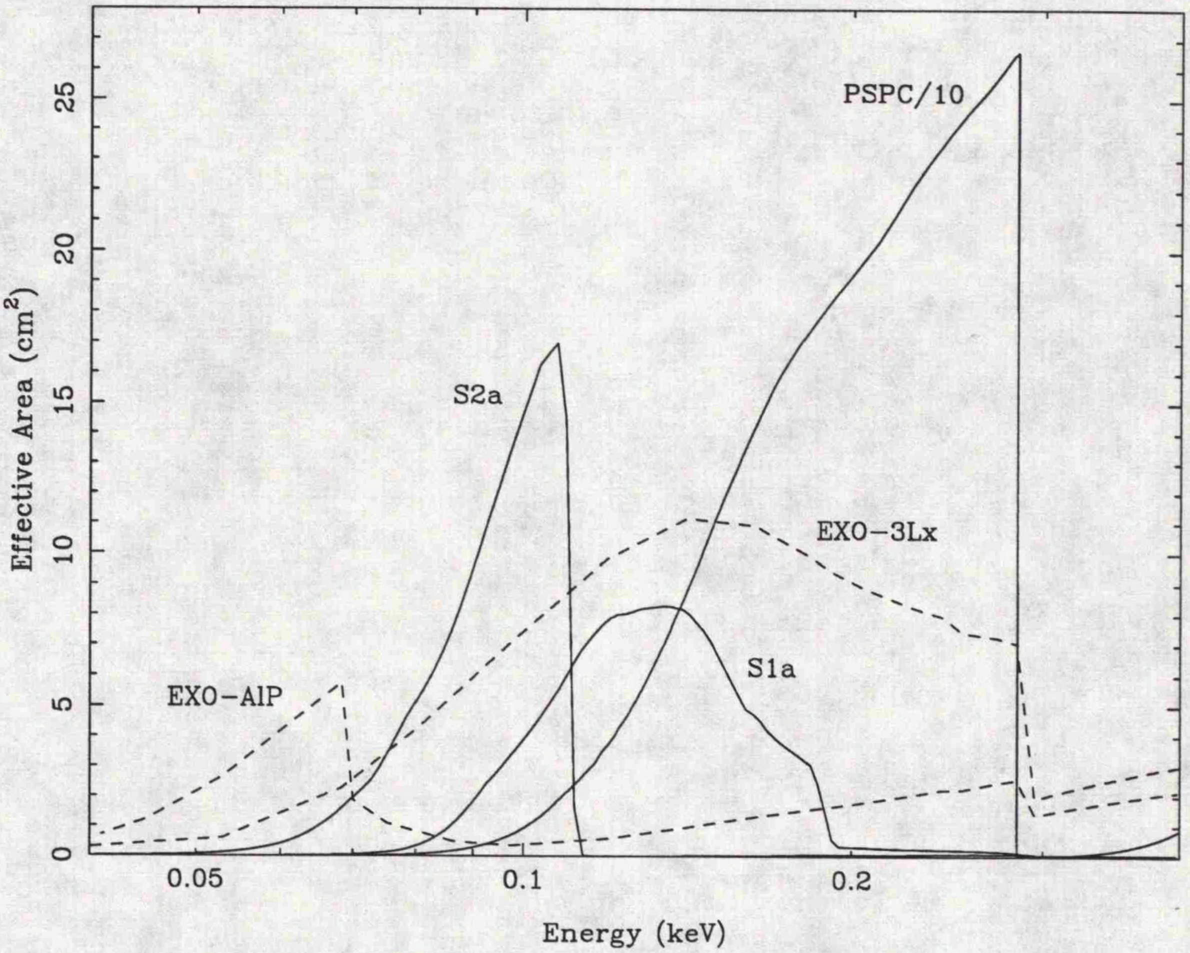

Figure 2.4: The on-axis effective area as a function of photon energy for the instruments used in the ROSAT all-sky survey. Solid lines show the XRT PSPC'C' and the WFC S1a and S2a filters (+MCP detector) as indicated. For comparison, the dashed lines show the response of the EXOSAT thin lexan (3Lx) and aluminium/parylene (AlP) filters.

Shown for comparison in figure 2.4 are the responses of the prime EXOSAT thin lexan (3Lx) and aluminium/parylene (AlP) filters. It can be seen that the ROSAT instruments yield a better energy resolution than was available with EXOSAT, thus providing more information with which to constrain any model.

2.3 The All-Sky Survey

The all-sky survey was performed over a period of six months from 31st July 1990 to 25th January 1991. Full sky coverage was obtained by rotating the spacecraft on an axis, once per orbit, such that the telescopes always pointed away from the Earth. This ensured the pointing axis traced out a series of great circles on the sky each passing through the ecliptic poles and crossing the ecliptic plane at a fixed angle. As the Earth moved around the Sun, the scan path advanced $\sim 1°$ per day to maintain the required orientation of the solar panels, thereby covering the entire sky in approximately six months. The exposure is therefore a function of ecliptic lattitude, the longest exposures being at the north and south ecliptic poles. However, in order to protect the detectors, both instruments were shut down while passing through regions of high particle background (ie. the South Atlantic Anomaly and the Northern and Southern Auroral Zones) resulting in a loss of $\approx 26\%$ of the exposure each day. Of the order of 10% of the sky was not covered due to various technical problems but these gaps were filled in at a later date, with reduced sensitivity in the WFC.

Once the full survey exposure had been achieved for a given region of sky, the PSPC images were divided into strips of ecliptic longitude and those of the WFC were divided into $2° \times 2°$ 'small maps'. In both cases, the data were searched for point sources and the measured positions were compared with catalogues of known objects. The 'C band' ($0.1 - 0.28$keV) count rates for each of the DAs in the PSPC survey were determined independently by Fleming *et al.* (1995). For the WFC, an automated source searching algorithm 'NIPS' (Page 1990) was used to extract the count rates of each object, published as the Bright Source Catalogue (BSC; Pounds *et al.* 1993) which contains 119 identified white dwarfs. Recently, a further catalogue with lower detection thresholds has been published known as the 2RE catalogue (Pye *et al.* 1995). This catalogue results from more refined source detection techniques as well as several other improvements such as better background screening and a more detailed understanding of the survey sensitivity.

The NIPS routine assumes a fixed source radius for extraction of the count rates and then corrects for the known point response function (psf) of the instrument. The assumption that the psf is the same for each source only holds if the source exposure is completely uniform across the telescope field of view. This is not true in general, since the detector was switched off while passing through the regions of high background. Hence, it is possible that an additional source of error in the count rates may be present which is not included in the catalogue data. To test the magnitude of any such hidden errors, the count rates for a subsample of stars (29 in all, see Barstow *et al.* 1993) were derived manually. This involved measuring the source count rate within an initial radius of 2.3 arcminutes after subtracting a backround rate taken from an annulus around the source scaled by area. The source circle was then gradually expanded until the count rate no longer increased. This ensured that more than 99% of the source counts were included and made no *a priori* assumptions about the psf. The same extraction radius was then used on the raw image in order to find the statistical count rate error. The errors derived manually are larger than those measured using NIPS as a greater background component was subtracted from a larger area on the image, but this method ensures that any hidden systematic errors arising from the assumed psf are included. The comparison of the count rates extracted manually with those found automatically (figure 2.5) shows they are in good agreement. Therefore, it may be assumed that any hidden systematic errors present in the count rates measured using the NIPS routine are insignificant.

As the 2RE catalogue was not available at the time of this work all the count rates used in this thesis were taken from the BSC apart from those for one object, RE0632-05 which showed an anomalous WFC band ratio with the S1 count rate more than three times that in the S2 band. Re-extraction showed this to be an error and the WFC count rates for this star were subsequently taken from the 2RE catalogue. Later comparison of the two catalogues showed the count rates for the remaining stars to be in agreement to within their statistical errors.

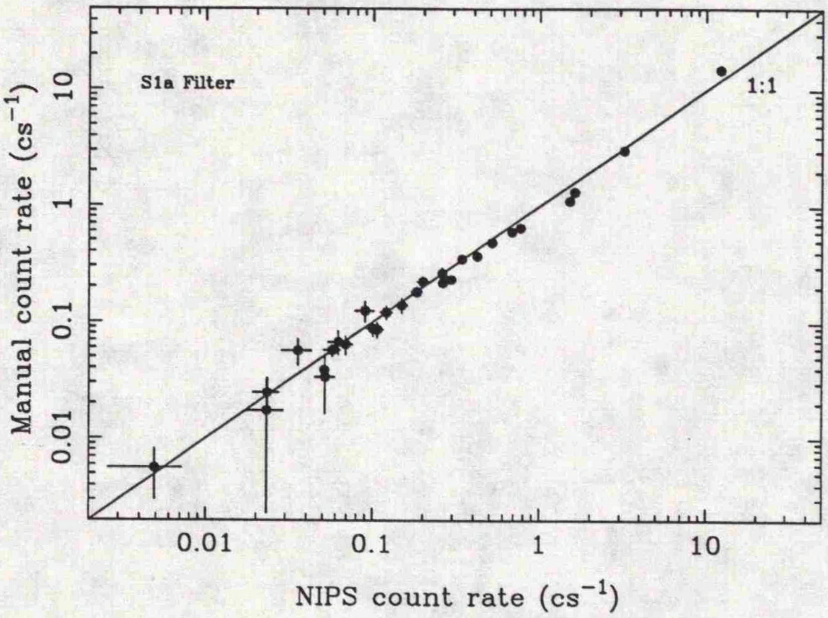

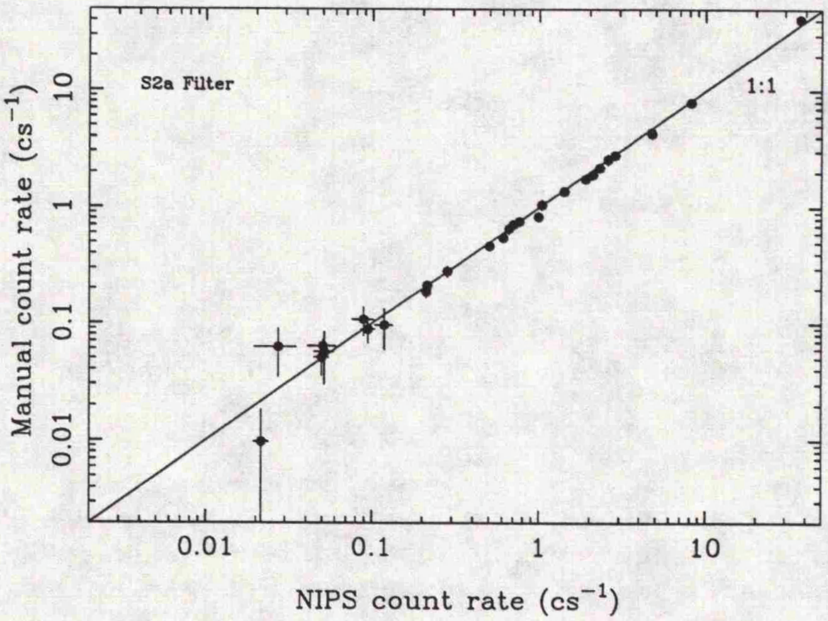

Figure 2.5: Comparison of count rates extracted using the automated NIPS routine and those derived manually for a subsample of 29 stars (see Barstow et al. 1993) for the WFC survey filters. The NIPS rates were taken from the Bright Source Catalogue. Both manual and NIPS rates are corrected to the launch epoch (see section 2.4.1).

2.3.1 Survey Sensitivity

During the survey, the WFC suffered a drift in quantum efficiency which reduced the sensitivity of the S1a and S2a bands to $\approx 30\%$ and $\approx 17\%$ of their initial values respectively by the end of the survey (Willingale 1995). The actual degradation of the instrument responses was monitored through several observations of the hot white dwarfs HZ43 and RE1629+781 and it was found to be a steady decline which could be approximated by a simple function giving correction factors for each filter with which the observed count rates may be multiplied of the form,

$$C_f = C_i(1 + 0.30\frac{MJD - 148}{180})\,(S1) \tag{2.1}$$

$$C_f = C_i(1 + 0.17\frac{MJD - 148}{180})\,(S2) \tag{2.2}$$

where C_i is the observed count rate, C_f is the count rate corrected to the launch epoch and MJD is the mean julian date of the observation.

On 25^{th} January 1991, the spacecraft suffered an attitude control systems failure during which time the 'open' telescopes pointed at the Earth and the Sun. This resulted in permanent damage to the PSPC 'C' detector and the S2a filter and detector of the WFC. However by this time, most of the survey had already been completed.

2.4 The ROSAT Sample

The survey PSPC and WFC S1a and S2a count rates (corrected to the launch epoch) for 86 DA and 3 DAO white dwarfs under investigation in this thesis, together with their statistical 1σ errors are presented in table 2.2. Several stars were not detected in one of the survey bands and therefore only upper limits to the count rates are available for these objects. These are given as 3σ above the local background and are indicated by a '$-$' in the error column.

Following completion of the survey, an extensive search of astronomical catalogues was carried out to identify the optical counterparts to the X-ray detections. The principal white dwarf catalogue of McCook & Sion (1987) allowed identification of 44 of the stars presented here as known DA white dwarfs. The remaining objects were identified as part of a program of follow up spectroscopic observations (Mason *et al.* 1995) to be 42 DA and 3 DAO stars. The new identifications are indicated in the table under the column headed 'Alternative Name'.

2.4.1 Known DAs Detected in the Survey

An estimate of the total number of known DAs with temperatures hotter than 20,000K suggests that ≈ 500 known DAs should have been detected in the survey (Fleming *et al.* 1993). Only 10% of these objects were detected which can not be explained by the effects of interstellar absorption. Barstow (1989) predicted that approximately twice as many DAs should have been detected by the PSPC compared to the WFC. However, the observed ratio of PSPC to WFC detections is around 1:1. If HI columns were greater than expected, the number of WFC detections would tend to *decrease* with respect to those in the PSPC. Conversely, lower than anticipated HI densities could increase the relative numbers of stars in the WFC data, but this is not consistent with the shortfall of detections from the known white dwarf catalogues. The predictions of the numbers of white dwarfs detected in the PSPC and WFC made simplistic assumptions regarding the expected atmospheric composition. Barstow (1989) assumed a canonical He:H ratio of 10^{-4} in a homogeneous mixture. The apparent shortfall of PSPC detections is strong circumstantial evidence for the presence of additional opacity in the form of heavy elements in DA atmospheres. With such a large sample of 'new ID' detections, together with the known white dwarfs, we are now in a position to investigate the effects of these additional opacity sources.

Table 2.2: Epoch corrected count rates from the ROSAT all-sky-survey

WFC	Alternative	Survey Count Rates ($c\,ks^{-1}$)						Mean Julian
Name	Name	PSPC*	1σ*	S1	1σ	S2	1σ	Date
RE0003 + 43	new ID	356.0	47.0	37.3	6.8	22.5	–	48179.7
RE0007 + 33	GD 2	2520.0	121.0	148.9	12.4	50.4	9.7	48178.8
RE0029 – 63	new ID	3790.0	190.0	625.7	35.9	1008.2	40.3	48195.9
RE0053 – 32	GD 659	3004.0	30.0	765.5	30.1	2079.1	44.6	48223.8
RE0108 – 35	GD 683	87.0	19.0	43.5	12.1	134.2	15.7	48226.8
RE0134 – 16	GD 984	1745.0	88.0	259.4	14.7	656.3	23.6	48178.8
RE0138 + 25	PG 0136 + 251	632.0	63.0	52.2	6.8	50.6	7.5	48182.6
RE0148 – 25	GD 1401	32.0	11.0	13.5	5.6	24.7	7.5	48178.8
RE0151 + 67	GD 421	158.0	20.0	23.3	4.1	49.4	5.0	48111.1
RE0230 – 47	LB 1628	50.0	16.0	24.8	4.5	135.1	9.7	48178.8
RE0235 + 03[a]	Feige 24	14.0	–	4.9	2.3	758.0	30.1	48183.3
RE0237 – 12	PHL 1400	329.0	39.0	55.6	10.2	121.6	12.9	48182.6
RE0322 – 53	LB 1663	230.0	76.0	68.9	6.8	210.4	11.8	48179.7
RE0348 – 00	GD 50	2086.0	71.0	291.7	16.2	500.7	19.1	48108.6
RE0350 + 17[b]	V471 TAU	1110.0	250.0	340.0	20.0	1040.0	29.0	48110.6
RE0457 – 28	new ID	106.0	27.0	120.5	10.2	2567.3	42.5	48115.5
RE0505 + 52	G191 B2B	40.0	22.0	62.2	8.3	2824.1	40.8	48125.0
RE0512 – 41	new ID	971.0	64.0	168.3	12.3	282.1	14.2	48118.6
RE0521 – 10	new ID	190.0	34.0	55.7	7.2	205.7	14.3	48122.1
RE0550 + 00	GD 257	725.0	13.0	100.4	8.4	94.4	9.2	48129.9
RE0550 – 24	new ID	373.0	41.0	23.0	4.2	15.4	6.2	48129.5
RE0552 + 15	GD 71	2800.0	113.0	679.0	21.9	2281.3	37.9	48129.5
RE0558 – 37	new ID	4.0	–	7.4	3.2	34.0	5.1	48133.9
RE0605 – 48	new ID	132.0	27.0	10.7	4.3	43.6	6.2	48141.8
RE0623 – 37	new ID	9.0	–	6.4	3.2	428.0	15.6	48146.2
RE0632 – 05[c]	new ID	1506.0	66.0	142.0	9.0	255.0	15.0	48141.8
RE0645 – 16	SIRIUS B	19730.0	290.0	3200.2	41.8	8187.4	68.7	48146.2
RE0654 – 02	GD 80	682.0	55.0	106.7	8.6	279.8	15.7	48149.2
RE0715 – 70	new ID	3536.0	1127.0	539.3	15.9	867.8	23.7	48183.3
RE0720 – 31[x]	new ID	455.0	45.0	109.5	9.9	369.9	19.0	48159.5
RE0723 – 27	new ID	1833.0	80.0	297.9	15.3	987.6	31.6	48159.5
RE0827 + 28	PG 0824 + 289	714.0	53.0	46.2	7.7	52.8	10.6	48162.4
RE0831 – 53	new ID	32.0	15.0	20.2	5.9	64.2	7.8	48215.2
RE0841 + 03	new ID	2154.0	102.0	238.2	16.8	448.2	22.4	48173.3
RE0902 – 04	new ID	81.0	23.0	26.9	5.6	37.4	8.5	48174.5
RE0907 + 50	PG 0904 + 511	61.0	19.0	35.3	–	47.6	8.5	48163.4
RE1016 – 05[x]	new ID	4744.0	116.0	528.0	19.9	594.4	24.1	48204.3
RE1019 – 14	new ID	286.0	27.0	28.3	5.9	77.0	8.8	48208.3
RE1024 – 30	new ID	288.0	30.0	58.6	8.4	137.7	12.2	48218.9
RE1029 + 45	PG 1026 + 454	196.0	22.0	31.4	4.5	88.7	10.7	48175.4

Table 2.1: cont.

WFC Name	Alternative Name	Survey Count Rates ($c\,ks^{-1}$) PSPC*	1σ*	S1	1σ	S2	1σ	Mean Julian Date
$RE1032+53$	new ID	9068.0	151.0	1136.5	25.8	2689.8	37.4	48174.0
$RE1033-11$	EG 070	242.0	27.0	35.5	7.1	118.0	14.3	48210.8
$RE1036+46$	GD 123	294.0	26.0	57.2	6.7	212.8	12.8	48175.4
$RE1043+49$	new ID	1634.0	69.0	226.6	11.2	477.9	18.2	48175.4
$RE1044+57$	PG $1041+580$	223.0	32.0	49.2	6.7	121.6	9.6	48173.0
$RE1058-38$	new ID	96.0	16.0	43.1	7.7	128.3	11.7	48165.8
$RE1100+71$	PG $1057+719$	1192.0	74.0	120.3	19.9	325.0	20.1	48164.4
$RE1112+24$	TON 61	508.0	42.0	90.1	11.7	88.8	13.2	48204.3
$RE1126+18$	PG $1123+189$	436.0	33.0	183.2	13.0	990.5	34.2	48210.8
$RE1128-02$	PG $1125-026$	50.0	15.0	22.7	4.8	42.2	7.8	48219.4
$RE1148+18$	PG $1145+188$	88.0	18.0	41.6	7.1	100.8	10.0	48215.7
$RE1236+47$	PG $1234+482$	2050.0	30.0	515.6	20.1	1890.2	40.8	48211.3
$RE1257+22$	EG 187	7640.0	163.0	1509.5	37.6	4749.8	54.1	48165.8
$RE1316+29$	HZ 43	87170.0	412.0	12157.6	92.9	36982.6	148.4	48165.8
$RE1340+60$	new ID	45.0	10.0	10.6	4.7	15.4	6.6	48208.8
$RE1431+37$	GD 336	153.0	25.0	22.6	4.5	20.4	6.4	48179.6
$RE1529+48$	new ID	153.0	26.0	17.0	3.4	38.7	6.4	48180.6
$RE1614-08$	new ID	225.0	24.0	17.3	7.1	23.2	9.1	48113.0
$RE1623-39$	CD -38 10980	969.0	54.0	199.5	14.3	605.8	22.3	48116.7
$RE1638+35$	KUV $433-3$	468.0	29.0	51.7	7.1	51.4	7.1	48111.6
$RE1650+40$	new ID	157.0	36.0	17.3	1.0	33.3	8.1	48114.0
$RE1726+58$	PG $1725+587$	1387.0	28.0	47.7	5.7	14.0	–	48183.3
$RE1738+66$	new ID	24.0	10.0	11.4	1.1	11.8	1.1	48183.3
$RE1746-70$	new ID	1248.0	306.0	106.2	18.9	267.6	26.8	48133.5
$RE1800+68$	KUV $18004+6$	812.0	237.0	51.1	2.3	21.5	2.2	48183.3
$RE1820+58$	new ID	1691.0	112.0	104.5	3.4	112.0	4.3	48183.3
$RE1847+01$	BPM 93487	1423.0	75.0	260.7	15.0	697.6	23.9	48146.2
$RE1847-22$	new ID	316.0	46.0	36.3	8.5	48.8	11.4	48142.3
$RE1943+50$	new ID	404.0	82.0	19.6	4.6	23.9	5.4	48192.7
$RE2004-56$	AOO $2000-56$	88.0	27.0	22.8	10.8	41.9	12.6	48153.4
$RE2009-60$	new ID	12040.0	430.0	1274.8	45.6	2626.6	72.3	48153.4
$RE2013+40^{x,d}$	new ID	935.0	34.0	61.8	6.7	33.2	6.4	48176.4
$RE2018-57$	L $210-114$	200.0	55.0	26.1	12.0	32.5	10.5	48155.2
$RE2024-42$	new ID	382.0	39.0	61.2	9.8	181.0	18.9	48157.7
$RE2024+20$	new ID	442.0	30.0	22.3	5.6	18.1	–	48172.0
$RE2029+39$	GD 391	71.0	9.0	23.1	5.8	27.2	7.6	48195.9
$RE2112+50$	GD 394	1282.0	65.0	418.1	13.2	1411.3	23.4	48220.4
$RE2127-22$	new ID	464.0	48.0	57.1	7.8	98.2	10.7	48173.5

Table 2.1: cont.

WFC Name	Alternative Name	Survey Count Rates ($c\,ks^{-1}$) PSPC*	1σ*	S1	1σ	S2	1σ	Mean Julian Date
RE2154 − 30	new ID	158.0	33.0	32.5	6.7	85.5	10.7	48174.5
RE2156 − 41	new ID	1650.0	84.0	166.5	13.4	181.3	12.8	48172.5
RE2156 − 54	new ID	6900.0	175.0	1146.3	29.0	2673.7	43.7	48171.3
RE2207 + 25	new ID	223.0	21.0	18.9	4.7	75.0	11.0	48210.8
RE2210 − 30	new ID	220.0	38.0	75.3	12.4	133.8	12.8	48176.4
RE2214 − 49	new ID	13.0	–	15.6	6.7	1104.8	30.9	48172.5
RE2244 − 32	PHL 0396	87.0	20.0	39.4	16.2	70.9	14.2	48197.4
RE2312 + 10	GD 246	6467.0	114.0	1613.6	35.9	4711.3	57.8	48219.4
RE2324 − 54	new ID	1049.0	82.0	261.3	20.7	656.8	29.3	48192.7
RE2334 − 47	new ID	55.0	22.0	40.6	18.5	364.1	27.3	48197.4
RE2353 − 24	new ID	136.0	25.0	36.9	9.5	64.2	12.2	48215.2

Notes:
* cs^{-1} in the 0.1 − 0.28 keV band
[x] DAO stars.
[a] S1 rate is PV/Cal data.
[b] Rates are after subtraction of K-star component and removal of eclipses (see Barstow et al. 1992).
[c] WFC rates derived from 2RE catalogue (Pye et al. 1995).
[d] PSPC rate is after subtraction of dMe companion, should be treated as upper limit (see Barstow et al. (1995)
'–' in the error column indicates the count rate is an upper limit.

Chapter 3

Optically Derived Stellar Parameters

Overview

The model atmospheres used to fit the ROSAT data, be they stratified or homogeneous, are specified by five main parameters. These are the effective temperature T_{eff}, the surface gravity, the interstellar HI column (N_H), the atmospheric helium abundance (or the mass of the Hydrogen layer M_H, for a stratified model) and a distance/radius related normalisation constant. Since only three independent data points are available from the ROSAT survey, additional information is needed to be able to model the ROSAT data. Photometry provides us with m_v which may be used as a normalisation constant. This still leaves us with four free parameters and only three data points. Two of these parameters, T_{eff} and log g, may be independently derived from the now standard technique of fitting synthetic line profiles to the observed Balmer series of the optical spectrum (eg. Bergeron, Saffer & Liebert 1992). Hence, with the three optically derived paramaters outlined in this chapter, it is possible to examine the role of helium in the ROSAT DA atmospheres and the effects of opacity in general from helium or heavier elements throughout the hot DA temperature range.

3.1 Photometry.

3.1.1 Introduction

It is essential that any model fit to the EUV/X-ray data has an independent flux normalisation at longer wavelengths. The most convenient parameter to use for this purpose is the visual apparent magnitude, m_v. An error of ≈ 0.01 on the V magnitude will only have a 1% effect on the predicted fluxes in the ROSAT bandpasses. This is very much smaller than other sources of error in the analysis such as the 10% systematic errors on the ROSAT data points (see section 4.4).

Over the past two years an extensive programme of observations has been undertaken to obtain UBV photometry for the stars which were either newly identified white dwarfs or for which no previous photometry existed. As ROSAT surveyed the entire sky, optical follow up observations required time on telescopes in both hemispheres. Photometry was obtained for 18 stars in the southern hemisphere and 25 stars in the north.

3.1.2 Observations

In the southern hemisphere, photoelectric photometry was obtained as part of a continuing general photometry programme during 1993-94 using the St. Andrews photometer on the 1.0m telescope based at Sutherland, South Africa and run by the South African Astronomical Observatory (SAAO).

The northern hemisphere stars were observed over a two week period from March 28^{th} – April 9^{th} on the 1.0m Jacobus-Kapteyn telescope (JKT) using an EEV7 CCD chip placed at the cassegrain focus, and a set of Harris UBVRI filters. To increase readout speed, the chip was windowed to 400×400 pixels as opposed to the full 1200×1200 pixels. Standards were adopted from the Kitt peak (Landolt 1983) and RGO (Argyle *et al.* 1988) surveys which covered a range of air mass of $1.0 < X < 2.2$. All of these standards, however, were redder than the white dwarf programme stars. Only on the last night of observing were blue standards observed giving a complete range in colour of $-0.336 < (B - V) < 1.1$ and $-1.245 < (U - B) < 1.1$. However, the observing conditions for this night were not completely photometric, with light cirrus clouds evident. As a result, a small systematic error was introduced into the determination of m_v for the white dwarfs. This is discussed in more detail in the next section.

3.1.3 Analysis

All the target frames were debiassed and flatfielded using the STARLINK package CCDPACK (Draper 1992). The source counts were then measured and the backround subtracted. Dividing by the exposure time gave the source flux in *counts* s^{-1}. An instrumental magnitude is then defined as

$$m_i = c - 2.5log_{10}(flux) \tag{3.1}$$

where c is an arbitrary constant, taken to be 30 in this work to ensure that the magnitude was always positive. The main task in reducing photometric observations is to calibrate the loss of stellar flux as it passes through the Earth's atmosphere for a given observatory and observing period. The two main mechanisms responsible for light loss are Rayleigh scattering and molecular absorption. Dust absorption may also be a problem but care was taken to exclude data from nights which had a high level of dust. A correct magnitude, m_o may be deduced, accounting for the atmospheric absorption by use of the standard star observations and the equation,

$$m_o = m_i - kX \tag{3.2}$$

from Hardie (1962) where X is the path length expressed in units of air mass at the zenith of the observer and k, the *extinction coefficient*, is a measure of the light-loss expressed in magnitudes for a star at the zenith. Standard stars at a range of air mass were observed throughout each night at not more than twenty minute intervals. It is known that the character of the atmosphere is not uniform and that even at a given instant the extinction in various parts of the sky may differ. There is also an obvious limit to the number of standards that can be practically observed in one night. For these reasons all the standard observations from different nights were grouped together to give a mean extinction curve for m_v (figure 3.1a). The scatter in the residuals (figure 3.1b) is caused by the non uniformity of the extinction and was used as a measure of the internal uncertainty for the magnitudes.

In a similar manner, the colour indices for each star may be corrected for extinction using,

$$C_o = C_i - k_c X \tag{3.3}$$

where C_o and C_i are the indices for the star outside and inside the atmosphere respectively. The colour extinction coefficient k_c is clearly the difference between the corresponding extinction coefficients for the individual magnitudes. However, finding k_c independently from the gradient of figure 3.2 is more accurate than taking the difference as the relative colour sensitivity of the telescope + sky system is more constant than the absolute sensitivity.

In order for the magnitudes and colour indices to be useful they must be transformed to a standard photometric system, such as the Johnson system (eg. Johnson 1963). This can be done by using the transformation equations defined by Hardie (1962),

$$C = \alpha C_o + Z_c \tag{3.4}$$

$$V = V_o + \beta C_o + Z_v \tag{3.5}$$

where α and β are the instrumental colour and visual 'scale' constants respectively and Z_c and Z_v instrumental colour and visual zero points respectively.

Combining equs. 3.2 and 3.4 gives,

$$C = \alpha C_i - \alpha' X + Z_c \tag{3.6}$$

where $\alpha' = \alpha k_c$. If we define the difference between the standard magnitude C_s, and the deduced magnitude as $\delta = C_s - C$ and the sum of the squares of this as, $S = \sum \delta^2$ then we can solve for the three unknowns simultaneously such that,

$$\frac{\partial S}{\partial \alpha} = \frac{\partial S}{\partial \alpha'} = \frac{\partial S}{\partial Z} = 0 \tag{3.7}$$

and then k_c is given by α'/α.

As mentioned in the previous section, blue standards were only observed on one night in poor photometric conditions. These stars *are* included in the colour mean extinction curves as colour is a relative measure and is not affected by the drop in flux due to uniform cloud. Of course, cloud is not uniform and as a result several points, lying well outside the 1σ level of the fit were rejected as these were almost certainly caused by a change in the level of cloud between observations, producing a spurious colour.

However, for the V band these blue standards *are not* included in the mean extinction curve as there was a significant drop in flux for these points. This resulted in the standards observed

(a)

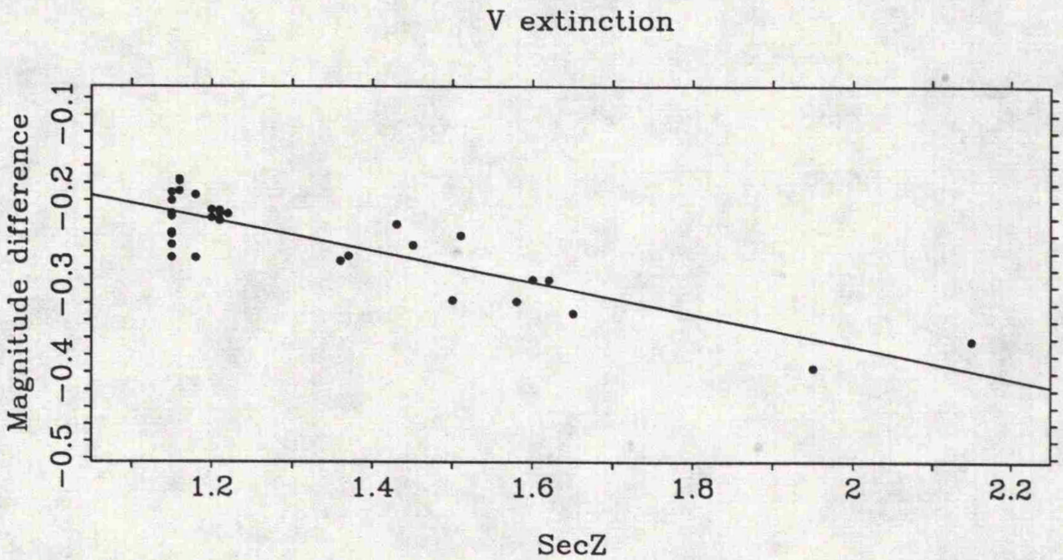

(b)

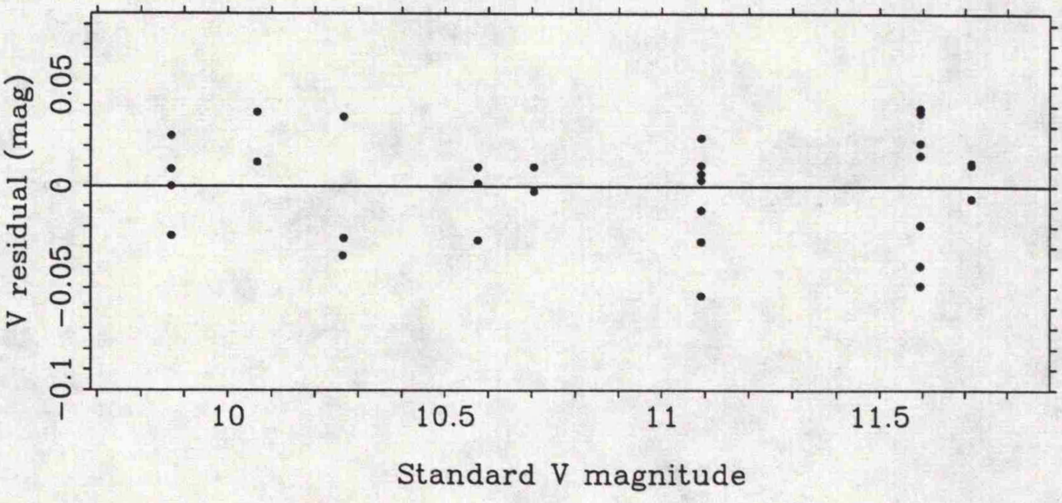

Figure 3.1: (a) The mean extinction curve for the V band. The ordinate shows the difference between the corrected and instrumental magnitudes. The stars are redder than the program white dwarfs (b) The residuals between the standard and observed (extinction corrected and transformed) magnitudes.

(a)

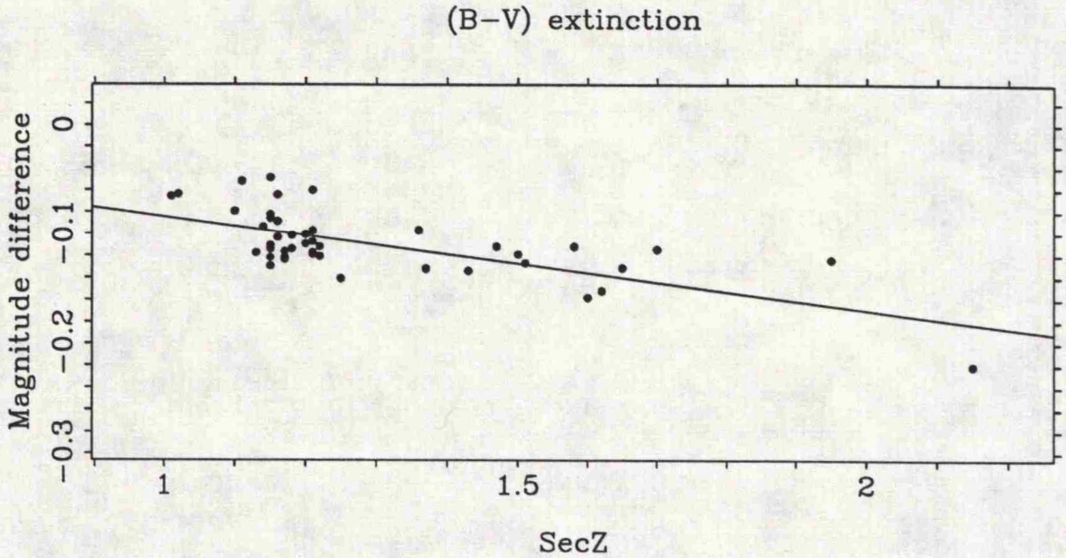

(b)

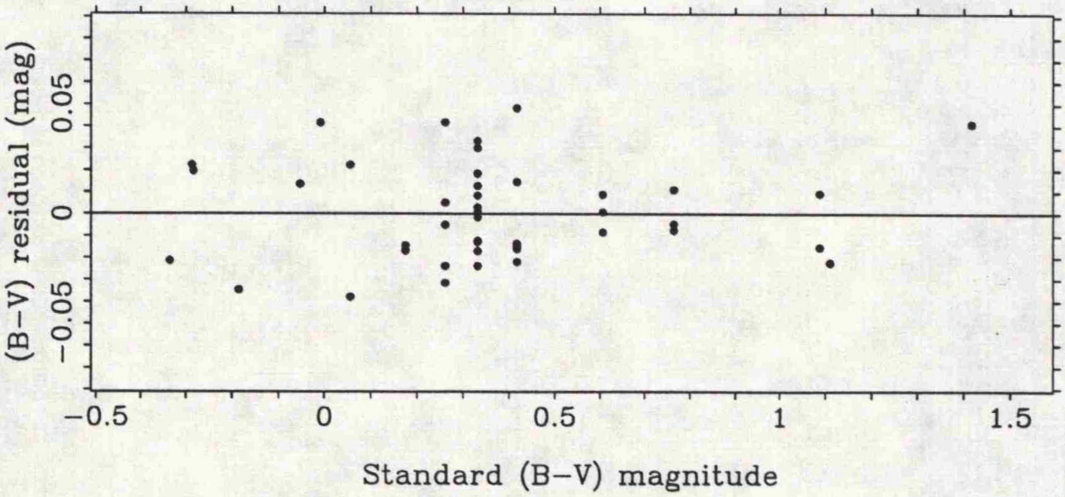

Figure 3.2: (a) The mean extinction curve for (B-V). The ordinate shows the difference between the corrected and instrumental colours. (b) The residuals between the standard and observed (extinction corrected and transformed) colours.

Table 3.1: Colour extinction and transformation coefficients

	k	α	Z	σ
(B-V)	-0.085	0.991	-0.698	0.022
(U-B)	-0.258	1.037	-1.270	0.035

being redder than the target stars. As extinction is roughly proportional to λ^{-4} the extinction coefficient is therefore being underestimated when determining m_v for the white dwarfs. As a consistency check a white dwarf standard GD71 was observed as part of the programme on a night with ideal conditions. Using the extinction and transformation coefficients for m_v derived as above provides an estimate of the systematic error introduced. GD71 has a standard $m_v = 13.032$ (Landolt 1992) and we obtain a value of $m_v = 13.053$, a difference of less than 0.2%. Also one star, RE0521-10, was observed at both the JKT and at the SAAO (the SAAO work used a full range of blue standard stars). RE0521-10 has a visual magnitude of 15.815 ± 0.028 and 15.889 ± 0.018 from the JKT and SAAO work respectively, which agree to within 2σ.

3.1.4 Results.

The method described above was employed to obtain the values of α, k_c and Z_c from the mean extinction curve consisting of 47 standard star observations taken over 7 nights for the colours (B-V) and (U-B). The results are shown in table 3.1. The standard deviations of the residuals in the respective plots are also shown. The same method was then used with equation 3.5 and the 33 standard observations (excluding the blue stars observed in non photometric conditions) in order to obtain the extinction and transformation coefficients for the V magnitudes. These gave, $k_v = -0.185$, $\beta = 0.070$, $Z_v = -7.114$ and $\sigma = 0.028$.

All the data from the SAAO were reduced independently in South Africa in a similar manner and converted to the Cousins' standard system using standards with a full range of colour at varied air masses from Menzies *et al.* (1989). The final results for both hemispheres are listed in table 3.2, with the respective observatories indicated. The value given for RE0521-10 is a weighted average.

For 13 of the stars shown here it was not possible to obtain optical spectra and so they are excluded from the sample of 89 white dwarfs under investigation in this work. However, they are presented in table 3.2 as they have no previously published magnitudes.

Deducing m_v from the spectrum

It was not possible to obtain accurate photometry for all the stars in the sample so the less satisfactory method of estimating m_v from the flux of the optical spectrum was used for 35 stars.

The flux from a spectrum is related to a magnitude by,

$$log f_\lambda(m_x) = -0.4m_x + \log f_\lambda(0) \quad (3.8)$$

Where $f_\lambda(0)$ is the flux for a magnitude of 0.0. The optical spectrum obtained do not extend to the V band but do span the B band. From Zombeck (1990), we have equ. 3.9 in the form,

$$log(f) = -0.4m_b - 8.18\,(\mathrm{erg\,cm^{-2}s^{-1}\AA^{-1}}) \quad (3.9)$$

at 4,400Å (the B band). It is then possible to relate this to the V magnitude as (B-V) is a function of temperature, which is derived from fitting the Balmer lines of the optical spectrum (see next section). A (B-V)$-T_{eff}$ relation was employed using stratified model atmospheres for a star with a canonical log g of 8.0 (eg. see Cheselka *et al.* 1993).

This is a less reliable method due to the relatively inaccurate flux calibration of optical spectra. When mainly interested in the spectral shape rather than absolute flux it is possible to observe in varying atmospheric conditions, even if cloud is present (the flux will be reduced but the spectral shape will be retained). Even if observing conditions are good, high dispersion spectra may require several hours of telescope integration time. Typically, when doing spectroscopic observations only one or two standard stars will be observed per night (as opposed to photometric work where many standards are observed).

Comparing a sample of spectrally deduced magnitudes V_s, against their photometric determinations V_p, provides an estimate of the average errors involved. Doing this for 27 stars observed at Kitt Peak (KP - figure 3.3a) indicates the values determined for V_s are systematically too high. This is most probably due to inacurate spectrophotometric calibration and does not appear to be magnitude dependant. As the average errors on V_p are small they may be regarded as standard. Keeping a gradient of 1, a linear fit was performed on the data giving a constant shift in the V_s axis of 0.15. This is then a measure of the systematic error which is subtracted from all values of V_s for stars observed at KP. A sample of 12 stars from the SAAO showed no similar systematic error. Combining these with the corrected KP values for V_s (figure 3.3b) then enables an estimate of the statistical error from the scatter around the $V_s = V_p$ line yielding $\sigma = 0.3$.

(a)

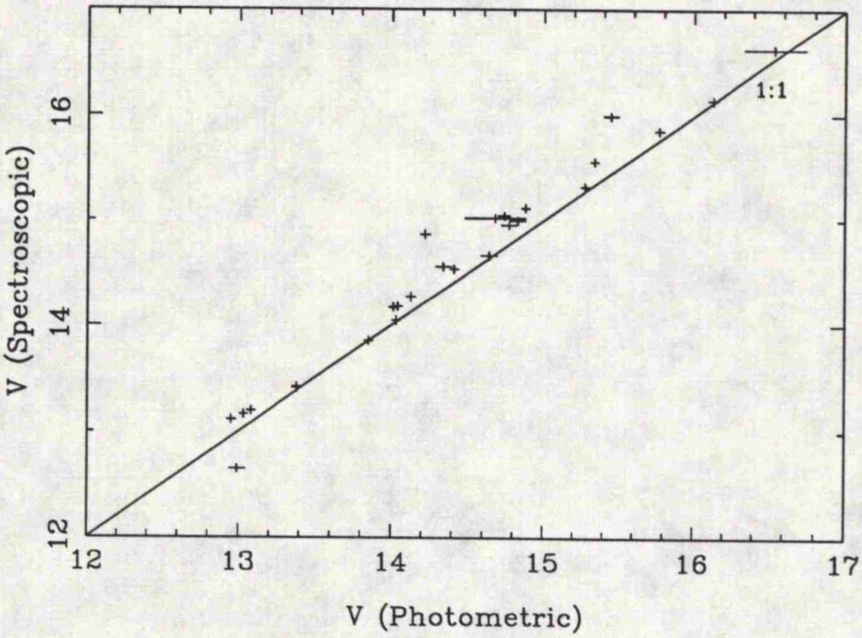

(b)

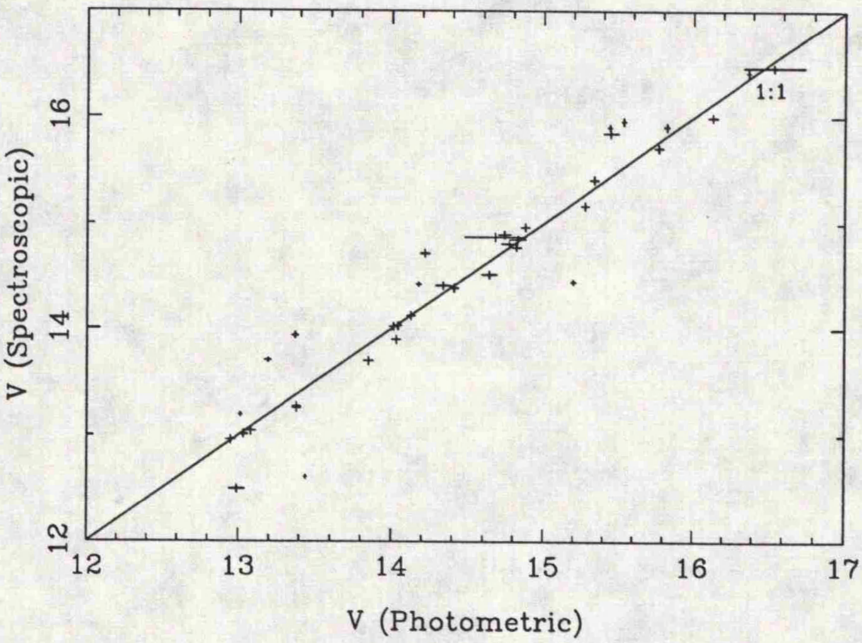

Figure 3.3: (a) V_s against V_p for 27 stars observed at KP showing a systematic error in V_s. (b) The magnitudes from KP after a systematic correction of -0.15 has been applied to V_s plus 12 stars from the SAAO. Errors on V_p are indicated. Errors on V_s for the SAAO objects are from detector counting statistics.

Table 3.2: UBV Photometry of ROSAT DA's

Target	V	1σ	B-V	1σ	U-B	1σ	Obs.
$RE0029-63$	15.314	0.011	-0.352	0.015	-1.148	0.014	SAAO
$RE0415-40^a$	16.444	0.010	-0.307	0.021	-1.249	0.015	SAAO
$RE0503-28^a$	13.912	0.009	-0.359	0.011	-1.233	0.009	SAAO
$RE0512-00^a$	13.827	0.007	-0.258	0.019	-1.024	0.010	SAAO
$RE0512-41$	17.257	0.013	-0.266	0.017	-0.966	0.021	SAAO
$RE0521-10$	15.867	0.015	-0.215	0.015	-1.183	0.013	JKT,SAAO
$RE0534-02^a$	16.198	0.017	-0.296	0.023	-1.036	0.021	SAAO
$RE0550+00$	14.768	0.028	-0.298	0.022	-1.086	0.035	JKT
$RE0550-24$	16.371	0.012	-0.351	0.017	-1.059	0.015	SAAO
$RE0552+15$	13.043	0.028	-0.239	0.022	-1.149	0.035	JKT
$RE0558-37$	14.369	0.006	-0.331	0.003	-1.194	0.002	SAAO
$RE0605-48$	15.825	0.017	-0.214	0.024	-1.177	0.023	SAAO
$RE0623-37$	12.089	0.016	-0.329	0.021	-1.204	0.018	SAAO
$RE0632-05$	15.537	0.015	-0.262	0.020	-1.225	0.017	SAAO
$RE0632-57^a$	15.690	0.016	-0.306	0.021	-1.246	0.018	SAAO
$RE0715-70$	14.178	0.015	-0.351	0.020	-0.230	0.029	SAAO
$RE0841+03$	14.475	0.028	-0.305	0.022	-1.175	0.035	JKT
$RE0902-04$	13.190	0.020	-0.168	0.016	-0.951	0.025	JKT
$RE0957+85^a$	15.747	0.020	-0.265	0.016	-1.192	0.025	JKT
$RE1016-05$	14.306	0.028	-0.033	0.022	-1.554	0.035	JKT
$RE1032+53$	14.455	0.020	-0.276	0.016	-1.195	0.025	JKT
$RE1033-11$	13.028	0.028	-0.181	0.022	-0.983	0.035	JKT
$RE1043+44^a$	16.955	0.028	-0.333	0.022	-1.189	0.035	JKT
$RE1043+49$	16.234	0.028	-0.504	0.022	-1.130	0.035	JKT
$RE1059+51^a$	16.781	0.028	-0.470	0.022	-1.018	0.035	JKT
$RE1112+24^a$	15.773	0.028	-0.291	0.022	-1.145	0.035	JKT
$RE1126+18$	14.127	0.028	-0.280	0.022	-1.187	0.035	JKT
$RE1128+17^a$	16.809	0.028	-0.396	0.022	-1.227	0.035	JKT
$RE1340+60$	16.941	0.020	-0.289	0.016	-1.040	0.025	JKT
$RE1425+53^a$	15.934	0.028	-0.379	0.022	-1.256	0.035	JKT
$RE1431+37$	15.272	0.028	-0.305	0.022	-1.117	0.035	JKT
$RE1440+75^a$	15.216	0.028	-0.151	0.022	-1.101	0.035	JKT
$RE1501+30^a$	15.779	0.020	0.695	0.016	0.206	0.025	JKT
$RE1529+48$	15.083	0.028	-1.476	0.022	-0.863	0.035	JKT
$RE1614-08$	14.013	0.028	-0.295	0.022	-1.141	0.035	JKT
$RE1650+40$	15.831	0.028	-0.251	0.022	-1.269	0.035	JKT
$RE1738+66$	14.606	0.028	-0.343	0.022	-1.250	0.035	JKT
$RE1820+58$	13.949	0.028	-0.279	0.022	-1.194	0.035	JKT
$RE1847-22$	13.720	0.028	-0.212	0.022	-1.123	0.035	JKT
$RE2214-49$	11.708	0.007	-0.341	0.008	-1.205	0.006	SAAO
$RE2324-54$	15.197	0.017	-0.344	0.021	-1.161	0.020	SAAO
$RE2334-47$	13.441	0.007	-0.296	0.010	-1.168	0.009	SAAO
$RE2353-24$	15.444	0.014	-0.066	0.022	-1.175	0.023	SAAO

Note:

[a] WD not included in the full sample of 89 objects.

3.2 Spectroscopy

3.2.1 Introduction

As white dwarfs are thermal sources of radiation with spectra peaking in the EUV and soft X-ray, their spectral slope, and hence their observed count rates in the ROSAT bandpasses are very sensitive to T_{eff}. Therefore tight constraints are required for this parameter, in order to fully utilise the ROSAT survey data. This requires high signal-noise spectra ($s/n \geq 50$) of moderate resolution (≤ 8 Å). Complementary to the programme of photometric observations, a programme on a similar timescale was undertaken to obtain good quality optical spectra for stars for which no previous spectrum existed.

Comparing previously published DA temperatures derived from Balmer line fitting it is seen that systematic differences occur as a result of using different model spectra. For example, Kidder (1991, hereafter K91) used an extended grid of line blanketed homogeneous LTE models by Wesemael *et al.* (1980), whereas Finley, Koester & Basri (1995) employed fully line blanketed stratified LTE models developed by Koester (see Koester 1991). Some of these results are summarised in Barstow *et al.* (1993). Although both these models are effectively equivalent in the case of pure hydrogen atmospheres (very low helium abundance/thick hydrogen layer), the Koester models take into account higher excitation levels of the H atom, which can effect the shape of the Balmer lines (eg. Bergeron, Saffer & Liebert 1992, hereafter BSL). For this reason, spectra used to derive previously published values for T_{eff} and log g for the 48 remaining objects in this sample have also been obtained and reanalysed, thereby providing an internally consistent data set.

3.2.2 Observations and Reductions

Observations were made at two observatories. Those in the southern hemisphere were made in October 1993 and March 1994 using the 1.9m reflector of the SAAO, which is equiped with a Reticon photon counting system (RPCS) detector. The RPCS has two arrays, one which accumulates energy from the source while the other records the brightness of the sky through an adjacent aperture. The grating was blazed to cover a wavelength range of $3600 - 5100$ Å and had a reciprocal dispersion of 75Å mm^{-1}, yielding a resolution of $\approx$ 2.5 Å. Flat-field spectra were obtained at the start and end of each night, and wavelength calibration was provided by a CuAr arc lamp which was observed at least every 20 minutes. Several spectrophotometric standards such as LDS 678A were observed in order to convert the observed counts to flux.

The majority of stars in the northern hemisphere were observed when possible on the 2.3m telescope at the Steward Observatory on Kitt Peak. This instrument is equipped with a Boller & Chivens spectrograph and a UV-flooded Texas Instrument 800 $\times$ 800 CCD detector. The grating was again blazed to cover the spectral range occupied by the Balmer lines and gave a spectral resolution of $\approx$ 8Å. The spectra were then flat-fielded and converted to flux through a standard observation. Details of the observations and reductions of stars studied by Kidder may be found in K91. Identical procedures were used for those stars observed as part of our independent programme.

3.2.3 Determination of Temperature and Gravity

The model atmospheres used in the line fitting procedure were provided by Detlev Koester (eg. Koester 1991) and use a chemically stratified grid of H/He models spanning the temperature range 20,000 – 100,000K and a range in log g from 7.0 – 9.0. Homogeneous models were also available but both structures are equivalent in the limit of zero He/H or large M_H. For most of the stars it was possible to fit the $H_\beta, H_\gamma, H_\delta$ and H_ϵ lines. For those data obtained by K91 often only the H_γ and H_δ lines were available. Prior to the fitting, the lines (as defined by $H_\beta = 4861 \pm 100Å, H_\gamma = 4340 \pm 75Å, H_\delta = 4101 \pm 50Å, H_\epsilon = 3970 \pm 50Å$) were 'cut' out of the spectrum. These boundaries were chosen to include most of the equivalent width of the line in question without overlapping any adjacent profiles.

In all the observations the detector oversamples the spectral resolution of the instrument and so the data points were grouped in order to roughly match the resolution used. As DA white dwarfs are defined as having no detectable helium in their optical spectrum the value of M_H was set to its maximum value (equivalent to a pure hydrogen envelope) and frozen.

The modelling was performed using the program XSPEC (Shafer *et al.* 1991) which uses the method of minimizing χ^2 to obtain a best fit model spectrum (see Appendix A). An independent normalisation constant was applied to each line ensuring that the fitting of the profile was independent of the local slope of the continuum and hence reducing the effect of any systematic errors in the flux calibration of the spectrum. All the lines were fit simultaneously until the minimum χ^2 was achieved. In dealing with CCD spectra it is difficult to determine errors on individual points so no errors were included in the initial fit. From the residuals of the first fit a systematic deviation in the spectral slope between model and data was often evident, arising from second-order errors in the flux calibration. This was corrected for and also an average error on the data points was estimated from the scatter on the residuals between the best fitting model and the observed spectrum which was then included in subsequent fits. This resulted in no change to the best-fitting parameters but, with the inclusion of errors on the data points, produced a lower reduced chi-squared, χ_r^2. To make a sensible estimate of the uncertainty in the fitted parameters, the χ_r^2 should be less than ≈ 2, and this was achieved in all cases. Example fits are shown in figure 3.4 of the very hot DA RE0029-63 and the cooler object RE0148-25. Error ranges were obtained by allowing the model parameters to vary until the $\Delta\chi^2$ reached a value corresponding to the 1σ level for the 2 degrees of freedom (T_{eff} and log g; see Appendix 1), It should be noted that the errors quoted only include instrumental and statistical errors and do not take into account any possible uncertainties in the model spectra.

3.2.4 Results

The values obtained for T_{eff} and logg from the profile fitting for the whole sample of 89 objects are given in table 3.4. The 1σ errors are shown as lower and upper bounds to each parameter. Also included here are the adopted values for m_v for each star in the sample. Where several photometric observations were available, including the results in the previous section and published photometry (which existed for 47 stars), a weighted average was taken. Objects for which m_v was estimated from the optical spectrum are indicated.

A potentially important effect that may affect the results of Balmer line fitting, is discussed by Bergeron, Saffer & Liebert (1992). They have shown that for DA stars, homogeneous helium abundances of He/H $\approx 10^{-5} - 10^{-4}$ which have no detectable HeII absorption feature at 4686 Å, can significantly reduce the derived effective temperature compared to that for a pure hydrogen atmosphere. For example, they show that a 52,000K DA with a homogeneous helium abundance

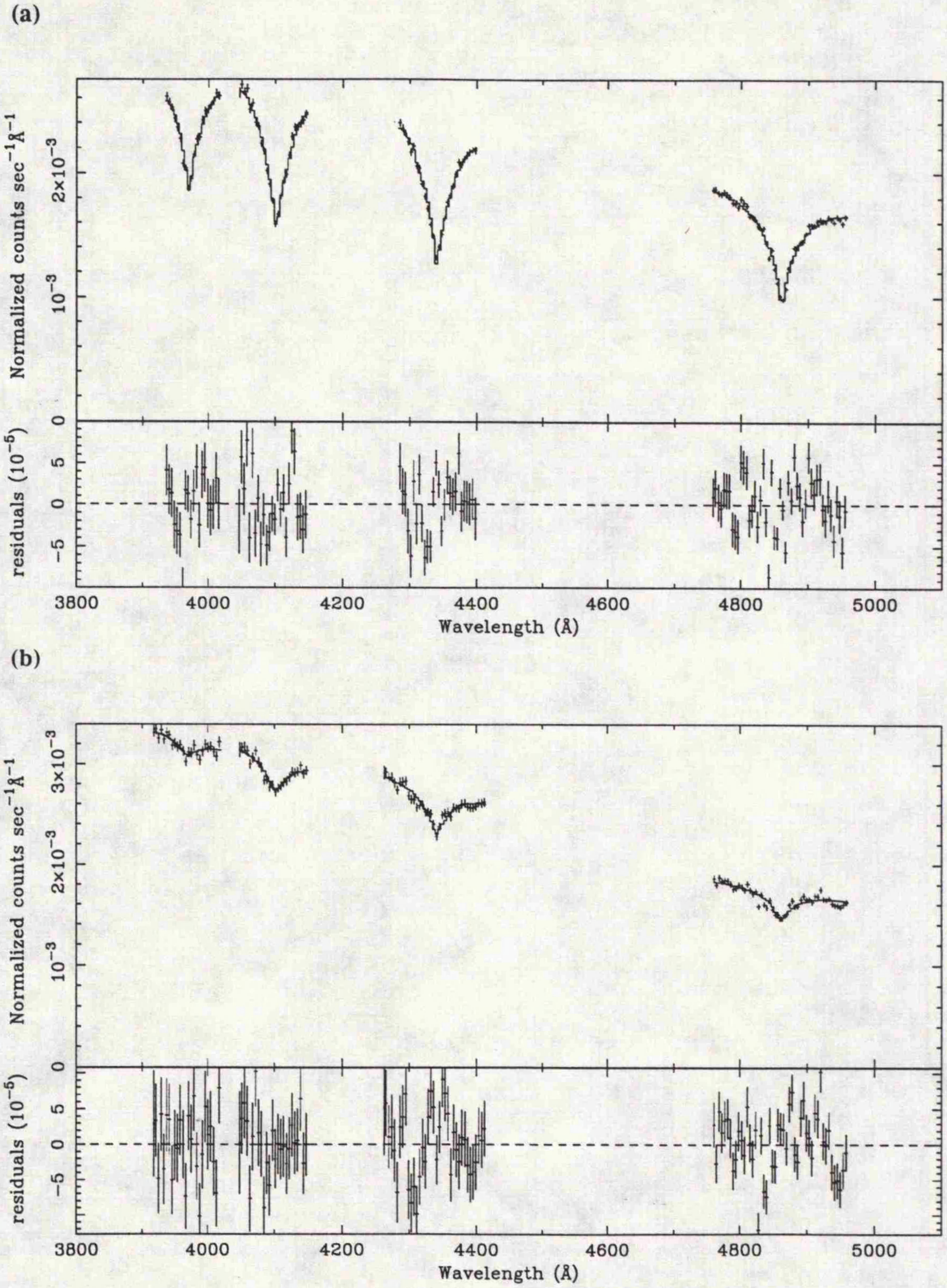

Figure 3.4: Example spectral fits for two stars where all $H_{\beta-\epsilon}$ lines are available.
(a) RE0148-25: T_{eff} = 24,540K, log g= 7.84 (χ_r^2 = 1.68)
(b) RE0029-63: T_{eff} = 60,595K, log g= 7.97 (χ_r^2 = 1.74)

of He/H = 10^{-4} could be interpreted as having $T_{eff} = 60,000K$ if it were assumed to be pure H. This effect is even stronger at higher temperatures, giving a discrepancy as high as 25% around 80,000K. If these levels of He were really present in the hot DAs the net effect would be a non linear compression of the temperature scale towards the hot end. Nevertheless, comparisons between individual objects would still be valid unless the abundances of helium varied considerably at a given T_{eff}.

However, Napiwotzki (1995) has recently demonstrated that the affect trace helium has on the Balmer lines is exaggerated due to the assumption of LTE. Also, observations of hot DAs with EUVE (Barstow, Holberg & Koester 1994) have shown no evidence for an abundance of helium as high as this in any DA, if in fact it is present at all. This suggests, for the moment, that helium has a minimal effect on the hot DA temperature scale, and it was therefore chosen to adopt a temperature scale derived from pure hydrogen fits. The same EUVE observations as well as IUE observations (Holberg *et al.* 1993) do on the other hand show evidence for many trace elements heavier than helium in almost all of the very hot DAs. These elements may well have a similar effect on the Balmer lines as helium. This is being investigated but the evidence is conflicting. Dreizler & Werner (1993) found that with non-LTE model atmospheres, the inclusion of line blanketing from Fe-group elements had a very small effect on the hydrogen line profiles. Alternatively, Lanz & Hubeny (1995) found that the inclusion of heavy elements in their non LTE-models did have a significant effect on the profiles. This matter needs to be speedily resolved but until then one can only proceed with caution with regard to a temperature scale based on pure hydrogen envelopes.

3.2.5 Comparisons with previous studies – (*Mass Distribution*)

The sample of DAs studied in this work were selected purely on the basis that they were detected in the EUV/X-ray *ROSAT all-sky survey*. This presents a bias in only detecting the very hot objects (> $20000K$). It is important to investigate any effects of this selection bias by comparing the sample with other studies. One way to do this is by comparing *mass distributions*. There are several methods available for determining a DA mass. Once the temperature and gravity are known the mass can be found from a theoretical mass-radius relationship, with gravity being the ratio of the mass to the square of the radius.

There are several studies of mass distributions of large samples of DA white dwarfs available in the literature. The majority of these are summarised in BSL, who compare previous results with their own findings. Most of these works are dominated by objects below $T_{eff} \sim 15000$K due to their photometric method for deriving temperature and gravity (and also as most DAs have temperatures below this). Several sources of uncertainty in deriving T_{eff} and log g by this method in this temperature regime are discussed by BSL. They also show that for $T_{eff} > 15000$K optical Balmer line fitting provides a far more accurate way of determining these parameters, which is the method they use. For this reason, we compare our results with those of BSL. A further study is that of Kidder (1991) who studied 101 hot DAs, the majority of which were selected on the basis of detection during the *EXOSAT* and *Einstein* X-ray missions. However, he assumed that the masses and radii follow the Hamada & Salpeter (1961) zero-temperature mass-radius relation for degenerate ^{12}C as do all the other works apart from that by BSL. They point out that for $T_{eff} > 12000$K finite temperature effects are important and can result in underestimates of the masses. Instead they estimate radius and hence mass using the evolutionary models of Wood (1990) for DAs with pure carbon cores surrounded by an envelope with composition $\log(M_{He}/M_*) = -4$. These models were also employed in our work spanning a mass range of $0.4M_\odot - 1.0M_\odot$ in steps of $0.1M_\odot$.

As the evolutionary models only cover this specific mass range, 8 stars with masses apparently above $1M_\odot$ were not included when finding the mean of the mass distribution. The mean of the BSL mass distribution was recalculated excluding 10 stars with masses either above $1M_\odot$ or below $0.4M_\odot$ to enable a fair comparison. These values are shown in table 3.3, together with the respective sample dispesions. Also shown are the mean and dispersions of the surface gravity distributions for both samples. These were calculated including all 89 stars in the ROSAT sample and all 129 stars in the BSL sample. The ROSAT sample has a weighted mean log g of 7.873 and a weighted mean mass of $0.562M_\odot$. The actual surface gravity and mass distributions of the sample are shown in comparison to those of BSL in figure 3.6 and figure 3.5 respectively.

Comparing samples we see that the mass distributions are very similar, both having well defined peaks around $0.5M_\odot - 0.6M_\odot$ with the BSL peak being less sharp due to a larger sample size.

Table 3.3: Comparison of our results with those of BSL.

	$< \log g >$	σ	$< M/M_{\odot} >$	σ
BSL (1992)	7.909	0.257	0.573	0.109
This work	7.899	0.377	0.597	0.112

The mean of the ROSAT sample is higher due to a broader peak and a relatively larger number of more massive stars. It can be seen from figure 3.6 that the surface gravity distribution peaks around log g = 7.75 (lower than that of BSL which peaks around log g = 7.85), and then falls off less rapidly than BSL toward high gravity. A lower peak in the surface gravity distribution is to be expected as ROSAT detects hotter, and therefore younger stars which have lower surface gravities. However, the mean surface gravity is very similar to that of BSL due to a larger population of high gravity ($\log g = 8.5 - 9.0$) stars. It appears that through EUV/X-ray observations, ROSAT detects a larger than expected number of hot, very high gravity massive DAs. The prescence of this 'high gravity tail' in the distribution is an anomaly and it will be seen later that these stars do not fit in with evolutionary models (see figure 4.15) requiring another explanation, possibly white dwarf merging.

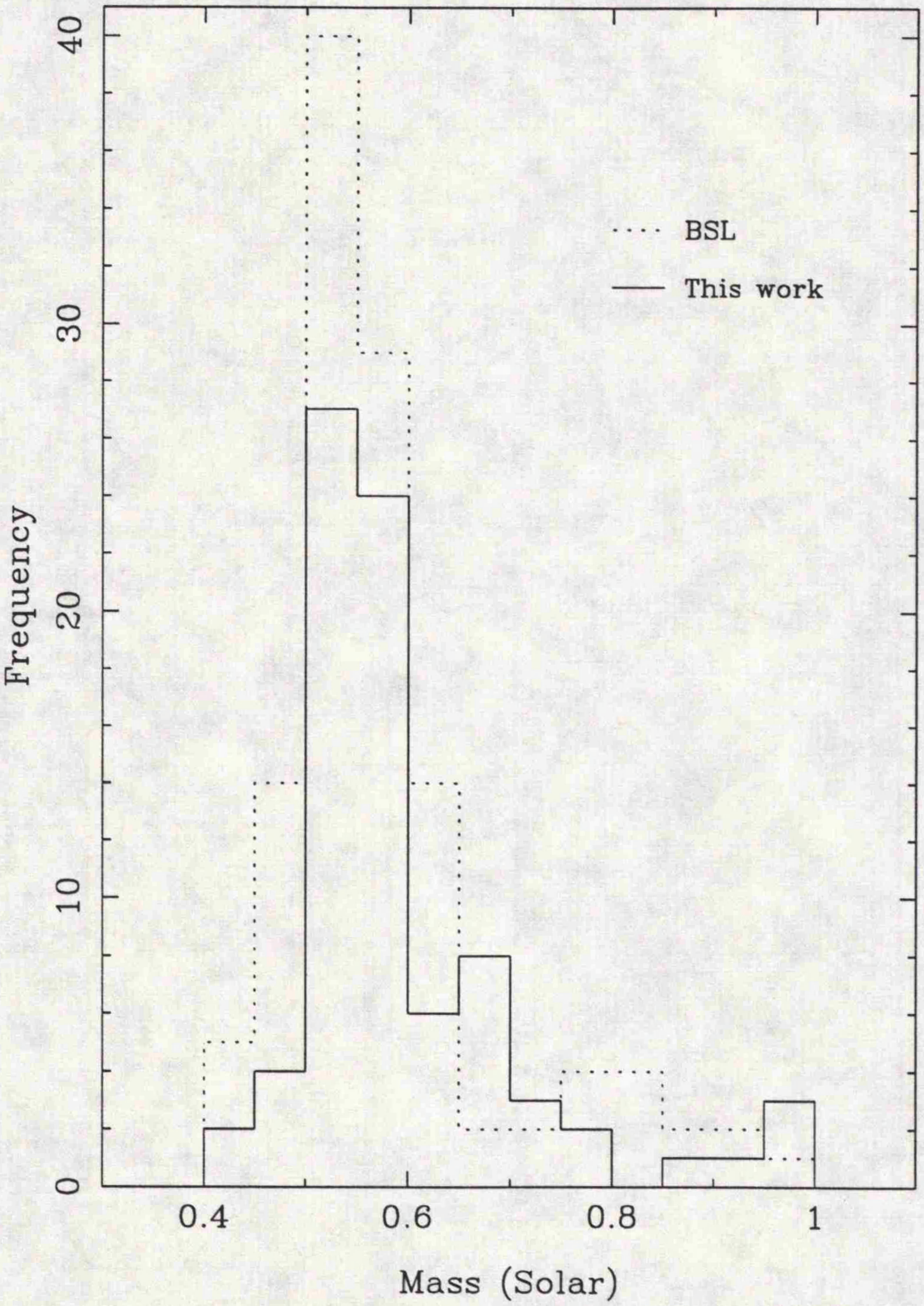

Figure 3.5: Derived mass distributions including only stars with $0.4 < M/M_{\odot} < 1.0$ for 81 objects from the ROSAT sample and 119 stars from BSL.

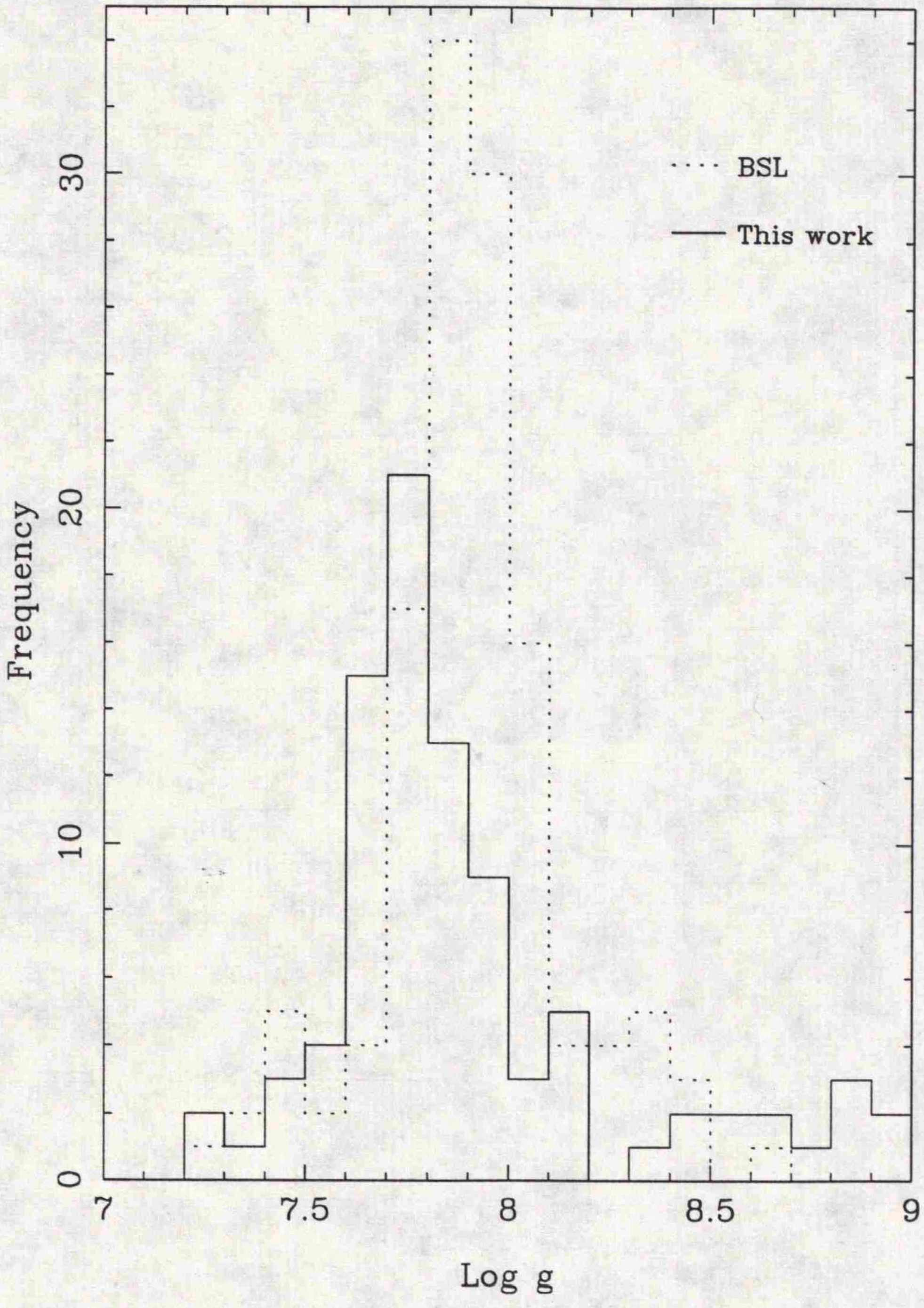

Figure 3.6: Distributions of log g for all 89 stars in the ROSAT sample and all 129 stars in BSL.

Table 3.4: Summary of Derived Stellar Parameters

Target	m_v	1σ err.	T_{eff} (K)	1σ bounds	log g (cm s^{-2})	1σ bounds
RE0003 + 43	16.82	0.30	46205	44476 – 47850	8.85	8.73 – 8.97
RE0007 + 33	13.85	0.01	47936	46839 – 49086	7.77	7.67 – 7.86
RE0029 – 63	15.314	0.011	60595	58130 – 63800	7.97	7.76 – 8.16
RE0053 – 32	13.37	0.02	34684	34382 – 34998	7.89	7.82 – 7.96
RE0108 – 35*	14.76	0.30	28580	28320 – 28835	7.90	7.83 – 7.97
RE0134 – 16	13.96	0.03	44850	42786 – 48296	7.96	7.70 – 8.32
RE0138 + 25	15.87	0.03	38964	38458 – 40708	9.00	8.92 – 9.00
RE0148 – 25*	14.69	0.30	24540	24300 – 24765	7.84	7.79 – 7.92
RE0151 + 67	14.41	0.02	30120	29874 – 30338	7.70	7.62 – 7.77
RE0230 – 47	14.79	0.30	63400	62680 – 67280	7.43	7.25 – 7.67
RE0235 + 03	12.56	0.05	62947	61481 – 64336	7.53	7.45 – 7.62
RE0237 – 12*	14.92	0.30	31290	30970 – 31710	8.44	8.35 – 8.53
RE0322 – 53	14.83	0.3	32860	32445 – 33135	7.66	7.62 – 7.78
RE0348 – 00	14.04	0.02	42373	41577 – 43473	9.00	8.90 – 9.00
RE0350 + 17	13.65	0.05	34200	33600 – 34800	8.80	8.52 – 9.08
RE0457 – 28	13.951	0.009	58080	55875 – 60170	7.90	7.78 – 8.07
RE0505 + 52	11.73	0.01	57340	56040 – 58670	7.48	7.34 – 7.58
RE0512 – 41	17.257	0.013	53960	51400 – 58435	7.62	7.33 – 7.86
RE0521 – 10	15.815	0.028	31770	31090 – 32160	8.70	8.61 – 8.82
RE0550 + 00	14.773	0.024	45748	44360 – 47405	7.79	7.66 – 7.90
RE0550 – 24	16.371	0.012	51870	48750 – 56400	7.29	7.02 – 7.59
RE0552 + 15	13.032	0.009	32008	31962 – 32287	7.70	7.63 – 7.73
RE0558 – 37	14.369	0.006	70275	66400 – 78780	7.37	7.13 – 7.50
RE0605 – 48	15.825	0.017	33040	32260 – 34370	7.80	7.57 – 8.26
RE0623 – 37	12.089	0.001	62280	60590 – 64140	7.22	7.13 – 7.40
RE0632 – 05	15.537	0.015	41765	40330 – 44420	8.51	8.35 – 8.65
RE0645 – 16	8.35	0.1	24700	23700 – 25700	8.65	8.35 – 8.95
RE0654 – 02	14.82	0.03	32280	31740 – 32840	8.34	8.23 – 8.45
RE0715 – 70	14.178	0.015	44300	43310 – 45445	7.69	7.62 – 7.80
RE0720 – 31	14.87	0.04	53630	52400 – 54525	7.64	7.54 – 7.74
RE0723 – 27*	14.60	0.30	37120	36390 – 37860	7.75	7.65 – 7.85
RE0827 + 28	14.22	0.03	51934	48457 – 56007	8.00	7.73 – 8.22
RE0831 – 53*	14.65	0.30	29330	28970 – 29590	7.79	7.75 – 7.89
RE0841 + 03	14.475	0.028	36605	36180 – 37015	7.69	7.64 – 7.76
RE0902 – 04	13.190	0.020	23310	22560 – 24120	7.74	7.64 – 7.83
RE0907 + 50	16.54	0.2	33459	32882 – 34239	7.86	7.70 – 7.99
RE1016 – 05[a]	14.21	0.05	53827	52629 – 55931	8.08	7.98 – 8.17
RE1019 – 14*	14.93	0.30	31340	30895 – 31680	7.79	7.70 – 7.89
RE1024 – 30*	16.67	0.30	36610	35780 – 38360	8.69	8.50 – 8.80
RE1029 + 45	16.13	0.03	34224	33889 – 34740	7.85	7.76 – 7.93

Table 3.4: continued

Target	m_v	1σ err.	T_{eff} (K)	1σ bounds	log g (cm s^{-2})	1σ bounds
RE1032 + 53	14.455	0.020	44980	44210 – 45310	7.68	7.64 – 7.77
RE1033 – 11	13.012	0.009	22790	22570 – 23030	7.57	7.53 – 7.60
RE1036 + 46	14.34	0.05	28766	28349 – 29236	7.92	7.79 – 8.06
RE1043 + 49	16.234	0.028	47560	46550 – 48630	7.62	7.52 – 7.70
RE1044 + 57	14.64	0.05	29016	28750 – 29304	7.79	7.71 – 7.87
RE1058 – 38*	13.78	0.30	27970	27680 – 28200	7.88	7.81 – 7.95
RE1100 + 71	14.68	0.2	39555	38747 – 40503	7.66	7.54 – 7.78
RE1112 + 24	15.773	0.028	38970	38620 – 39780	7.91	7.81 – 7.96
RE1126 + 18	14.127	0.028	55640	54770 – 56940	7.62	7.54 – 7.69
RE1128 – 02*	15.73	0.30	31280	30840 – 31770	8.11	8.00 – 8.21
RE1148 + 18	14.33	0.30	25107	24764 – 25489	7.81	7.73 – 7.87
RE1236 + 47	14.38	0.05	55570	54540 – 56720	7.57	7.49 – 7.64
RE1257 + 22	13.38	0.02	37880	37209 – 38584	7.69	7.59 – 7.79
RE1316 + 29[b]	12.99	0.05	49000	47000 – 51000	7.70	7.50 – 7.90
RE1340 + 60	16.941	0.020	42970	42030 – 44240	7.68	7.57 – 7.84
RE1431 + 37	15.277	0.016	34419	33582 – 35135	7.66	7.52 – 7.82
RE1529 + 48	15.083	0.028	46230	45540 – 47000	7.70	7.62 – 7.75
RE1614 – 08	14.013	0.028	38500	38160 – 38890	7.85	7.79 – 7.90
RE1623 – 39	11.00	0.01	24760	24333 – 24805	7.92	7.88 – 8.09
RE1638 + 35	14.83	0.05	36056	35479 – 36662	7.71	7.61 – 7.80
RE1650 + 40	15.831	0.028	37850	36800 – 38430	7.95	7.81 – 8.12
RE1726 + 58	15.45	0.05	54550	49616 – 58835	8.49	8.25 – 8.77
RE1738 + 66	14.606	0.028	88010	85400 – 90400	7.79	7.70 – 7.93
RE1746 – 70*	16.60	0.30	51050	48410 – 53930	8.84	8.68 – 9.00
RE1800 + 68	14.74	0.04	43701	42700 – 44759	7.80	7.68 – 7.92
RE1820 + 58	13.949	0.028	45330	44600 – 46290	7.73	7.68 – 7.81
RE1847 + 01	12.95	0.05	28744	28485 – 29017	7.72	7.65 – 7.79
RE1847 – 22	13.720	0.028	31920	31540 – 32260	8.00	7.91 – 8.09
RE1943 + 50*	14.62	0.30	33500	33330 – 33690	7.86	7.82 – 7.90
RE2004 – 56	15.05	0.30	44456	43381 – 45327	7.54	7.43 – 7.66
RE2009 – 60	13.59	0.30	44200	43650 – 44800	8.14	8.03 – 8.22
RE2013 + 40	14.6	0.60	47057	45680 – 48230	7.74	7.49 – 8.04
RE2018 – 57*	13.61	0.30	26579	26034 – 26892	7.78	7.72 – 7.85
RE2024 – 42*	14.74	0.30	28597	28230 – 28988	8.54	8.38 – 8.67
RE2024 + 20*	16.59	0.30	50564	49332 – 51810	7.96	7.83 – 8.06
RE2029 + 39	13.38	0.01	22153	21749 – 22560	7.79	7.72 – 7.87
RE2112 + 50	13.08	0.02	38866	38139 – 39634	7.84	7.74 – 7.94
RE2127 – 22*	14.66	0.30	48297	46455 – 49934	7.69	7.56 – 7.82

Table 3.4: continued

Target	m_v	1σ err.	T_{eff} (K)	1σ bounds	log g ($cm\ s^{-2}$)	1σ bounds
RE2154 − 30*	14.17	0.30	28741	28363 − 29152	8.18	8.08 − 8.26
RE2156 − 41*	15.38	0.30	49764	46513 − 53131	7.75	7.57 − 7.92
RE2156 − 54*	14.44	0.30	45860	44600 − 47200	7.74	7.64 − 7.83
RE2207 + 25*	14.58	0.30	24610	24490 − 24690	8.16	8.14 − 8.20
RE2210 − 30*	14.79	0.30	28268	27823 − 28640	7.60	7.53 − 7.72
RE2214 − 49	11.708	0.007	65600	63790 − 68510	7.42	7.24 − 7.57
RE2244 − 32*	15.66	0.30	31692	31312 − 32188	8.07	7.96 − 8.17
RE2312 + 10	13.09	0.01	57380	56190 − 58670	7.86	7.78 − 7.93
RE2324 − 54	15.197	0.017	45860	44490 − 47320	7.73	7.61 − 7.82
RE2334 − 47	13.441	0.007	56682	54883 − 59500	7.64	7.57 − 7.78
RE2353 − 24	15.444	0.014	29120	28720 − 29620	8.14	8.01 − 8.21

Notes:

* m_v determined from spectral flux.

[a] V magnitude is taken from Thorstensen, Vennes & Bowyer (1995) – see section 4.7.

[b] Values for HZ43 are from Napiwotzki *et al.* (1993).

Chapter 4

Studies of the DA Atmospheres

4.1 Model Atmosphere Calculations

With the parameters described in the previous chapter it is now possible to examine the role of helium in the DA atmospheres. At our disposal are both homogeneous and stratified models calculated from the atmosphere code of Koester (1991). The former assumes a homogeneous distribution of hydrogen and helium under LTE conditions and covers a range in helium abundance of $-8 > \log \mathrm{He/H} > -3$. The stratified structure assumes a plane parallel geometry with a thin layer of hydrogen denoted by its mass M_H, and covers the approximate range $10^{-16} > M_{H(\odot)} > 10^{-11}$ which overlies a helium atmosphere and also assumes LTE conditions. The assumption of LTE has been examined by Barstow (1990). By comparing LTE and non-LTE H+He models he finds that over the range of surface gravity covered here, the EUV/X-ray data only become sensitive to departures from LTE at very high temperatures ($> 10^5$K). Since the DAs in the ROSAT sample have temperatures cooler than this, the errors due to the LTE approximation will, therefore, be small. All of the model calculations include full line blanketing from hydrogen and helium.

It has long been noted that a layered structure is much more physically realistic than a homogeneous structure for a DA white dwarf atmosphere. Schatzmann (1958) originally proposed that the high surface gravities of white dwarfs (typically $\log g = 8.0$) together with electric forces in the atmosphere would cause the heavier elements to settle below the photosphere on a relatively short timescale (of the order of a few years) leaving a layer of pure hydrogen on top. Koester

(1991) has demonstrated that a stratified structure is able to explain certain anomalies in several DAs, such as the absence of a HeII (4686Å) line in the spectrum of G191-B2B for a layer mass which reproduces the EXOSAT count rates. The fraction of helium homogeneously mixed which reproduces the EXOSAT data also predicts a significant HeII line. Conversely, recent results by Bergeron *et al.* (1994) show that ROSAT observations of DAO white dwarfs (three known DAOs are in this sample) can only be explained by a homogeneous structure. All these DAO stars appear to be in close binary systems. Some common evolution between white dwarf and secondary could be the explanation for the homogeneous atmospheres and this needs to be investigated. In light of this work and the fundamental question of whether DA white dwarfs have thick hydrogen layers with helium or heavier elements homogeneously mixed in them or thin hydrogen layers with the opacity originating at the H/He diffusion boundary, both model structures were used in the analyse presented here.

Grids of models were calculated to cover fully the parameter space spanned by the DAs in the ROSAT sample. Both structures covered a range in temperature of $20,000\mathrm{K} < T_{eff} < 100,000\mathrm{K}$ and in gravity of $7.0 < \log g < 9.0$ with log g sampled every 0.5 dex and temperature every 5,000K above 30,000K but every 1,000K below 30,000K as this is where the flux changes most rapidly with increasing T_{eff}. A model spectrum for a particular set of parameters is then generated by interpolating between the model grid in question.

4.2 Sensitivity of EUV Flux to Model Parameters

When interpolating between models to deduce the structure and composition of a stellar atmosphere it is necessary to understand the magnitude of the effect that changing a model parameter has on the emergent flux. The EUV flux is heavily attenuated by interstellar matter. Figure 4.1 shows this absorption as a function of increasing N_H for each of the ROSAT survey bandpasses. The increasing opacity with decreasing band energy (due to the energy dependence of the photoelectric cross section of the interstellar medium below the Lyman limit) is apparent with a column of only $10^{18}\,\mathrm{cm}^{-2}$ reducing the S2 flux by 10%. With a column of just $10^{19}\,\mathrm{cm}^{-2}$ the S2 flux is more than halved.

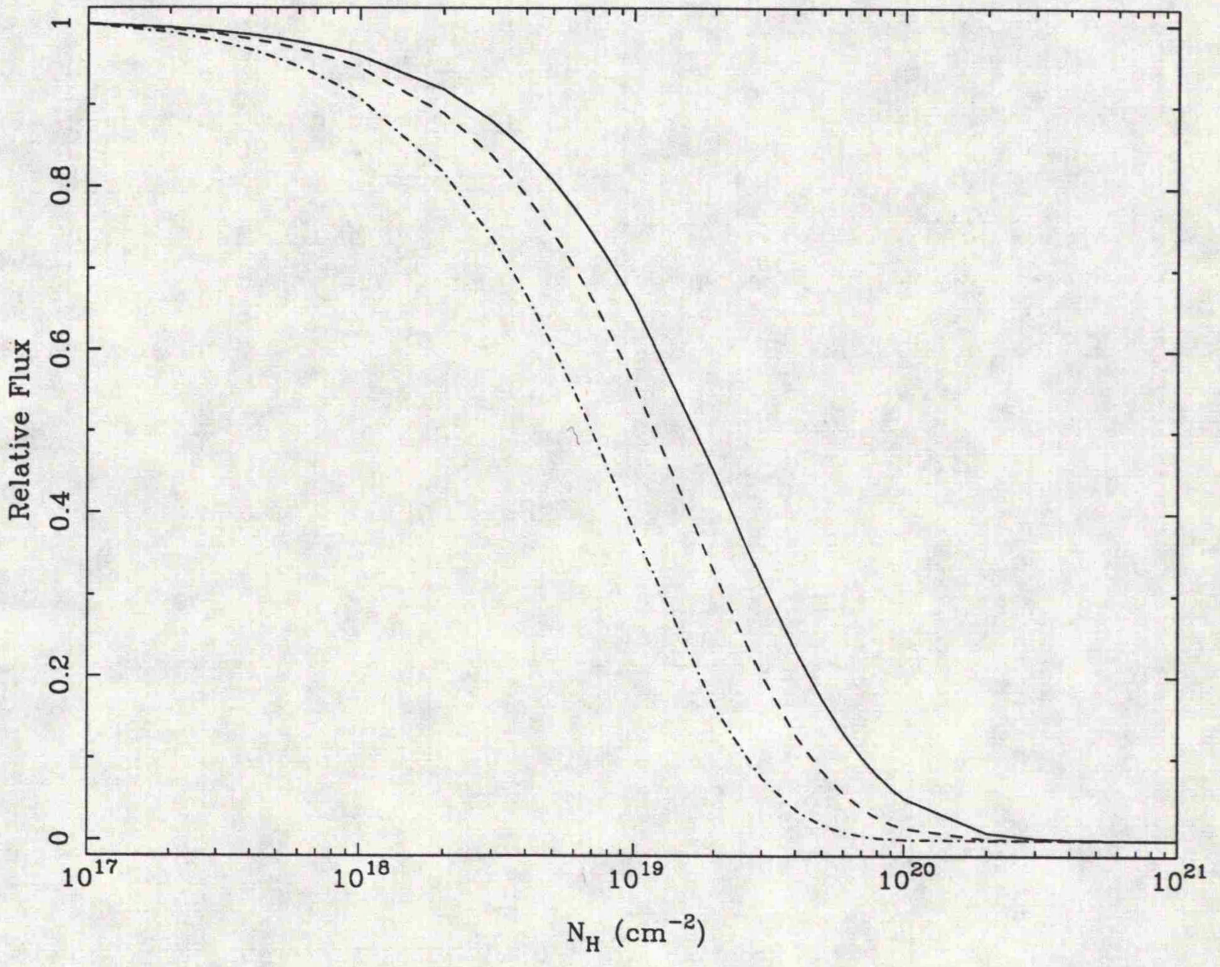

Figure 4.1: The effect of interstellar H column density N_H, on the EUV/X-ray fluxes. Predicted fluxes are for $T_{eff} = 40,000$K, and log g = 8.0 for a pure hydrogen stratified atmosphere and are normalised on the plot to $N_H = 10^{17}$ cm^{-2}. Interstellar HeI was set to cosmic abundance (one tenth the value of N_H). Model used was that of Rumph, Bowyer & Vennes (1994). PSPC - solid line, S1a - dashed line, S2a - dash-dot line.

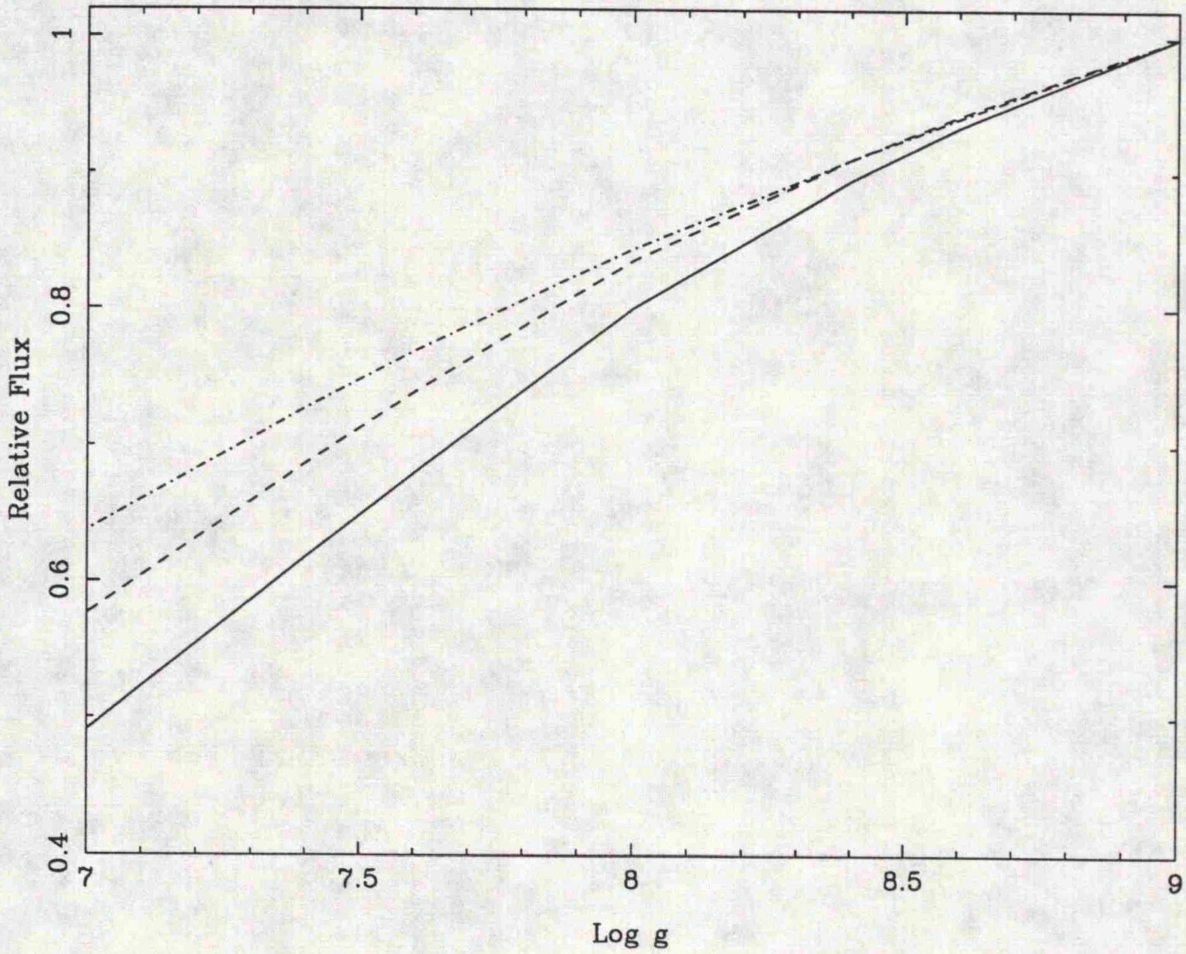

Figure 4.2: The effect of decreasing surface gravity on the EUV/X-ray fluxes. Predicted fluxes are for a homogeneous pure hydrogen atmosphere (He/H = 10^{-8}) with $T_{eff} = 30,000$K and are normalised on the plot to log g = 9.0. PSPC - solid line, S1a - dashed line, S2a - dash-dot line.

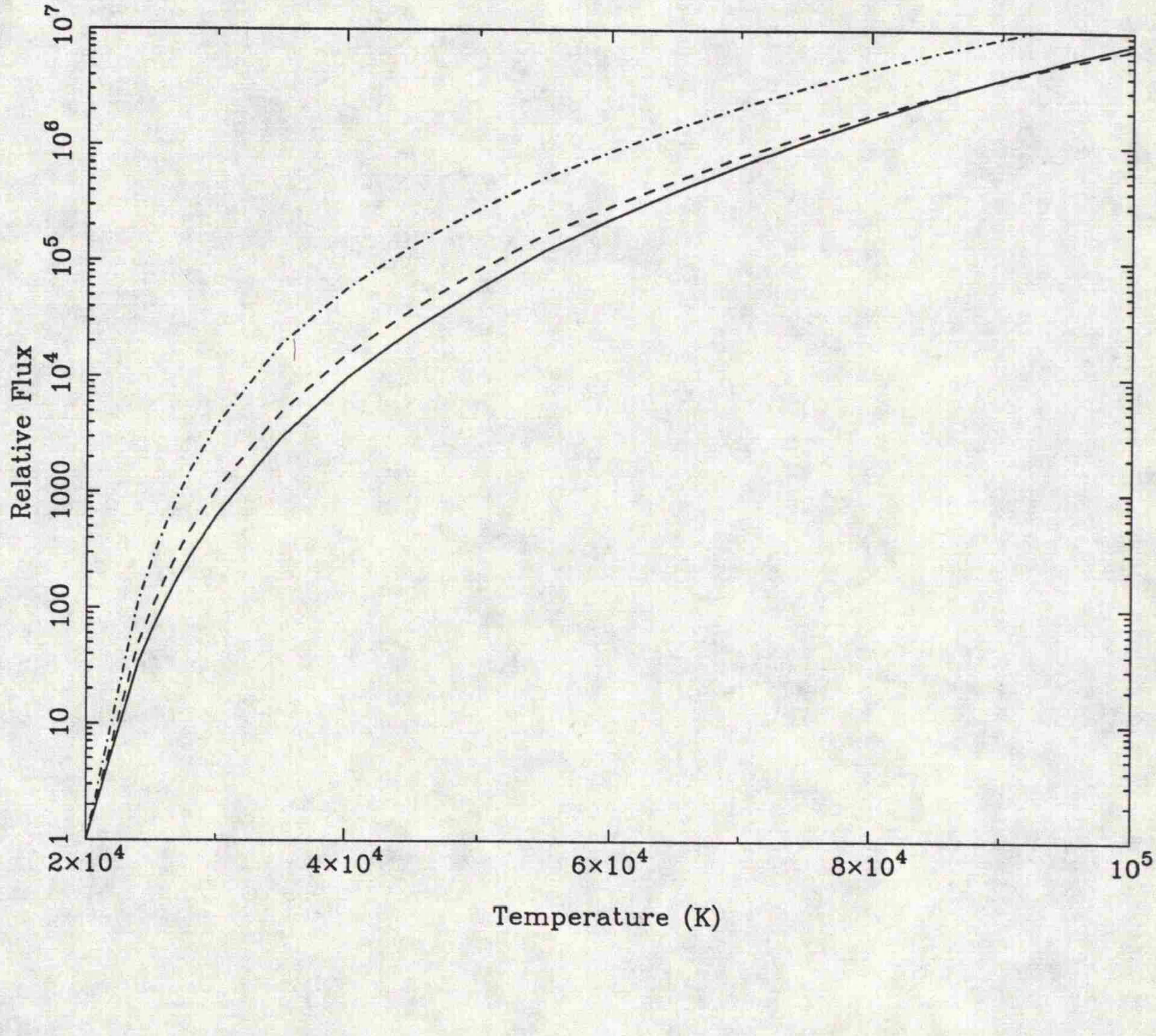

Figure 4.3: The effect of increasing temperature on the EUV/X-ray fluxes. Predicted fluxes are for a stratified pure hydrogen atmosphere ($M_H \approx 10^{-12}$) with log g = 7.0 and are normalised on the plot to $T_{eff} = 20,000$K. PSPC - solid line, S1a - dashed line, S2a - dash-dot line.

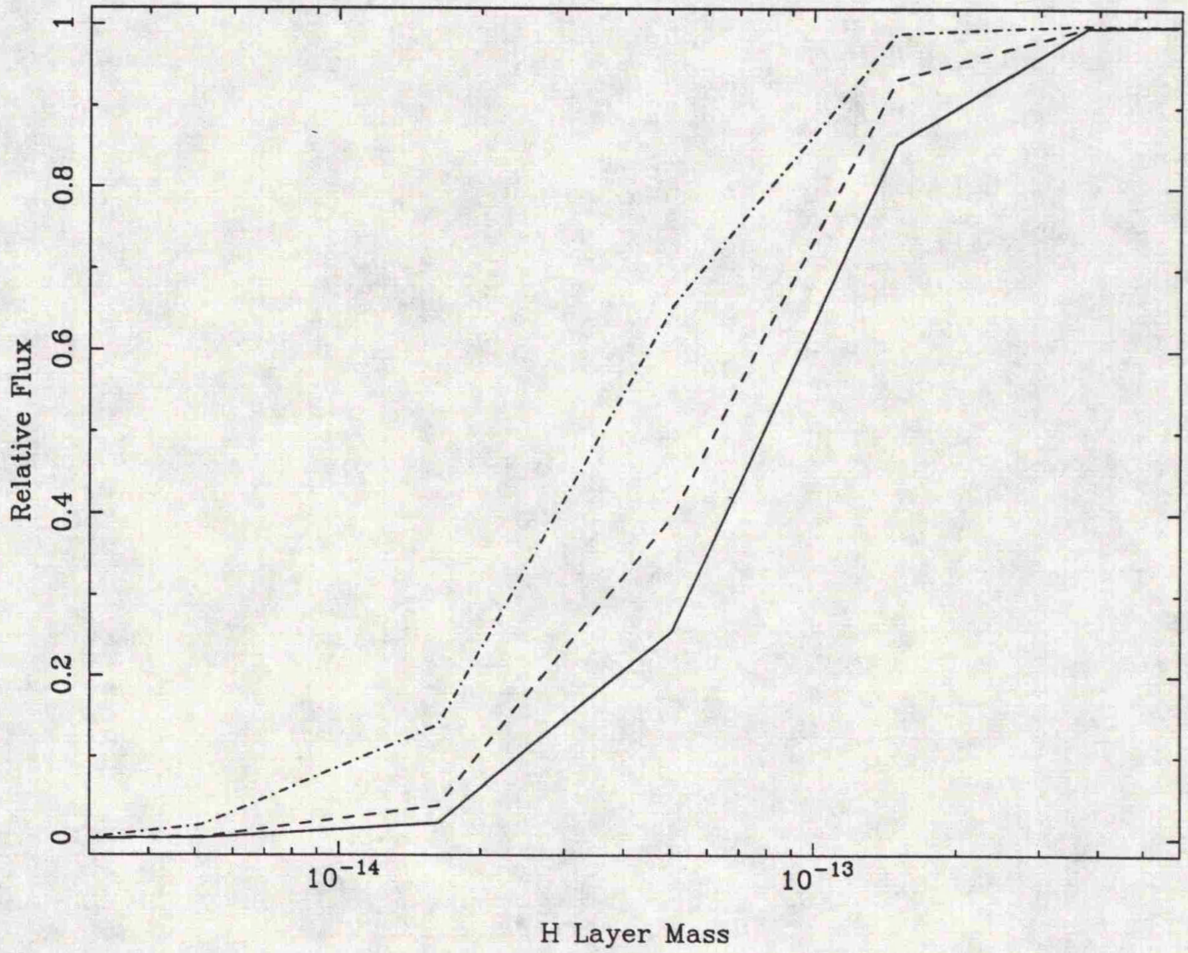

Figure 4.4: The effect of varying hydrogen layer mass in a stratified atmosphere on the EUV/X-ray fluxes. Predicted fluxes are for $T_{eff} = 30,000$K, log g = 8.0 and are normalised on the plot to those for a pure hydrogen atmosphere ($M_H = 6.5 \times 10^{-13}$). PSPC - solid line, S1a - dashed line, S2a - dash-dot line.

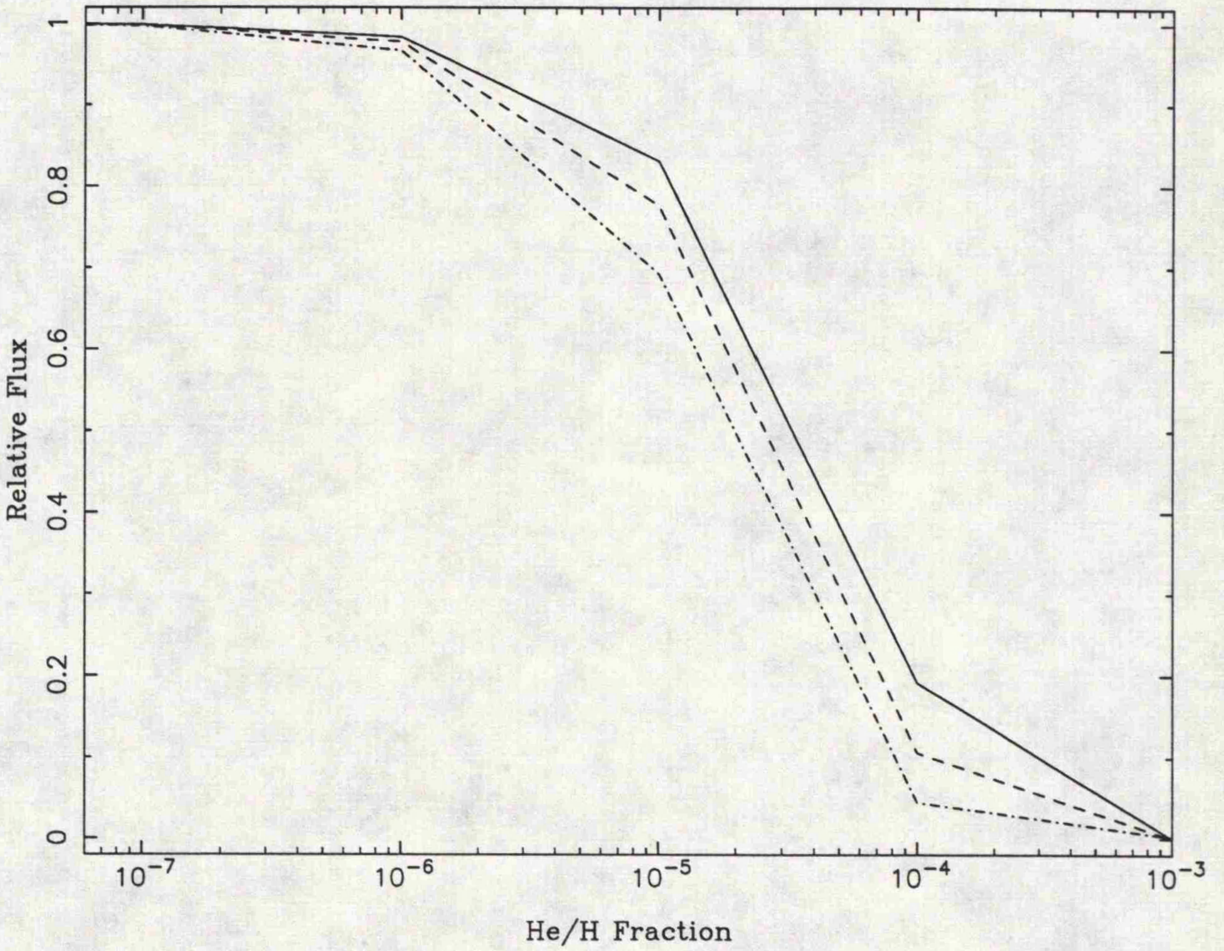

Figure 4.5: The effect of homogeneously mixed trace helium on the EUV/X-ray fluxes. Predicted fluxes are for T_{eff} = 30,000K, log g = 8.0 and are normalised on the plot to that for a pure hydrogen atmosphere (He/H = 10^{-8}). PSPC - solid line, S1a - dashed line, S2a - dash-dot line.

Of the atmospheric stellar parameters, the ROSAT fluxes depend only weakly on log g (which is accurately known) over the range of values covered here (figure 4.2), but all the remaining parameters have a large effect on the observed count rates. As mentioned above, the fluxes increase sharply from 20,000K to 30,000K with the gradient increasing toward the softer energy bands. Above this temperature (where the Lyman edge disappears due to a decline in the population of the ground state) they then increase quite uniformly up to 100,000K as shown in figure 4.3.

From figure 4.4 it can be seen that decreasing M_H has the largest effect in the highest energy band, because in the stratified model, helium is located at some depth in the atmosphere as defined by the diffusion boundary and decreases toward the surface. As photons with shorter wavelengths originate from deeper, hotter regions in the atmosphere, the higher energy photons will encounter a higher density of helium. In the homogeneous models however, where helium is located throughout the whole of the atmosphere the situation is different. Figure 4.5 shows how the presence of helium in this structure affects the lowest energy bands the most. This is due to the HeII absorption edge at 228 Å (just below the S2 band width) increasing with increasing helium abundance. The fact that the different structures affect the emergent fluxes in such different ways provides a way of distinguishing between them. However, the presence of heavy elements which have many absorption edges in the soft X-ray, can affect the flux in the shortest wavelengths the most giving a similar effect to that of stratification.

4.3 Model Fitting Technique

Model fits were performed with both homogeneous and stratified models using XSPEC. This compares predicted count rates, after folding model atmosphere spectra through each instrumental response and interstellar absorption, with observed values in each instrument and filter. Firstly, the V magnitude with its associated error was converted to a count rate and a gaussian response was calculated. This then provided a fourth data point together with the ROSAT S1a, S2a and PSPC survey count rates. Interstellar absorption from HI, HeI and HeII is taken into account using the model of Rumph, Bowyer & Vennes (1994) which includes HeI absorption cross-sections for a recently discovered series of resonance features near 206 Å. In all cases HI

Table 4.1: Probability of χ_r^2 exceeding the tabulated values

	Probability (Confidence Level)			
ν	0.32	0.1	0.01	0.001
	($68\% = 1\sigma$)	(90%)	(99%)	($99.9\% \approx 3\sigma$)
1	1.00	2.71	6.63	10.83
2	1.15	2.30	4.60	6.91
3	1.17	2.10	3.80	5.40
4	1.18	1.95	3.33	4.6

was left as a free parameter with HeI set to cosmic abundance (ie. one tenth that of HI) essentially freezing this parameter, and HeII was set to zero and frozen. The model atmospheres were then specified by log H/He (or log Pg_0 – see section 4.6), log g, T_{eff}, and a normalisation constant. The presence of the normalisation constant essentially being accounted for by the use of the V magnitude as a data point.

An initial fit to the data was performed with log g frozen at the best fit value (as log g has the least effect on the count rate) derived from the optical spectroscopy while all the other parameters except T_{eff} (which was stepped throughout its 1σ error range) were allowed to vary throughout the full range of the model spectra. Once a minimum was found, T_{eff} was frozen and log g was allowed to change through its 1σ error range. This process was repeated until the minimum χ^2 was found for both parameters, usually involving no more than two iterations of the above steps. T_{eff} and log g were then frozen at their best fit values giving one degree of freedom. Subsequent fits were then performed allowing only N_H and log Pg_0 (or log H/He) to vary. In this way the absolute minimum in χ_r^2 space was determined and hence the best fitting model spectrum to the data was found.

It is necessary in the analysis to define what is a good fit and what is not, by considering the probability that a particular value of χ_r^2 occurs by chance. A good fit corresponds to a probability of 0.1 (i.e. 90% confidence) and a bad fit a probability of 0.01 (99% confidence). In between, the fits are not necessarily bad, but it is not possible to exclude the models with high confidence. Table 4.1 lists the values of χ_r^2 corresponding to probabilities of 0.32, 0.1, 0.01, and 0.001 (confidence levels of $68\% = 1\sigma$, 90%, 99%, and $99.9\% \approx 3\sigma$) for several degrees of freedom (ν). Taking as an example a spectral analysis where $\nu = 1$ (as in this work), a 'good' fit requires χ_r^2 to be less than 2.71, but the value would need to exceed 6.63 before the model could be excluded with any certainty.

Once the best model fit to the data was achieved, the values of N_H and He/H (or log Pg_0) were independently stepped until $\Delta\chi^2 = 2.71$ providing $\chi_m^2 + \Delta\chi^2 < 6.63$ thus yielding upper and lower bounds of $\approx 1\sigma$ (see Appendix A).

4.4 Accuracy of Fitted Model Parameters

Several sources of error contribute to the accuracy of the parameters derived from any spectral fit to the data. Firstly, there are the errors on the data themselves. These are in the form of 1σ statistical counting errors on the observed survey count rates as listed in table 2.2. There are also systematic errors associated with the absolute photometric calibration of the instruments which must be taken into account, the largest factor being the uncertainty in the reference standards used. For the PSPC, S1a and S2a, the reference standards are proportional counters with a quantum efficiency which can be calculated theoretically, giving a 1σ error of 10%. This systematic error was added in quadrature to the statistical error for each data point during the analysis. The resultant error bars effectively 'weight' the data points when calculating the χ^2 statistic (see equ. A.2).

A more difficult error to assess is that of the synthetic spectra themselves. If the models do not accurately represent the correct compositions in the DA atmospheres then they will obviously not fit the observed data well. Even if all the opacity sources are included, it is still possible that an incomplete description of all the physical processes involved may give rise to a poor fit. However, this is very difficult to quantify but the fact that some stars may be fitted very well suggests that the models may be suitable. If not all the data can be fitted by the model then this implies that the model may be wrong in some aspect.

4.5 Results for Homogeneous Models

This section considers the results of the spectral fitting under the assumption that the white dwarf atmospheres are homogenous mixtures of hydrogen and helium. It is possible to divide the sample into two main groups, those for which a good fit is achieved (HGI: 60 stars) and those for which no fit is possible to the observed count rates (HGII: 29 stars). The 'best fit' values of N_H and helium fraction for the stars in HGI are listed in table 4.2 and the stars in HGII are listed in table 4.4. Of the stars which could be succesfully modelled, the sample can be further divided into two subgroups (HGIa and HGIb). This is best illustrated in figure 4.6 which shows the allowed ranges of He/H fraction against their optically derived temperatures for HGI. For clarity only the best fit values of T_{eff} are shown.

HGIa:

It can be seen that the fluxes of all the stars in this subgroup (47 in all) may be accounted for by a pure hydrogen atmosphere. He abundances are in the range $\approx 0 - 4 \times 10^{-4}$, with two objects having $\approx 0 - 3 \times 10^{-3}$ by number fraction (10^{-8} is the lower limit of the model atmosphere grid and effectively 0). In reality, as helium may not be the only opacity source, only an upper limit of $\approx 4 \times 10^{-4}$ may be placed on these abundances, but it should be noted that all these objects are consistent with a pure hydrogen atmosphere. Only two of the stars, RE0350+17 and RE0605-48 have a lower limit above 10^{-8}, specifically 6.1×10^{-6} and 2.2×10^{-6} respectively, but such number fractions are still extremely low. Most these stars (33) in this group have temperatures below 40,000K but it should be noted that 14 lie above this temperature. This is in contrast to the work by B93 and Diamond (1993) who found that no stars above 40,000K (except for HZ43) had count rates which could be modelled by a pure hydrogen atmosphere.

HGIb:

The stars in this subgroup (13 objects) all have a He/H fraction greater than $\approx 3 \times 10^{-4}$ and are distinct in figure 4.6 in displaying a relatively small confidence range. In agreement with the previous work all these stars lie above $\approx$ 40,000K (only one, RE1614-08 lies below, with an upper limit to T_{eff} of 38,890K). Two of these stars, RE2013+40 and RE1016-05 are DAOs (the third known DAO, RE0720-31 produced no fit) showing HeII absorption at 4686 Å (Barstow *et al.* 1995a and Tweedy *et al.* 1993 respectively). However, although there is no doubt that significant quantities of helium are present in these stars, the abundances given here for RE2013+40 appear

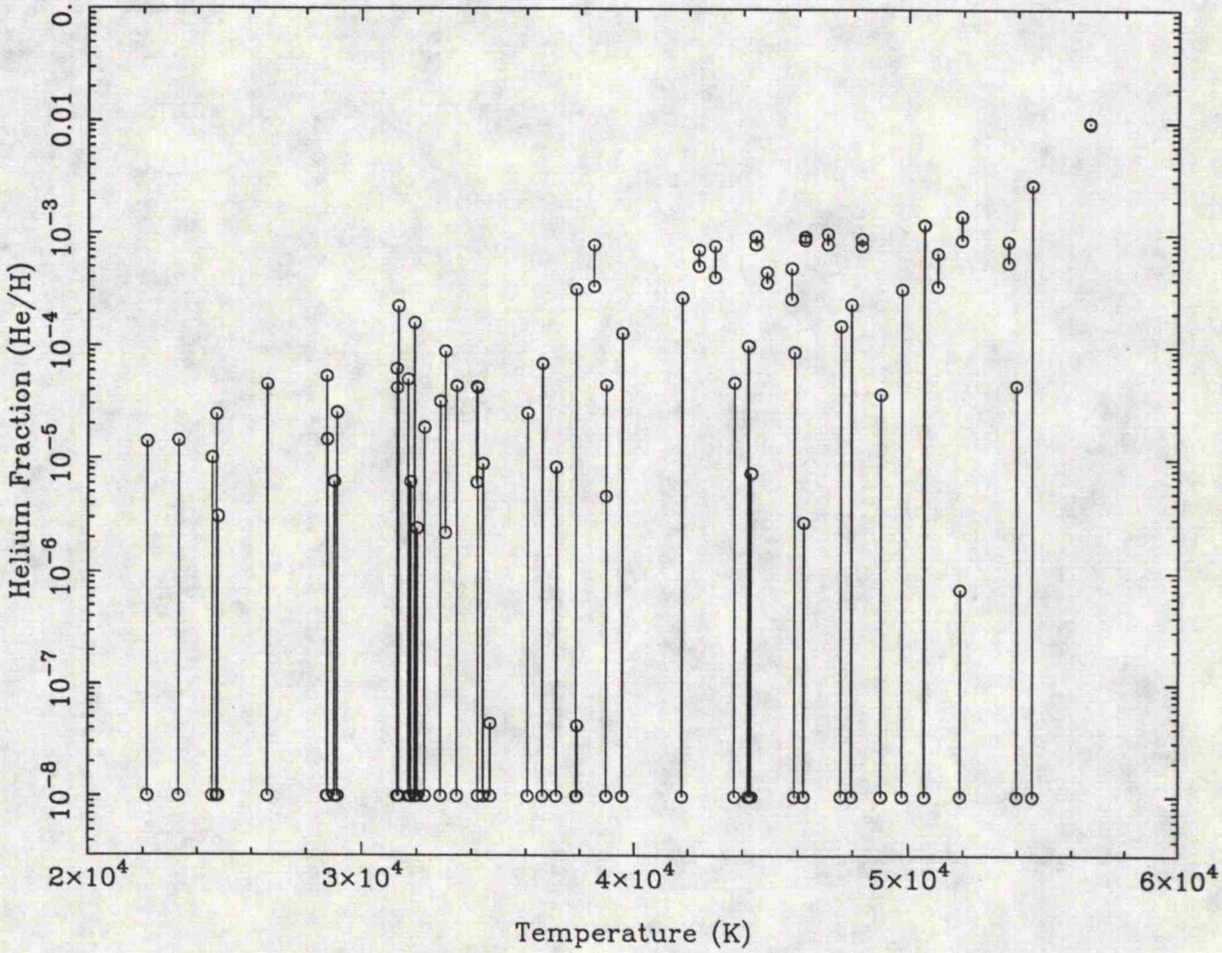

Figure 4.6: The 1σ range in helium abundance allowed by the ROSAT data for those white dwarfs for which good fits to homogeneous H + He models were obtained as a function of temperature. The range in He/H fraction was found within the optically determined temperature bounds but only the best fit value of T_{eff} is shown for clarity.

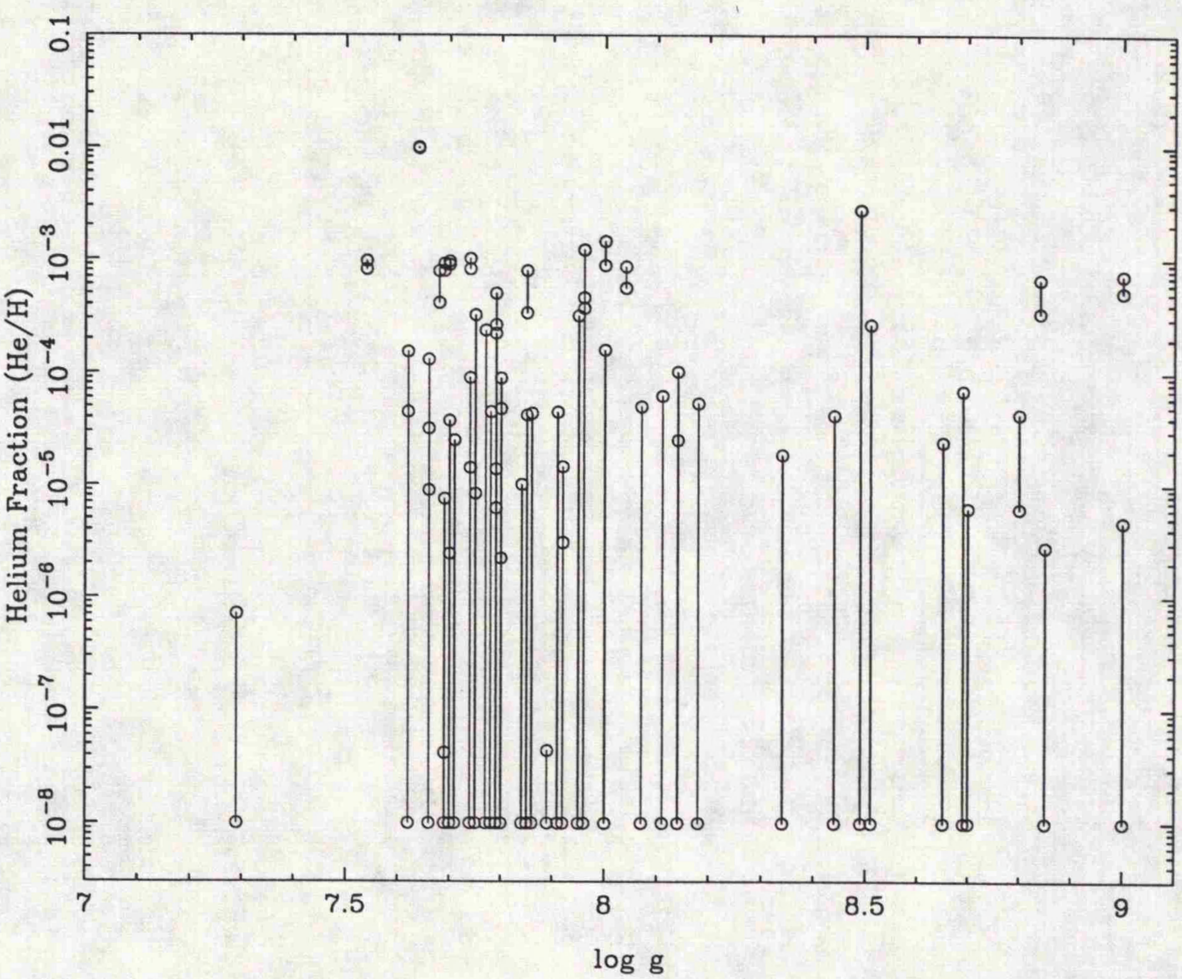

Figure 4.7: The 1σ range in helium abundance allowed by the ROSAT data for those white dwarfs for which good fits to homogeneous H + He models were obtained as a function of surface gravity. The range in He/H fraction was found within the optically determined bounds of log g but for clarity only the best fit value is shown.

to be in disagreement with those derived from fitting the HeII (4686Å) absorption line. This is discussed further in section 4.7. For the remainder of the stars in this subgroup only lower limits can be placed on the helium abundances of $\approx 3 \times 10^{-4}$, if we assume that helium is the only source of opacity present. Such abundances would only produce weak HeII optical absorption which would be lost in the signal to noise. However, the helium abundance of RE2334-47 which is the highest in figure 4.6 (at 9.89×10^{-3}) would give rise to strong HeII absorption and this is not observed in the optical spectrum (see figure 4.11). A possible explanation of this could be stratification. However, it is possible that several, if not all of these objects (except the DAOs) have little helium but that small amounts of trace heavier elements affect the fluxes in a way similar to that of helium. If this is the case, it can only be quoted that these objects contain at most a helium abundance of $\approx 10^{-3}$ (with RE2334-47 having 10^{-2}, which is the model grid upper limit), but the possibility of the opacity arising from heavier elements rules out further interpretation.

This possibility is compounded by the fact that the 29 objects in HGII cannot be represented by any H + He model atmosphere. Many of these objects have been observed in various wavebands showing numerous lines due to heavier trace elements but no sign of helium (Barstow, Holberg & Koester 1994). Irrespective of the absorbing material (be it helium or heavier elements) there seems to be no correlation between the resultant inferred helium abundance from these models and temperature apart from the confirmation of previous work that the absorbing material only becomes evident above $\approx 40,000$K.

HGII:

Interestingly, only 16 of the 29 HGII stars lie above 40,000K (see table 4.4), with 9 objects being cooler than 30,000K. In the B93 work it was suggested that not being able to model stars cooler than 30,000K was due to the lack of line blanketing in their models giving rise to ambiguities below 30,000K. However, the models used here are fully line blanketed and so it is difficult to account for these objects not being consistent with a pure hydrogen composition.

Figure 4.7 shows the values of He/H fraction as a function of surface gravity for the stars for which a good fit is possible. As might be expected, when considering radiation levitating elements against surface gravity, the stars which are not consistent with pure hydrogen (HGIb), have some of the lowest surface gravities. However, it should be noted that many stars which may be explained as pure hydrogen also have surface gravities in this range (as well as high temperatures, $T_{eff} > 40,000$K) implying the actual photospheric composition may vary significantly from star to star. Surprisingly, two of the 'non-pure H' stars, RE1746-70 and RE0348-00 have some of the highest surface gravities in the sample at 8.84 and 9.0 respectively. Vennes *et al.* (1988) have shown that in such a regime, even at the high temperatures of these stars, the amount of helium that may be supported in the photosphere purely as a result of radiative levitation is approximately an order of magnitude less than that inferred here. The abundance derived here could represent the effect of heavier elements or could be the result of a physical process such as convection causing the helium to rise in the atmosphere. Such high gravities at the given temperatures for these stars deviate from the normal DA evolution model as will be discussed later. To conclude, there appears to be no correlation between surface gravity and helium abundance apart from the fact that the observed He abundances occur on the whole in the lowest gravity objects.

4.6 Results for Stratified Models

This section summarises the spectral fitting results assuming a stratified structure, with a thin layer of hydrogen overlying a helium atmosphere. The mass of the hydrogen layer M_H, for a given temperature and gravity dictates whether the observed EUV/X-ray photons originate from a region of pure hydrogen or a region polluted by the helium diffusion tail, giving rise to opacity from helium. The parameter which effectively defines the level of opacity in the stratified model is Pg_0, the gas pressure at the optical depth where the partial pressures of the hydrogen layer and the helium layer are equal, defining the diffusion boundary (see Jordan & Koester 1986, for further details). It may be represented by the equation,

$$Pg_0 = \alpha \frac{GM_* 4\pi R_*^4}{M_H} \tag{4.1}$$

where α is a normalisation constant and the other symbols have their usual meanings. A log $Pg_0 \approx 9.0 - 10.0$ is sufficiently high that the radiation emitted below the diffusion boundary is completely absorbed by the atmosphere above and results in a spectrum identical to that of a pure hydrogen envelope. However, from the above equation it is evident that M_H is also heavily dependent on surface gravity. For a high gravity star, the atmospheric pressure and hence the mean density of the atmosphere is higher than that for a low gravity object. Therefore, the EUV/X-ray photons may actually be absorbed by a physically lower mass of H. M_H is also dependent on T_{eff} but only very weakly. The actual variation of M_H with log g (for constant T_{eff} and log Pg_o) and log Pg_o (for constant log g and T_{eff}) are shown in figure 4.8.

Similar to the homogeneous régime, it is possible to divide the results into two groups, although not necessarily containing all the same objects as the corresponding homogeneous groups. Those which may be modelled well (SGI: 71 stars) are listed in table 4.3 and those which cannot be represented by any combination of N_H or M_H (SGII: 18 stars) are listed in table 4.4. Figure 4.9 shows the range in M_H allowed in the spectral fitting as a function of T_{eff} for SGI. Due to the dependence of M_H on surface gravity, for clarity objects with log g greater than 8.0 are shown as open circles whereas those below this value are filled circles. These stars may then be divided into two subgroups SGIa and SGIb.

SGIa:

Although the spread in M_H is large, all the objects in this subgroup (45 stars) are in fact consistent with approximately pure hydrogen atmospheres but for differing surface gravities. It is therefore difficult to place limits on the layer masses but it is possible to say that below 50,000K, objects with log g < 8.0 have a lower limit of $\geq 3 \times 10^{-14}\,M_\odot$ with the majority having $M_H \geq 10^{-13}\,M_\odot$ which is sufficiently massive that the EUV/X-ray photons, which are from deeper layers, are originating from a region of pure hydrogen. It is somewhat easier to identify these stars as being consistent with pure hydrogen if M_H is plotted as a function of surface gravity (figure 4.10). The dashed lines correspond to layer masses approximately equivalent to a pure hydrogen atmosphere (log $Pg_0 = 9.0 - 10.0$) for a constant temperature. Although only values of M_H are given, an upper limit (and often a best fit value) of log $Pg_0 = 10.0$ was found for the majority of these stars corresponding to a pure hydrogen spectrum and this gives the expected general trend for decreasing layer mass with increasing log g. As in the homogeneous case, of the order of 10 objects which may be modelled as pure hydrogen have temperatures in excess of 40,000K.

SGIb:

The count rates for the 26 objects in this subgroup may be explained by layer masses thin

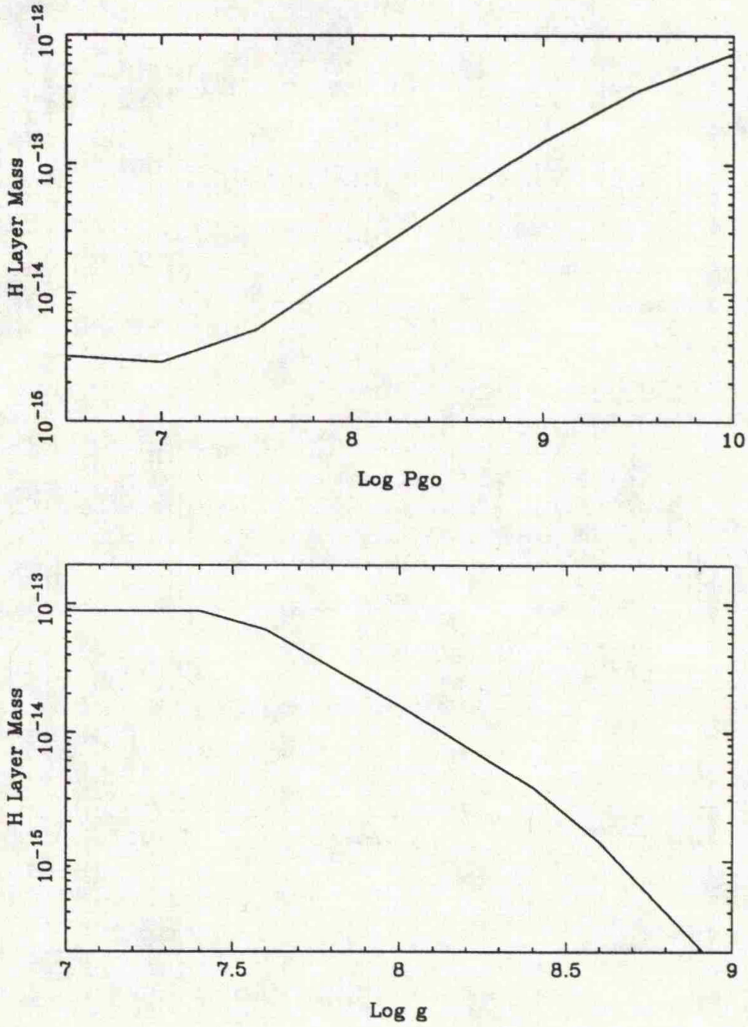

Figure 4.8: The dependence of hydrogen layer mass (M_H) on $\log Pg_0$ (the log of the gas pressure at the H:He diffusion boundary) for $T_{eff} = 30,000$K, log g = 8.0 (top) and surface gravity for $T_{eff} = 30,000$K, $\log Pg_0 = 8.0$ (bottom). The dependence of M_H on T_{eff} is very weak.

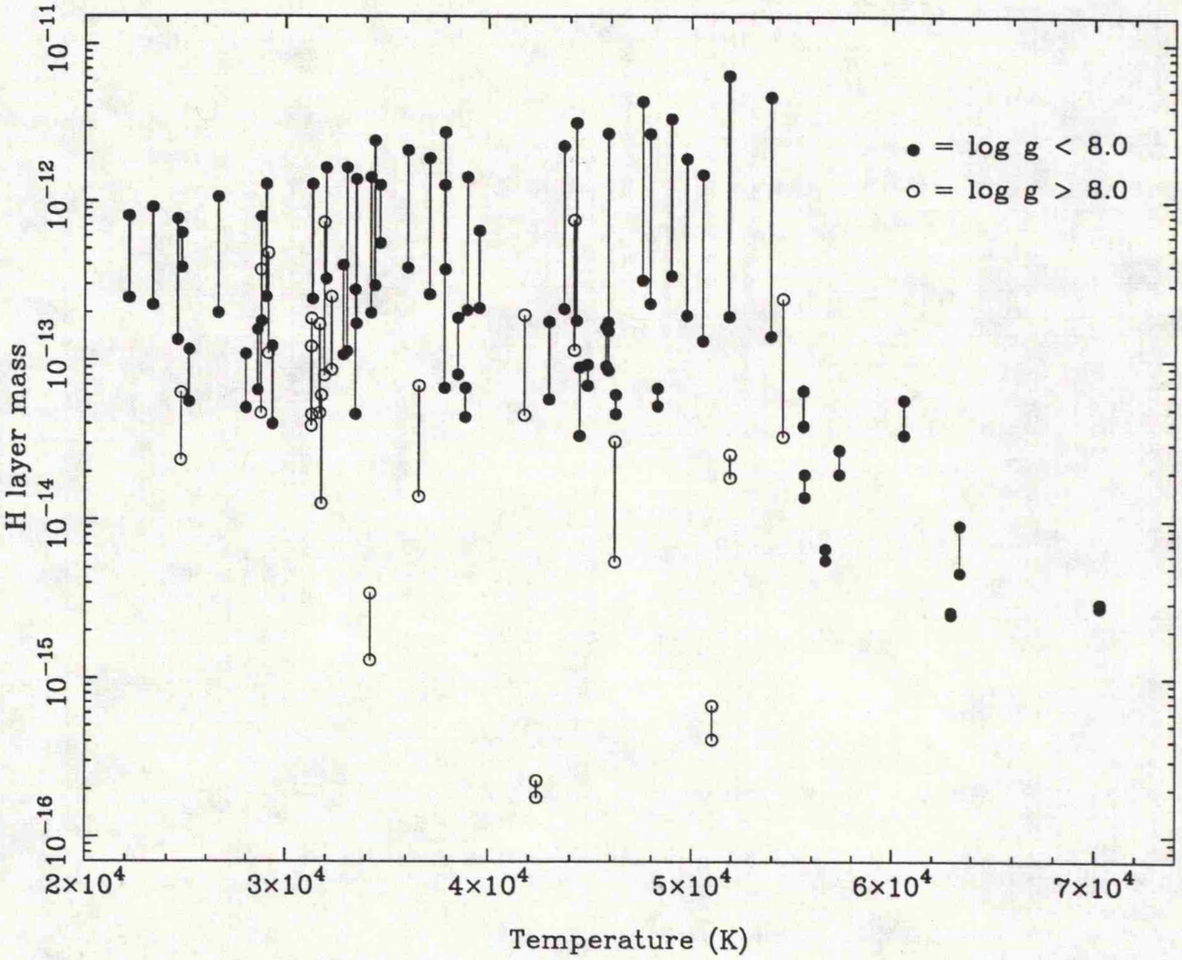

Figure 4.9: The 1σ range in M_H allowed by the ROSAT data for those white dwarfs for which good fits to stratified H + He models were obtained as a function of temperature. The range in M_H was found within the optically determined temperature bounds but only the best fit T_{eff} is shown for clarity.

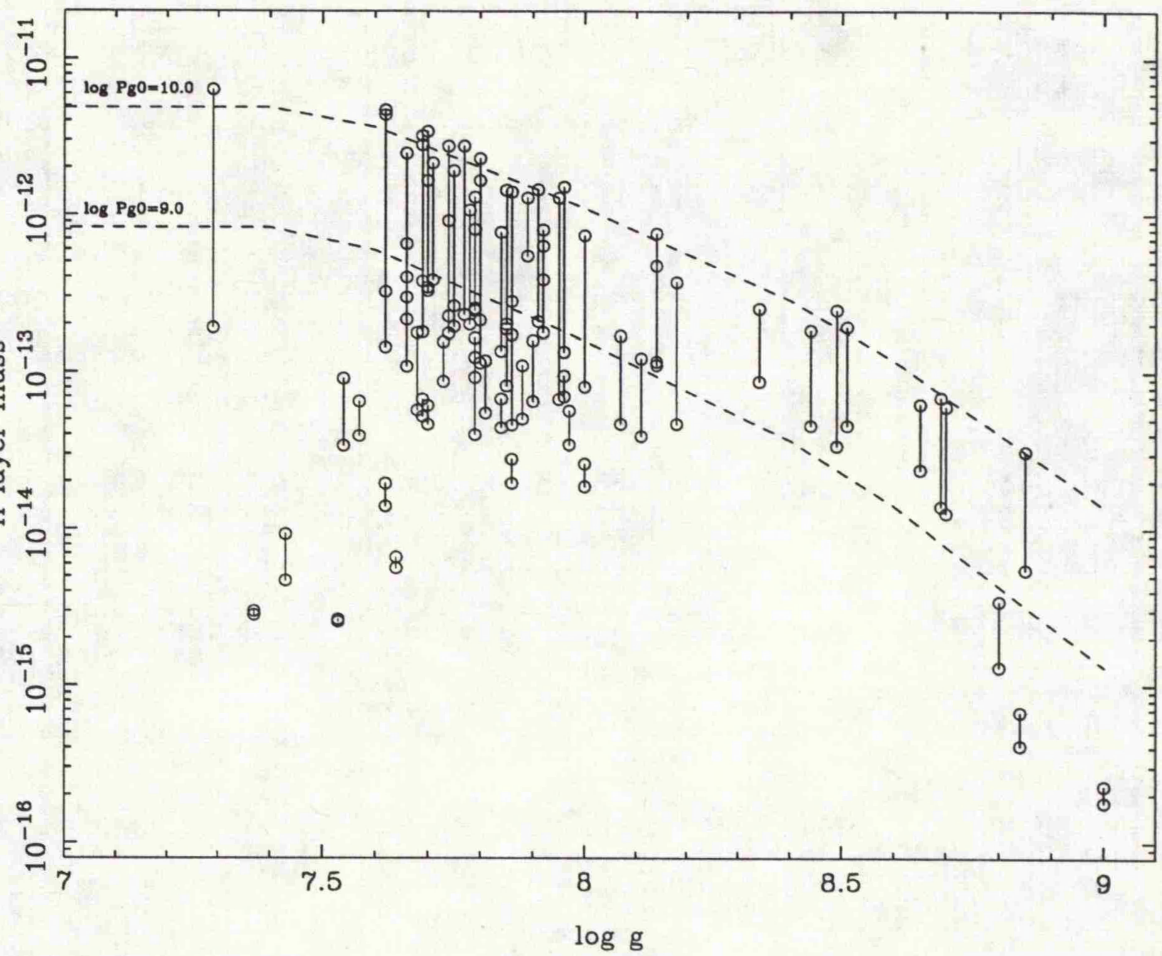

Figure 4.10: The 1σ range in M_H allowed by the ROSAT data for those white dwarfs for which good fits to stratified H + He models were obtained as a function of log surface gravity. The range in M_H was found within the optically determined log g bounds but only the best fit log g is shown for clarity. The dashed lines enclose the approximate region where an atmosphere is pure hydrogen (log $Pg_0 = 9.0 - 10.0$).

enough for the EUV/X-ray radiation to come from a helium contaminated region below the hydrogen layer. This is immediately evident from figure 4.10 where these stars, contrary to the pure hydrogen relation of gravity with M_H, show increasingly lower layer masses with decreasing surface gravity. However, it should be noted that the lowest gravity object RE0550-24 appears to be pure hydrogen with a large hydrogen layer mass greater than 1.9×10^{-13}. This object is also consistent with pure hydrogen in the homogeneous regime. Figure 4.9 also shows a tendency for decreasing layer mass with increasing T_{eff} (for log g < 8.0) above 50,000K. This is most probably due to the evolutionary relation between temperature and gravity, although it is possible that some of these low gravity objects may have evolved from hot subdwarfs on the extended horizontal branch. The highest gravity objects also have extremely thin hydrogen layers (eg. RE0348-00 with log g $= 9.0$ having $M_H = 2.0 \times 10^{-16}\ M_\odot$ at the model boundary) which could possibly be the result of the abnormal evolution already suggested.

It is interesting to note that RE2334-47 which had the highest He/H fraction in the homogeneous fitting no longer seems unique when assuming a stratified structure. With the layer mass of $7.3 \times 10^{-14}\ M_\odot$ derived here, the predicted HeII line at 4686Å disappears due to the different structure. Figure 4.11 shows the spectrum of RE2334-47 together with the spectrum predicted by the homogeneous model (with the best fit helium abundance to the ROSAT data) and that predicted by the stratified model (with the best fit hydrogen layer mass). A stratified atmosphere with a moderate hydrogen layer mass is, therefore, a plausible explanation for this star. However, the possibility that heavier elements are present in the photosphere, which have the same net effect as stratification, can not be ruled out until an extensive examination of an EUVE spectrum has been performed. As later discussion will show (see figure 4.14), RE2334-47 appears very similar to several objects which are known to contain a host of heavy elements.

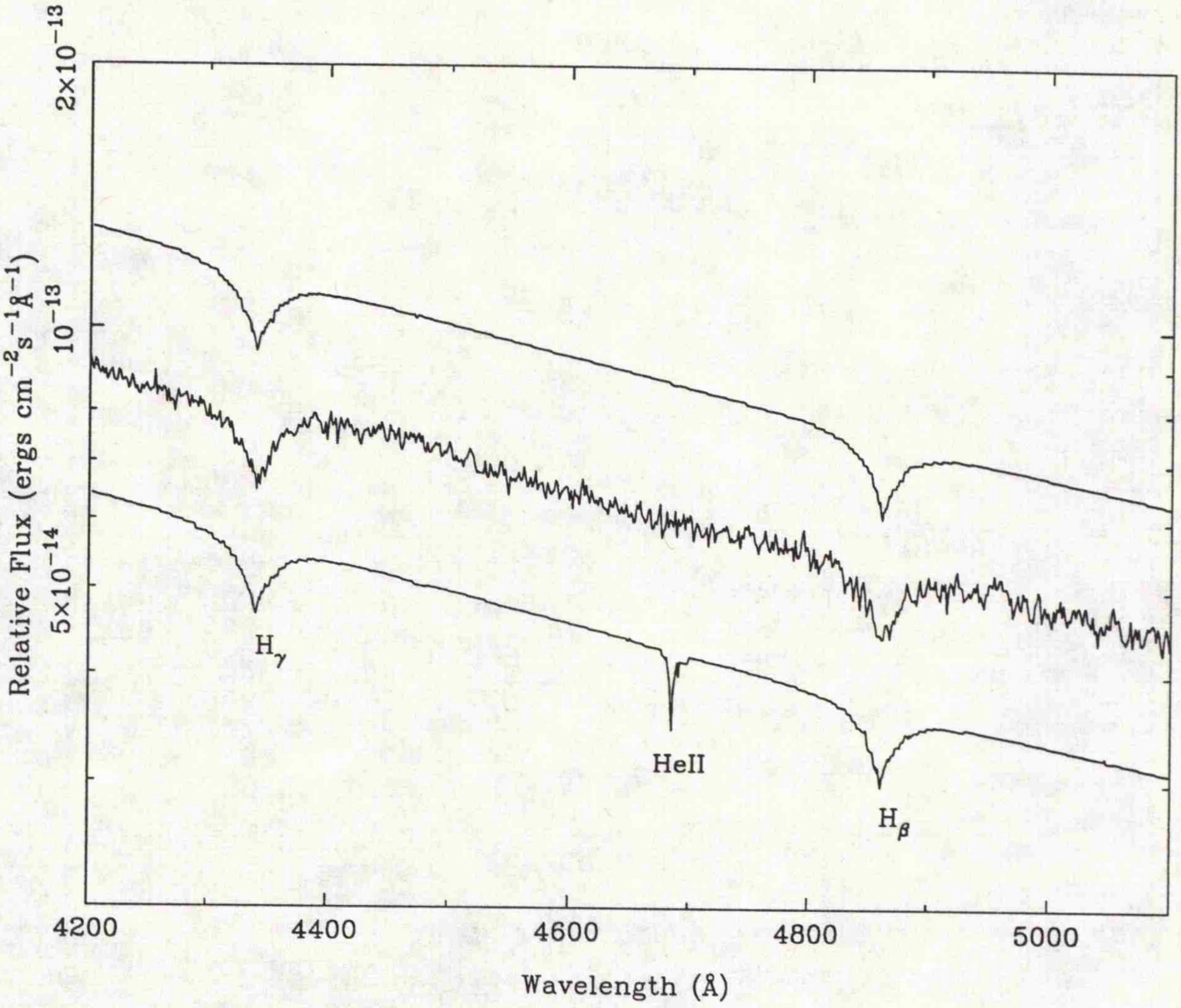

Figure 4.11: Part of the optical spectrum of RE2334-47 (centre). The top curve is the spectrum predicted by a stratified model with $M_H = 7.3 \times 10^{-14}$ $M_\odot$, $T_{eff} = 55,082$K and log g = 7.61 (ie. the best fit parameters from the EUV/X-ray data). The bottom curve is the corresponding spectrum predicted by a homogeneous model with He/H = 9.9×10^{-3}, $T_{eff} = 54,884$K and log g = 7.63. The HeII 4686 Å line predicted by the homogeneous model is clearly not evident in the spectrum.

SGII

Of the 18 stars which could not be modelled by a stratified atmosphere, only three, RE0138+25 and the DAOs RE2013+40 and RE1016-05 may succesfully be modelled by a homogeneous structure (see table 4.4). As in the homogeneous case, several of these objects, 8 to be exact, have temperatures less than 40,000K (with 5 below 30,000K) which is difficult to explain as one would not expect significant amounts of trace elements at these temperatures.

The stratified H + He model structure may be a suitable description for the majority of stars but the fact that many stars cannot be fit by any combination of N_H and M_H and that several stars have been observed to contain many trace heavier elements means we can only put lower limits on M_H. Much of the absorption may arise from elements heavier than helium being 'levitated' by radiation pressure against the force of gravity into the helium diffusion tail reducing the EUV/X-ray flux giving rise to an apparently thin layer mass. If this is the case then figure 4.9 would imply that, apart from a few objects, one or more heavy elements are levitated above 50,000K.

4.7 The DAO stars

As the DAO stars display a HeII absorption feature in the optical band, this has to be taken into account in the interpretaion of the model fitting. It has been found that all three of the DAOs in this sample are also members of binary systems with an M-dwarf in close proximity. The presence of the companion creates problems in measuring the V magnitude as well as T_{eff} and log g. Also, any EUV/X-ray emission from the secondary must be subtracted from the ROSAT photometry in order to isolate the white dwarf count rate. Details of the approach taken for RE2013+40, RE0720-31 and RE1016-05 may be found in Barstow *et al.* (1995a), Barstow *et al.* (1995b) and Tweedy *et al.* (1993) respectively, but will be briefly summarised here together with the results of the new analysis.

RE2013+40:

As the V magnitude for RE2013+40 has a large error and an IUE UV spectrum exists, the 1400Å flux (1.5×10^{-12} ergs cm^{-2} s^{-1} Å^{-1}) was used to normalise the model spectra. Three individual optical spectra were obtained and all were analysed independently as co-adding them carried the risk of artificially broadening the Balmer lines by orbital motion. In measuring the temperature and gravity for these stars one cannot assume a pure hydrogen model due to the presence of the HeII feature. The Balmer lines and the HeII line were fit simultaneosly, using both homogeneous and stratified model atmospheres allowing the He/H fraction or M_H respectively to vary along with T_{eff} and log g. With the stratified model the best fit to the HeII line corresponds to the thinnest hydrogen layer in the grid ($10^{-15}M_{\odot}$) for the derived temperature and gravity. Since the ROSAT fluxes predicted by this model are far below the instrument sensitivity, it is possible to rule out a stratified structure. Stratification was also ruled out by Bergeron *et al.* (1994) on the basis of a poor fit to the HeII line.

Homogenous models provided good fits to all three spectra. However, it was observed that emission cores in the Balmer absorption lines, associated with the red dwarf companion, differed in strength from one observation to another due to changing orbital phase. This resulted in different estimates of surface gravity and inferred helium abundance (the temperatures were in good agreement for all three spectra). Correspondingly, there was a variation in the equivalent width of the HeII line indicating the change in the inferred amount of helium is real rather than simply a result of the different estimates of log g. These changes do not necessarily arise from intrinsic variation in the photospheric content, but may be a result of infilling of the helium absorption feature by an emission line associated with the red dwarf. The spectrum obtained on 1^{st} July 1992, displayed the least core emission in the Balmer lines and the correspondingly largest HeII equivalent width and yielded a He/H fraction of 1.9×10^{-3} with bounds of $(1.3 - 2.9) \times 10^{-3}$.

When modelling the ROSAT data, any coronal X-ray flux arising from the M dwarf must be removed. In the PSPC, flux from even the hottest white dwarfs lies longward of the carbon K edge and so the detection of 0.038 ± 0.010 count s^{-1} shortward of this is attributed to the M dwarf. Fleming *et al.* (1995) find that typical dMe count ratios in the soft to hard PSPC bands is 2:1. The PSPC count rate for the primary is therefore adjusted to be 0.86 count s^{-1} and is treated as a lower limit. It was not possible to model the data with a helium abundance in the range found from the HeII line. However, a good fit was achieved as listed in table 4.2 with a range in He/H of $(3.9 - 7.4) \times 10^{-4}$, significantly lower than that derived from the optical data. It should be noted that several metal features (notably CIV) have been observed in the

IUE spectrum. Further sources of opacity such as this should give a higher helium abundance than that observed in the optical spectra. It has been suggested by (Barstow *et al.* 1995a) that the relative lack of helium in the EUV forming region to that of the optical may be a result of accretion onto the white dwarf surface of the red dwarf stellar wind resulting in more helium higher in the atmosphere.

RE0720-38:

Barstow *et al.* (1995b) derived a value of V = 14.87 from the optical light curve after subtraction of the secondary star. As there was no detection above the carbon edge of the PSPC they concluded that any EUV/X-ray flux originating from the companion is insignificant. Several independent optical spectra were obtained but the HeII line was only visible after co-addition of the two with highest s/n. They find that values of T_{eff} and log g estimated from each spectrum agree well and that the observed radial velocity changes present in the co-added spectrum are not large enough to significantly affect the model fits to the Balmer lines and so all work referenced here is based on this spectrum. Using a stratified structure to model the HeII line gives a layer mass at the lower grid boundary which would render the EUV/X-ray fluxes undetectable to ROSAT. Therefore, one may rule out a stratified structure for this object also. Assuming a homogeneous structure, no fit to the ROSAT data is possible in any temperature range implying the presence of significant amounts of elements heavier than helium.

RE1016-05:

Thorstensen, Vennes & Bowyer (1995) have obtained the most accurate photometry to date of the DAO primary in this system. After subtraction of the red dwarf companion and the flux from a nearby star they find V= 14.21 ± 0.05 which is the value quoted in table 3.4 and used in the model fitting. There is no hard detection in the PSPC so it can be assumed that the flux below the carbon edge is entirely due to the white dwarf. Two spectra were obtained for this star at the Steward Observatory. In the second spectra, obtained on the 24$^{\rm th}$ April 1992, the broad emission cores of the Balmer lines due to the secondary star have virtually dissappeared. Hence, in a similar manner to Tweedy *et al.* (1993), only this spectrum was used for measuring T_{eff}, log g and He/H fraction. Slight emission cores were evident in the H_β and H_γ features and these were removed during the fitting to ensure no contamination by the secondary. All the Balmer lines were fit simultaneously together with the HeII line, first with stratified and then homogeneous models. The stratified fit gave a layer mass at the lower grid boundary which would render the

PSPC count rate a factor four less than the observed rate, thus ruling out a stratified atmosphere. The homogeneous models yielded best fit parameters of, $T_{eff} = 53,827\,\mathrm{K}\,(52,629 - 55,931)$, log g $= 8.08\,(7.98 - 8.17)$ and He/H $= 1.3 \times 10^{-3}\,(3.3 \times 10^{-4} - 2.1 \times 10^{-3})$. Comparing these results to those of Tweedy *et al.* (1993) and Bergeron *et al.* (1994) reveals a slightly lower temperature, higher gravity but similar helium abundance (although the best fit value derived here is somewhat higher, the error ranges show significant overlap). From table 4.1 it can be seen that this helium abundance also agrees well with the value inferred from the ROSAT data. However, Thorstensen, Vennes & Bowyer (1995) have determined an abundance of He/H $= 2 \times 10^{-3}$ from a strong HeII (1640 Å) absorption feature in the IUE spectrum of this object. Unfortunately, no confidence region is given to enable a fair comparison.

4.8 Comparison of Absolute Fluxes

It is clear from the above results that for the hottest DAs there are opacity sources additional to helium present in the atmospheres. Having established the relative inadequacy of the model atmospheres it is then impossible to say for certain whether the absorption arises from helium alone for the remainder of the sample, for which a model fit is achieved, or whether an overestimate of the amount of helium (or underestimate of M_H) is accounting for EUV/X-ray absorption from heavier elements. One can only quote limits for the helium abundance (or M_H) and note that an atmosphere containing only hydrogen and helium in these quantities is a possible explanation for these objects. Further interpretation is restricted by the absence of suitable models containing the trace absorbers.

Although we now have instruments such as the EUVE spectrometers which can actually identify the heavier trace photospheric species directly, most objects are too faint to be observed with realistic exposure times. Broad band EUV/X-ray photometry of the kind provided by ROSAT is limited in the detail we can obtain about the precise nature of the trace elements, but it is possible to investigate the overall pattern of photospheric opacity throughout the hot DA temperature range independantly of the model atmospheres. Any dependence of the opacity with parameters such as temperature and gravity, together with theoretical calculations can then reveal the probable nature of the absorbers.

In order to use such a model independent approach, estimates are required of the absolute fluxes from the observed count rates in each band for each star. Important information may also be present in the downward slope of the EUV fluxes toward higher photon energies. However, this is obscured by the disparate effective areas of each instrument and filter combination (see figure 2.4). An estimate of the EUV/X-ray flux in each band can be made by dividing the observed count rate by some nominal effective area A_{eff}, at the mean energy E of the instrumental bandpass. Since white dwarf spectra decrease steeply throughout the energy range of each filter, the values of A_{eff} and E must be dependent on the spectral shape to some extent. However, this approach does provide a good first order estimate of the incident flux. The values of $A_{eff}\,(\mathrm{cm}^2)$ and $E\,(\mathrm{keV})$ used are 7 and 0.085 (S2a), 8 and 0.14 (S1a), 190 and 0.2 (PSPC) respectively. As discussed in the previous chapter, the V magnitude is a useful normalisation point, accounting for stellar distance and radius and is accurately known. It therefore provides an estimate of the emergent EUV/X-ray fluxes from each star as a function of energy, thus allowing the count rates to be placed on a common scale and comparisons made. This procedure is summarised by the equation,

$$F = \frac{\alpha}{10^{-0.4V}} \times \frac{C_{obs}}{EA_{eff}} \tag{4.2}$$

where F is the relative emergent flux, α is a normalisation constant and C_{obs} is the observed count rate in *count* s^{-1}. As only the relative fluxes from star to star are of interest, for ease of handling the value of the normalisation constant in the above equation was chosen so that the V magnitude correction factor is 1 for V = 11.0, giving $\alpha = 4 \times 10^{-5}$.

Figure 4.12 shows the ratios of the S2:PSPC and S1:PSPC fluxes. The solid lines represent the ratios for a pure hydrogen atmosphere (normalised on the plot to HZ43) with a modest interstellar column of $5.0 \times 10^{18}\ \mathrm{cm}^{-2}$, generated from the stratified model grid. This plot reflects the spectral slope across the three bandpasses. Interstellar absorption from HI affects the softest S2 band the most and so tends to flatten the spectrum whereas photospheric opacity affects the hardest PSPC band the most acting to steepen it. This results in stars with high levels of opacity in their photospheres having increased ratios above the pure hydrogen line whereas stars with very high interstellar columns have reduced ratios. These effects can be seen with many stars below $\approx 50,000$K having reduced ratios while above $\approx 50,000$K the ratios increase dramatically. With a very high N_H one begins to lose information about the star and it becomes difficult to distinguish photospheric from interstellar absorption. For this reason, 19 stars (indicated by filled circles for the S2:PSPC) which have obviously very high columns were omitted during further study.

One limitation in the interpretation of figure 4.12 is that a high column together with high intrinsic absorption can give a false pure hydrogen shaped spectrum. In order to see what is happening more clearly one must look at the individual fluxes which are shown in figure 4.13. Again, the solid lines represent the pure hydrogen star with modest column normalised to HZ43. This confirms the results of B93. Looking first at those stars less than 40,000K it can be seen that most have fluxes close to those predicted for a pure hydrogen atmosphere with a modest column. In most cases, as can be seen from tables 4.2 and 4.3, the small scatter around the pure hydrogen lines is due to varying amounts of interstellar column. The PSPC points are quite evenly distributed around the pure hydrogen prediction as they are least affected by N_H.

In a few cases such as RE0831-53 at 29,330K larger flux decrements are observed indicating some form of opacity is present. For this object, increasing departures from pure hydrogen with increasing band energy indicates possible photospheric absorption. From figure 4.12, the flux ratios also indicate some form of photospheric opacity. Conversely, RE1650+40 at 37,850K shows a large flux deficit in all bands but this decreases with increasing energy. Figure 4.12 indicates that a high column may be responsible for much of the opacity for this source. It is clear that in order to understand each individual object one must use the combined information from figures 4.12 and 4.13. However, with such a large sample it may be said that most of the stars below 40,000K are essentially pure hydrogen.

The increased sample size provides much more detail, particularly in the 40,000 - 50,000K range which was sparsely populated in the B93 work. In this region the majority of objects show flux decrements in all energy bands, indicating some photospheric opacity source is present. However, several objects other than HZ43, specifically RE0632-05, RE1032+53, RE1043+49, RE2009-60 and RE2156-54 appear consistent with a pure hydrogen atmosphere with the PSPC fluxes lying very close to the pure hydrogen line but the S1 fluxes showing a decrement and the S2 fluxes more so indicating relatively high columns. Figure 4.12 suggests that *all* the stars in this region are consistent with pure hydrogen but for the higher temperature stars, large flux decrements in all wavebands implies that there is signficant photospheric opacity in these objects.

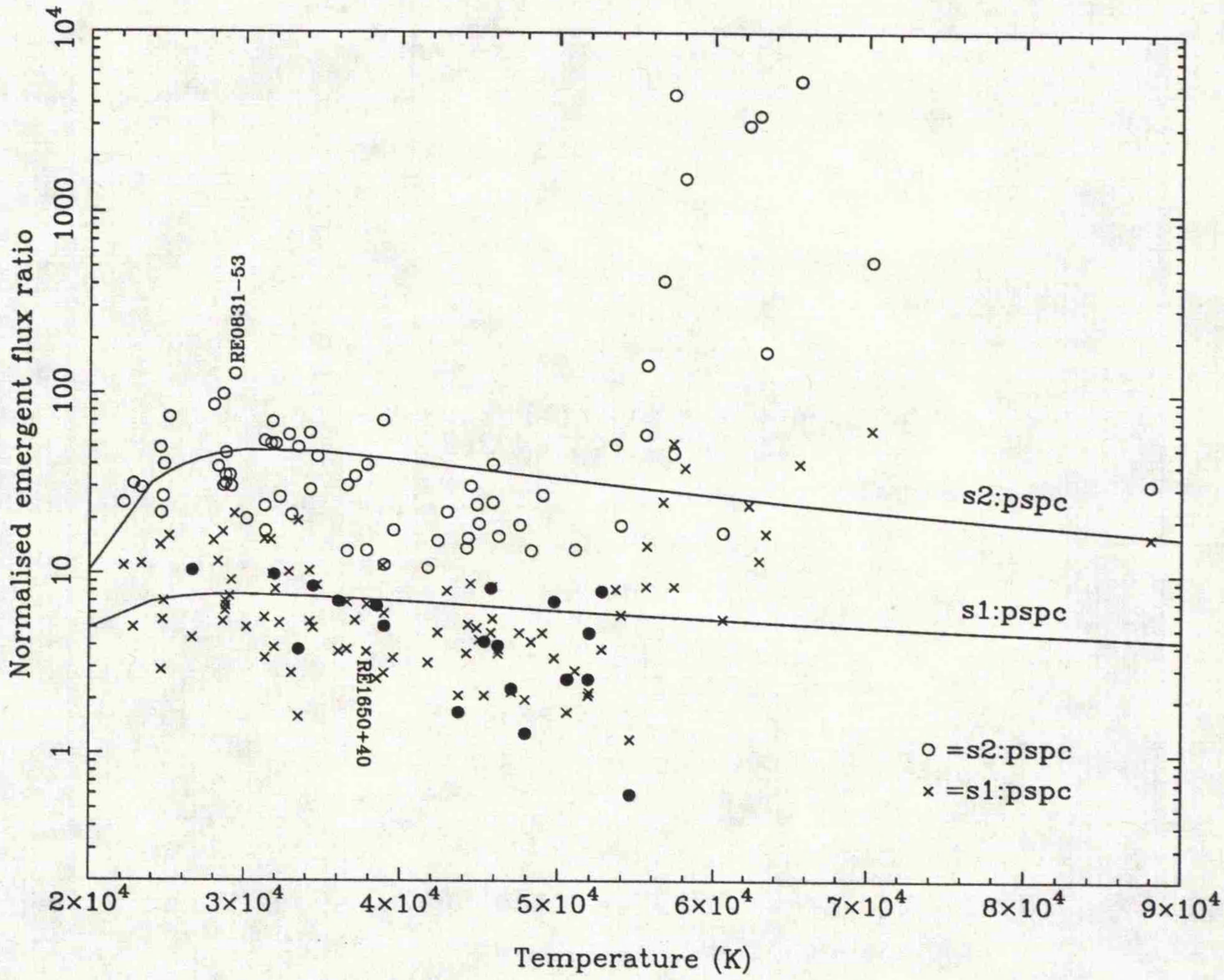

Figure 4.12: Ratio of S2:PSPC and S1:PSPC normalised emergent EUV/X-ray fluxes as a function of temperature. Lines correspond to the predicted ratios for a pure hydrogen atmosphere and HI column of 5×10^{18} cm^{-2} normalised to HZ43. Filled circles are the S2:PSPC ratios for those stars which were not included in subsequent plots due to inferred large column densities.

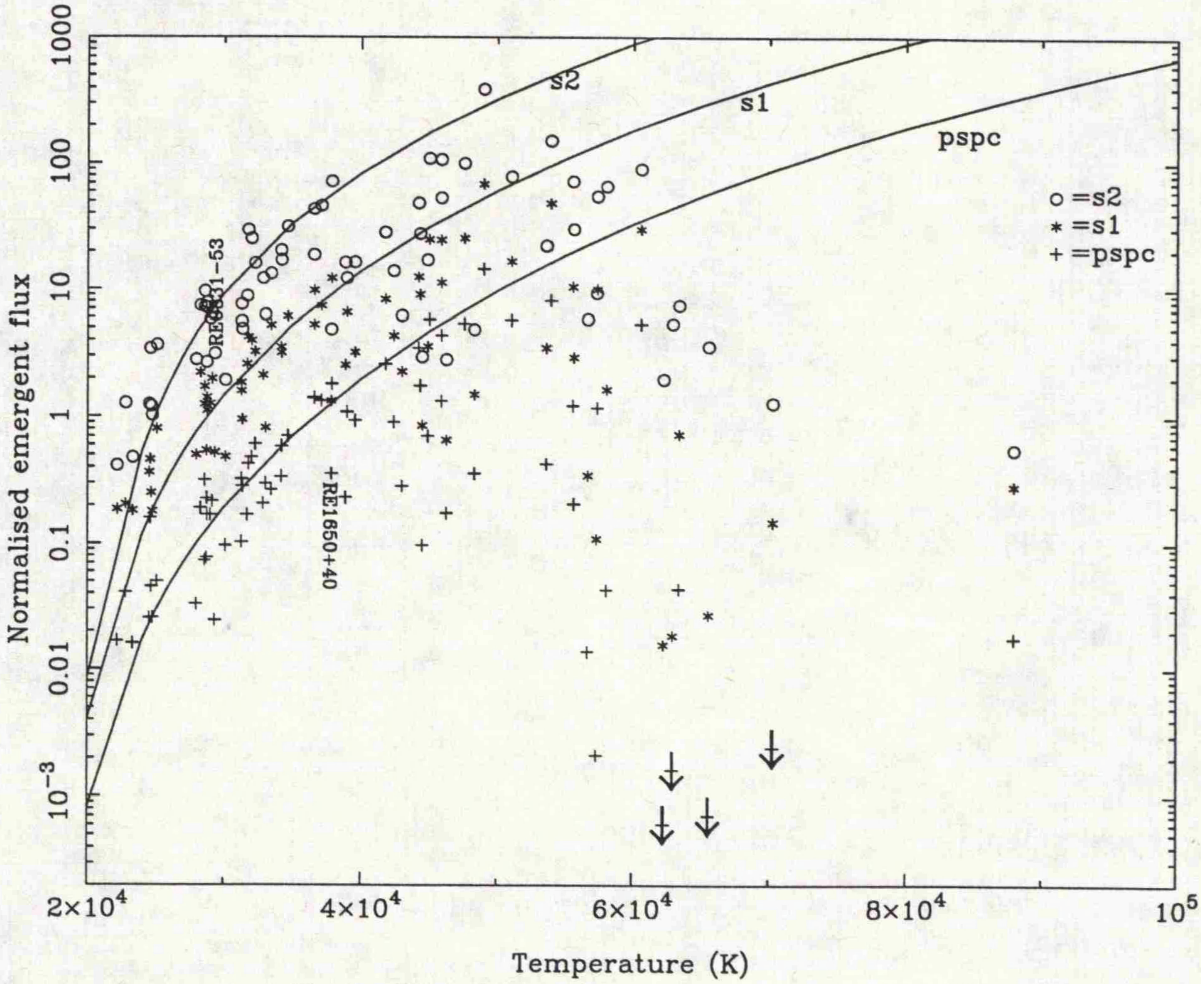

Figure 4.13: Normalised emergent EUV/X-ray fluxes as a function of temperature for the S2, S1 & PSPC survey bands as indicated. Lines correspond to predicted fluxes for a pure hydrogen atmosphere and HI column of 5×10^{18} cm^{-2} for each filter/instrument combination normalised to HZ43. Arrows depict upper limits.

Above $\approx$ 54,000K the flux deficits become very large particularly in the PSPC indicating high levels of photospheric opacity. This contamination is so great that it easily recognisable from the flux ratios.

4.8.1 Temperature and Gravity Dependence

In order to show more clearly how the levels of photospheric opacity vary with temperature, figure 4.14 shows the ratios of the PSPC fluxes (which are least sensitive to HI column) to the predicted fluxes if the atmosphere were assumed to be pure hydrogen, now including uncertainties in temperature. The pure hydrogen model fluxes were calculated individually for each object for its given temperature, gravity and m_v. In all cases the interstellar HI density was set to zero. In using only the best fit temperatures and gravities to calculate the pure hydrogen model, errors (be they small) are introduced into the flux ratios. This may account for objects such as RE2207+25 at 24,610K having ratios higher than 1.0. Figure 4.14 demonstrates very clearly how the opacity increases above 40,000K and then steepens dramatically above $\approx 54,000$K with several stars only having upper limits in the PSPC. Of these most extreme objects, RE0623-37, RE2214-49, Feige 24 and G191-B2B have been observed with the IUE satellite (Holberg *et al.* 1993; Vennes *et al.* 1992b) and show many heavy element features including numerous transitions due to Fe. More recently, Werner & Dreizler (1994) and Holberg *et al.* (1994) have reported the presence of significant quantities of Ni in the UV spectrum of these four objects. These iron group elements have a large EUV radiation cross-section due to their very large number of available transitions and can therefore provide substantial EUV opacity. Chayer, Fontaine & Wesemael (1995) predict that significant amounts of Fe species (Fe/H $\sim 10^{-4}$), can only be levitated against a surface gravity of $\approx$ 7.5 above 50,000K – 60,000K. From this it may be inferred that the large decrease in flux above 54,000K may be due to the presence of Fe in the photospheres. They also predict the presence of other elements such as C, N, O and Ca in this temperature range (with for example, the abundance of C being at a maximum at 40,000K). However, comparisons with observed abundances appear to be in disagreement with the theory as will be discussed in the final chapter. The fact that the reductions in flux occur at distinct temperatures suggests that possibly only a few species may be responsible for the effect.

Another interesting feature of figure 4.14 is the dispersion in the levels of opacity seen at a given T_{eff}. This is very small up to 40,000K, beginning to increase above this and then dramatically above 54,000K, suggesting that the abundances of the absorbing material vary quite considerably from star to star.

A possible explanation for the spread in opacity at a constant T_{eff} could be the effect of gravity, with higher gravities competing more effectively against radiation pressure, reducing the abundances of photospheric absorbing material. In order to investigate this, figure 4.15 shows the flux deficits as a function of surface gravity. The theory of radiative levitation predicts that the efficiency of levitating heavy elements against downward gravitational acceleration increases with increasing temperature, as seen in figure 4.14. As the affect appears to become significant above 40,000K only the stars above this temperature are shown. For stars with log g $>$ 8.0 it appears that the levels of opacity are relatively small suggesting that the majority of trace absorbers have settled below the photosphere (although with only four stars in this region no definite conclusion may be drawn). Below log g = 8.0 there does seem to be a weak correlation between the level of opacity and gravity, objects with the lowest gravities (eg. RE2214-49) having the the highest opacites (although these fluxes are only upper limits). However, this may simply be a result of normal evolution where the gravity increases as the star cools. Theoretical work suggests that although the levels of trace absorbers which can be levitated decrease monotonically with increasing gravity, they should not disappear entirely (eg. Vauclair 1989). Hence, the absence of trace elements in some stars is hard to explain.

To test this possibility, figure 4.16 shows effective temperature plotted against surface gravity, showing the evolutionary increase in gravity as the stars cool. There seems to be good agreement between the theoretical models of Wood (1990) and the optically derived stellar parameters. Only in the case of very high mass objects ($\approx$ 1$M_{\odot}$) do large deviations from the model predictions occur. A possible explanation for this could be that these stars are a result of white dwarf mergers, or that the white dwarf has undergone some phase of common envelope evolution with a hidden companion. From this figure it appears that for most masses, and hence gravities, the level of opacity in the photosphere is a function mainly of temperature, with the affect of gravity resulting more from natural evolution. More conclusive proof of this is restricted by the very narrow peak in the DA mass function (see figure 3.5) and the relatively small number

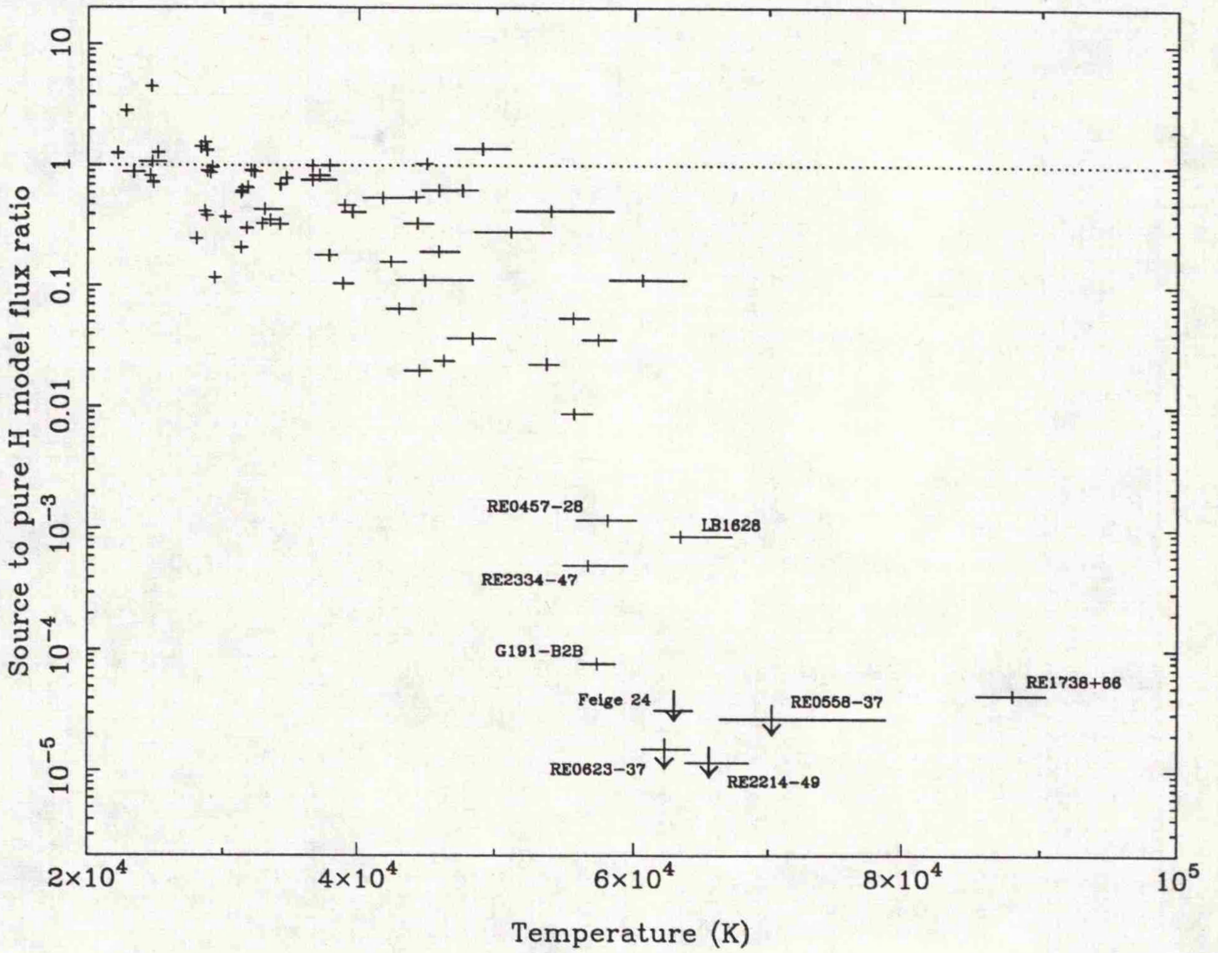

Figure 4.14: Ratio of PSPC normalised emergent fluxes to those predicted for a pure hydrogen atmosphere with zero HI column density as a function of temperature for individual stars. (Each predicted rate was calculated with the same stellar parameters as the star with which the ratio was made). Error bars are on T_{eff} only and arrows depict upper limits. Objects with the largest deficits are indicated.

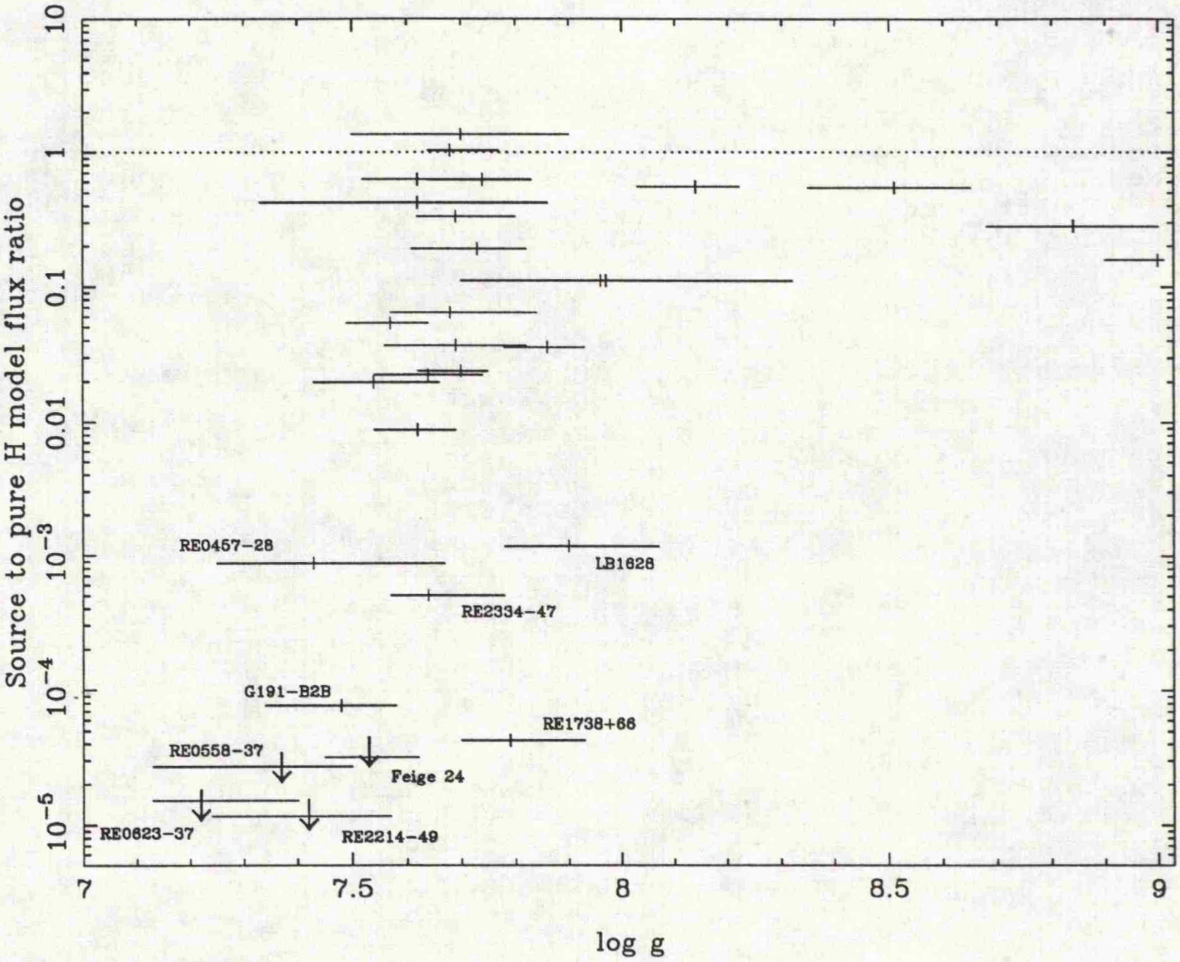

Figure 4.15: Ratio of PSPC normalised emergent fluxes to those predicted for a pure hydrogen atmosphere with zero HI column density as a function of log surface gravity for individual stars hotter than 40,000K. (Each predicted rate was calculated with the same stellar parameters as the star with which the ratio was made). Error bars are on log g only and arrows depict upper limits. Objects with the largest deficits are indicated.

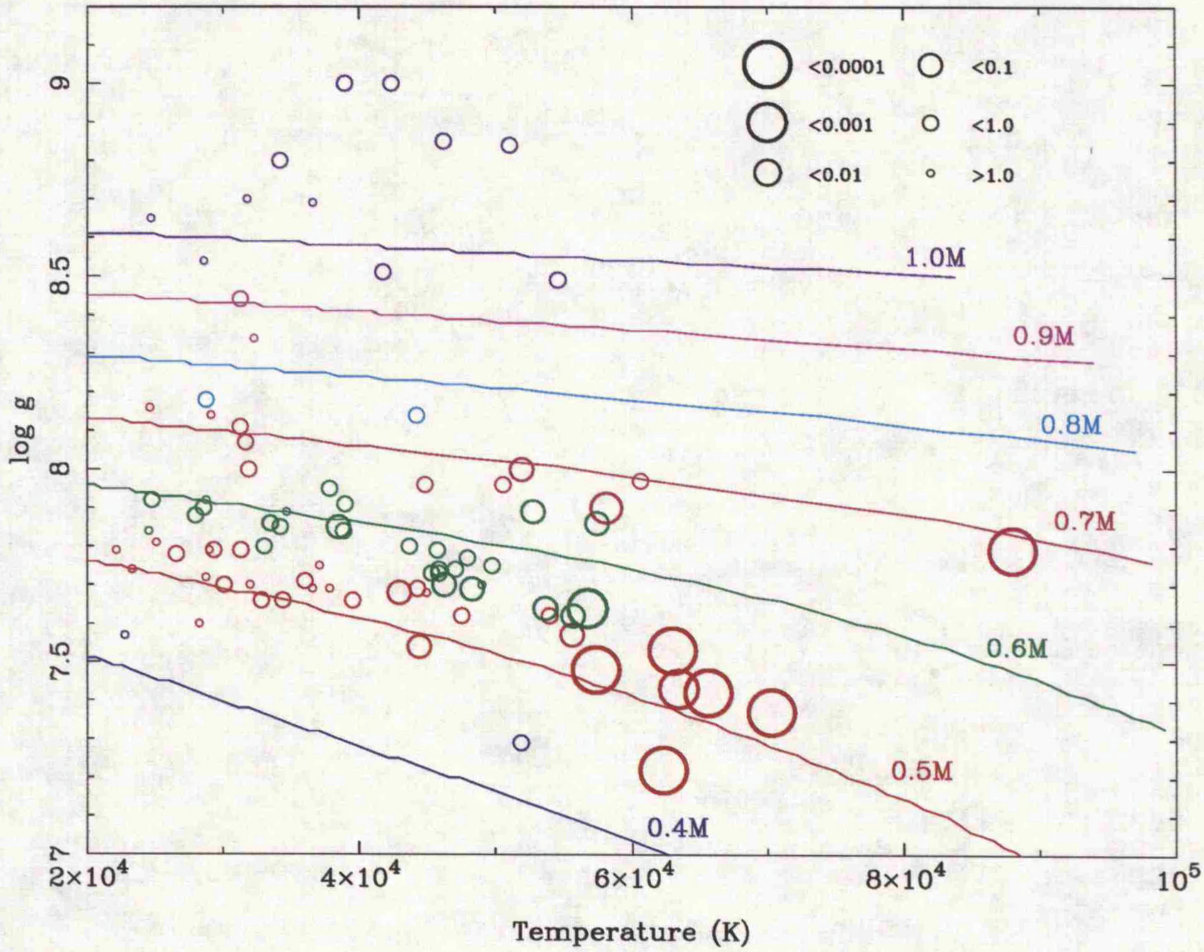

Figure 4.16: Temperature against log surface gravity for all the stars in the sample. The lines correspond to the evolutionary predictions of Wood (1990) for DA's with masses varying from $0.4M_\odot$ to $1.0M_\odot$ as indicated. The size of each circle is proportional to the flux deficit observed in figure 4.6 as indicated. The colour of each circle corresponds to the mass of each object rounded to the nearest $0.1M_\odot$.

of stars in the ROSAT sample.

4.9 Discussion

The results presented here have profound implications for the structure and evolution of DA white dwarfs. With such a large sample it is possible to confirm previous findings but also gain much more detail about the compostion of the DA atmospheres. In this detailed study of 89 ROSAT detections with effective temperatures above 20,000K we find clear evidence that, for the hottest stars, trace photospheric opacity in addition to helium is required to explain the observed EUV/X-ray count rates. Proof of the existence and nature of these trace absorbers has been found in many of these stars from absorption lines arising from elements such as C, N, O, Si, Ni and Fe in the far-UV using IUE. The presence of these elements suggests that many of their EUV bound-bound, bound-free and free-free transitions may significantly affect the ROSAT count rates. With the advent of the EUVE satellite many of these anomalous DAs have now been observed spectroscopically in this waveband and reveal important metal absorption lines which may account for much of the ROSAT flux deficits (Burleigh 1995). One of the most important results is that helium is not a dominant opacity source in any temperature regime. Only 13 objects of the sample of 89 stars require the presence of helium in their atmospheres if it were assumed to be homogeneously mixed and a similar number if the atmospheres were stratified. Two of these stars are the DAOs where helium is definitely present but the remaining DAO RE0720-38 can not be fit by any model atmosphere. This, together with discrepancies between the helium abundances derived from fitting the ROSAT data and the optical HeII line indicate that heavier elements may also be present in these stars. It is only possible to place upper limits on any helium abundances as it is difficult to quantify the role of the heavier elements. However, from the broader picture it seems that helium plays a minimal role in affecting the EUV/X-ray fluxes.

From comparing the emergent fluxes of each star it is obvious that opacity is present in all stars above 50,000K in the form of heavy elements but that the abundances of these elements can vary dramatically from star to star. From $40,000\text{K} - 50,000\text{K}$ the opacity may be accounted for by the presence of helium in several stars. Only two stars in this temperature regime, RE1032+53 and RE1820+58 do not fit any model atmosphere structure. However, these stars do not show the largest flux deficits at these temperatures.

How do these findings compare with existing theories of radiative levitation in DA envelopes? Selective radiative levitation of such elements as mentioned above, against gravitational stratification is much more efficient than it is for helium. This is due to the larger number of transitions possible in these ions giving them a much larger radiative cross-section. Indeed, Vennes *et al.* (1988) demonstrated that the amount of helium that can be radiatively supported in the photosphere was far less than was needed to explain several EXOSAT observations. Various groups have made theoretical calculations demonstrating radiative forces may support significant abundances of these heavier species against gravitational settling, in the abscence of competing processes such as accretion. Morvan, Vauclair & Vauclair (1976), Vauclair (1989) and Chayer, Fontaine & Wesemael (1989) have predicted the equilibrium abundances of C, N, O and Si in DA atmospheres for various temperatures. As an example figure 4.17 shows these abundances as a function of temperature taken from the review by Vauclair (1989) which are in agreement with the other works. These were computed at an optical depth of $\tau = 0.1$ in pure hydrogen atmospheres with a log g $= 8.0$ for a $0.6M_{\odot}$ object following the Koester & Schönberner (1986) evolutionary sequence. It is evident that C, N and O increase monotonically with temperature, whereas the abundance of Si decreases above $50,000$K but is roughly constant down to $30,000$K at a tenth solar abundance. Vauclair also computed abundances for differing values of log g but found that although the abundances do decrease with increasing log g, their sensitivity to gravity does not seem large enough to explain the absence of metals in several high gravity DAs. Chayer, Fontaine & Wesemael (1995) have also considered the levitation of Fe. They find that the abundance of Fe also increases monotonically with increasing temperature but that and observable level cannot be radiatively supported below $\approx 50,000$K for DAs.

This seems to fit in well with the comparison of absolute fluxes from ROSAT. The flux deficits increase dramatically above $54,000$K suggesting an extra absorption component is present, possibly Fe. A combination of absorption from the other elements may account for the reduced flux deficits down to $40,000$K with Si playing an important role in many of the DAs showing a small flux decrement below this temperature. However, the level of dispersion observed in all these temperature ranges is harder to explain. The level of opacity observed and, therefore, the inferred abundance may vary from extreme to practically non-existent for any given

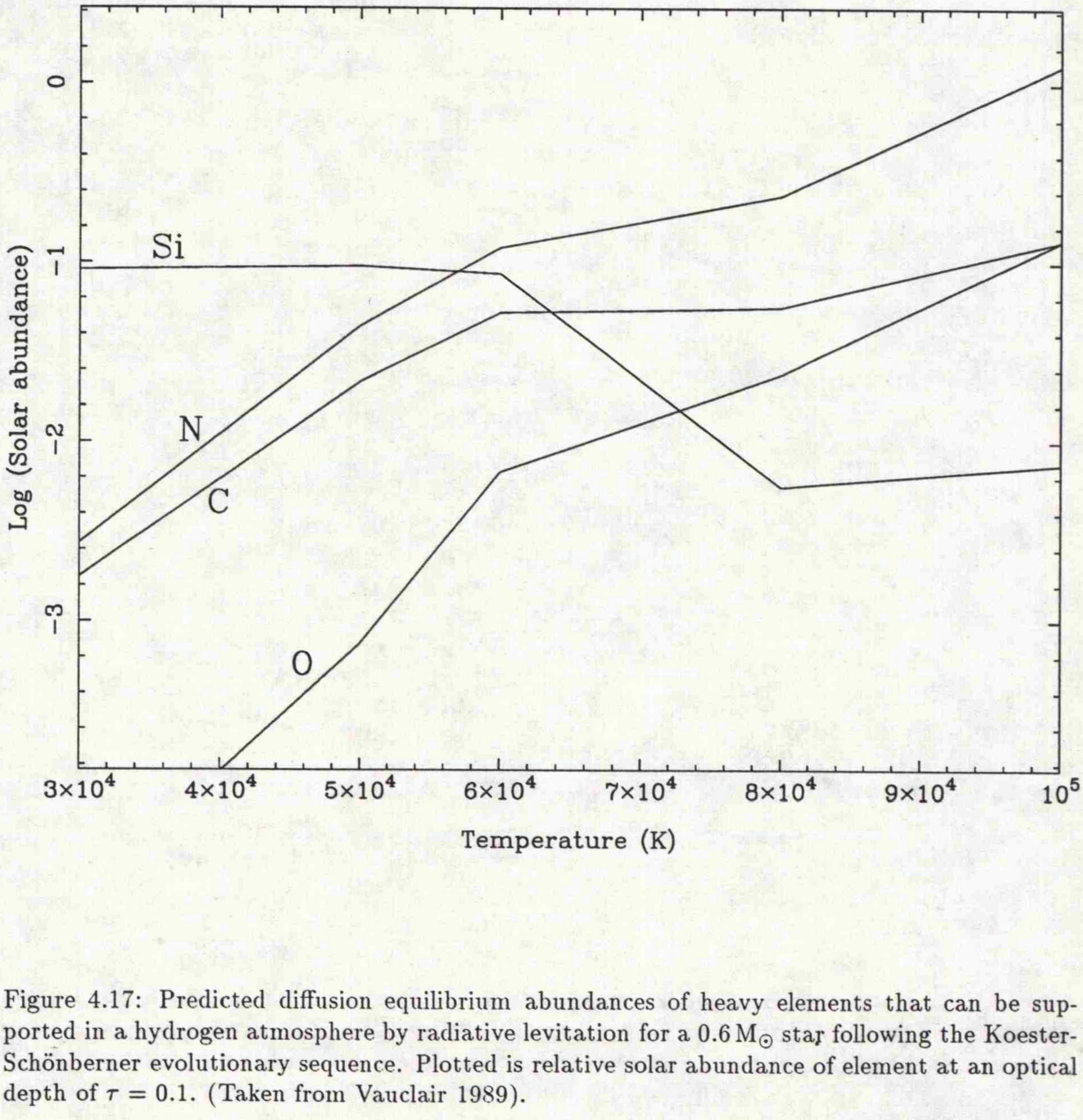

Figure 4.17: Predicted diffusion equilibrium abundances of heavy elements that can be supported in a hydrogen atmosphere by radiative levitation for a $0.6\,M_{\odot}$ star following the Koester-Schönberner evolutionary sequence. Plotted is relative solar abundance of element at an optical depth of $\tau = 0.1$. (Taken from Vauclair 1989).

temperature. How can the heavy element abundance vary so greatly from star to star? All the radiative levitation calculations mentioned above assumed no competing physical processes against radiative upward acceleration other than the downward gravitational acceleration. This must be a simplistic view. In reality, with such high surface gravities, accretion from the interstellar medium may play a significant role. The accretion rate will be determined by the local density of the interstellar material and the surface gravity of the star, with the balance between radiative forces and gravity determining how much of the accreted matter remains visible in the photosphere. However, Vennes *et al.* (1988) conclude that accretion is a minimal contributor. Conversely, with such high effective temperatures, weak stellar winds may be present as has been suggested by Chayer, Fontaine & Wesemael (1989) to explain observed carbon abundances in stars such as Feige 24. Chayer *et al.* (1993) have calculated abundance profiles for various heavy elements including mass-loss, again for a $0.6M_{\odot}$ star. They find that the presence of weak stellar winds (mass-loss of $10^{-16}\ M_{\odot}\ yr^{-1}$) can cause a reservoir of a heavy elements near the surface to disappear after 2800 yr for a $80,000$K star. The abundance profile would then be weakly dependant on the initial mass of the white dwarf. However, the spread in abundances will also be dependent on the initial H layer masses.

4.9.1 Summary

From utilizing the *whole* ROSAT survey a more detailed picture is obtained of the atmospheric structure and composition of hot DA white dwarf atmospheres. Below is a summary of these findings.

1. From the use of H+He model atmospheres it is found that all stars $< 40,000$K which can be successfully modelled are consistent with being pure hydrogen or having a layer mass thick enough that the EUV/X-ray photons originate from pure hydrogen material. However, of the order of 10 objects are also consistent with pure hydrogen with temperatures up to $\approx 55,000$K.

2. If homogeneously mixed, only 13 stars require the presence of helium (two of which are DAO stars). If stratified, a similar number show thin enough layers implying absorption from helium. All these stars are hotter than $40,000$K.

3. It is evident that in general a stratified atmosphere is more realistic, as 13 more stars may be described by this structure compared to a homogeneous one. However, stars that do not fit show no dependence on temperature for either model structure highlighting possible problems with the model calculations. Also, using such a photometric technique it is difficult to distinguish between stratification and heavy element contamination.

4. Irrespective of the nature of the absorbing material there is a clear dependence of opacity with T_{eff}. Below 40,000K the emergent fluxes show a deficit of $0 - 0.1$ that of a pure hydrogen atmosphere. From 40,000K$- \approx 54,000$K this range in deficit becomes $0 - 0.01$ and above $\approx 54,000$K it becomes $0.1 - 10^{-5}$ with the lowest observed fluxes being upper limits.

5. Interestingly, several stars in the 40,000K – 50,000K region are consistent with pure hydrogen atmospheres. This is contrary to the work of B93 and warrents further investigation as radiative levitation predicts significant populations of trace absorbers at these temperatures.

6. This dependence of the level of opacity on T_{eff} reflects radiative levitation calculations for various species. In particular the presence of Fe in the atmospheres above $\approx 50,000$K. Fe has been identified spectroscopically in several of the hotter stars which could not be modelled by H + He atmospheres.

7. There is no strong dependence of opacity with surface gravity. Any dependence present appears to be a result of normal evolution with log g increasing as the star cools.

8. The level of dispersion of opacity for a given temperature suggests that when DAs arrive on the cooling sequence the abundances of heavy elements in the photospheres must differ considerably from star to star. It seems difficult to explain such a large range of extremes without invoking physical effects other than only radiative levitation competing against gravity, possibly convection and/or mass-loss.

9. There are several high mass stars with anomalously high surface gravities. These are possibly a result of extraordinary evolution such as white dwarf merging which may account for them being modelled by unusually thin layer masses (or high helium abundances) for their surface gravities.

Table 4.2: Summary of Homogeneous Fitting Results for which a good fit was obtained (HGI).

Target	χ_r^2	He/H Fraction	1σ bounds	N_H ($\times 10^{19}\,cm^{-2}$)	1σ bounds
RE0003 + 43	1.380	7.110×10^{-8}	$1.000 \times 10^{-8} - 2.790 \times 10^{-6}$	5.150	2.440 - 6.110
RE0007 + 33	0.278	9.400×10^{-7}	$1.000 \times 10^{-8} - 2.370 \times 10^{-4}$	8.100	5.300 - 8.580
RE0053 − 32	2.004	1.000×10^{-8}	$1.000 \times 10^{-8} - 4.410 \times 10^{-8}$	0.552	0.000 - 0.708
RE0138 + 25	1.516	1.000×10^{-8}	$1.000 \times 10^{-8} - 4.660 \times 10^{-6}$	3.837	2.193 - 4.210
RE0148 − 25	1.284	1.000×10^{-8}	$1.000 \times 10^{-8} - 1.010 \times 10^{-5}$	0.000	0.000 - 0.585
RE0237 − 12	0.677	1.000×10^{-8}	$1.000 \times 10^{-8} - 4.190 \times 10^{-5}$	1.390	0.292 - 1.730
RE0322 − 53	1.091	2.260×10^{-5}	$1.000 \times 10^{-8} - 3.180 \times 10^{-5}$	0.008	0.000 - 1.200
RE0350 + 17	3.711	3.440×10^{-5}	$6.140 \times 10^{-6} - 4.330 \times 10^{-5}$	0.000	0.000 - 0.702
RE0512 − 41	0.857	4.730×10^{-6}	$1.000 \times 10^{-8} - 4.470 \times 10^{-5}$	1.550	0.000 - 1.870
RE0521 − 10	1.133	1.000×10^{-8}	$1.000 \times 10^{-8} - 6.180 \times 10^{-6}$	0.000	0.000 - 0.167
RE0550 − 24	1.053	4.120×10^{-8}	$1.000 \times 10^{-8} - 7.080 \times 10^{-7}$	7.290	3.170 - 8.050
RE0552 + 15	2.780	1.000×10^{-8}	$1.000 \times 10^{-8} - 2.440 \times 10^{-6}$	0.047	0.000 - 0.185
RE0605 − 48	2.845	7.830×10^{-5}	$2.220 \times 10^{-6} - 8.950 \times 10^{-5}$	0.000	0.000 - 2.300
RE0632 − 05	3.007	1.500×10^{-4}	$1.000 \times 10^{-8} - 2.700 \times 10^{-4}$	1.160	0.548 - 2.970
RE0645 − 16	1.245	9.910×10^{-7}	$1.000 \times 10^{-8} - 2.420 \times 10^{-5}$	1.080	0.287 - 1.310
RE0654 − 02	3.603	1.000×10^{-8}	$1.000 \times 10^{-8} - 1.860 \times 10^{-5}$	0.800	0.245 - 0.983
RE0715 − 70	0.040	9.460×10^{-7}	$1.000 \times 10^{-8} - 7.500 \times 10^{-6}$	2.450	0.000 - 2.680
RE0723 − 27	1.660	9.860×10^{-7}	$1.000 \times 10^{-8} - 8.380 \times 10^{-6}$	0.738	0.000 - 1.030
RE0902 − 04	2.399	1.000×10^{-8}	$1.000 \times 10^{-8} - 1.430 \times 10^{-5}$	0.475	0.000 - 0.970
RE0907 + 50	0.100	2.720×10^{-5}	$1.000 \times 10^{-8} - 4.380 \times 10^{-5}$	0.000	0.000 - 1.460
RE1019 − 14	3.037	1.010×10^{-4}	$1.000 \times 10^{-8} - 2.230 \times 10^{-4}$	0.479	0.000 - 2.440
RE1024 − 30	0.437	1.670×10^{-6}	$1.000 \times 10^{-8} - 6.980 \times 10^{-5}$	0.871	0.000 - 1.230
RE1029 + 45	0.540	1.330×10^{-7}	$1.000 \times 10^{-8} - 4.220 \times 10^{-5}$	1.210	0.000 - 1.500
RE1036 + 46	0.487	7.430×10^{-6}	$1.000 \times 10^{-8} - 1.460 \times 10^{-5}$	0.087	0.000 - 0.666
RE1043 + 49	0.294	9.350×10^{-5}	$1.000 \times 10^{-8} - 1.530 \times 10^{-4}$	0.221	0.000 - 1.600
RE1044 + 57	1.309	1.000×10^{-8}	$1.000 \times 10^{-8} - 6.220 \times 10^{-6}$	0.696	0.000 - 0.920
RE1100 + 71	3.489	9.620×10^{-5}	$1.000 \times 10^{-8} - 1.300 \times 10^{-4}$	0.000	0.000 - 2.700
RE1112 + 24	4.373	1.000×10^{-8}	$1.000 \times 10^{-8} - 4.480 \times 10^{-5}$	2.600	1.340 - 2.910
RE1128 − 02	4.522	4.570×10^{-5}	$1.000 \times 10^{-8} - 6.220 \times 10^{-5}$	0.000	0.000 - 1.340
RE1257 + 22	1.925	1.000×10^{-8}	$1.000 \times 10^{-8} - 4.210 \times 10^{-8}$	0.332	0.000 - 0.478
RE1316 + 29	2.661	1.000×10^{-8}	$1.000 \times 10^{-8} - 3.750 \times 10^{-5}$	0.478	0.000 - 0.640
RE1431 + 37	0.516	1.000×10^{-8}	$1.000 \times 10^{-8} - 8.990 \times 10^{-6}$	4.200	0.227 - 4.810
RE1623 − 39	0.197	1.340×10^{-6}	$1.000 \times 10^{-8} - 3.070 \times 10^{-6}$	0.000	0.000 - 0.287
RE1638 + 35	3.763	1.000×10^{-8}	$1.000 \times 10^{-8} - 2.500 \times 10^{-5}$	3.790	2.790 - 4.100
RE1650 + 40	0.727	2.350×10^{-4}	$1.000 \times 10^{-8} - 3.190 \times 10^{-4}$	0.124	0.000 - 4.320
RE1726 + 58	0.004	8.150×10^{-4}	$1.000 \times 10^{-8} - 2.780 \times 10^{-3}$	6.590	5.410 - 3.100
RE1800 + 68	0.254	9.080×10^{-8}	$1.000 \times 10^{-8} - 4.790 \times 10^{-5}$	7.190	5.810 - 7.520
RE1847 − 22	0.180	1.150×10^{-5}	$1.000 \times 10^{-8} - 1.590 \times 10^{-4}$	3.530	0.000 - 4.550
RE2009 − 60	3.126	7.010×10^{-5}	$1.000 \times 10^{-8} - 1.020 \times 10^{-4}$	0.897	0.026 - 2.400
RE2018 − 57	2.138	4.980×10^{-7}	$1.000 \times 10^{-8} - 4.490 \times 10^{-5}$	2.190	0.374 - 2.990
RE2024 + 20	0.240	1.360×10^{-4}	$1.000 \times 10^{-8} - 1.220 \times 10^{-3}$	7.240	1.450 - 0.100
RE2029 + 39	2.462	1.000×10^{-8}	$1.000 \times 10^{-8} - 1.390 \times 10^{-5}$	0.555	0.000 - 1.030

Table 4.2: continued

Target	χ^2_r	He/H Fraction	1σ bounds	N_H ($\times 10^{19}\,cm^{-2}$)	1σ bounds
RE2154 − 30	0.045	2.220×10^{-5}	1.000×10^{-8} – 5.360×10^{-5}	0.547	0.000 – 1.780
RE2156 − 41	0.121	1.730×10^{-4}	1.000×10^{-8} – 3.230×10^{-4}	2.140	1.430 – 4.360
RE2156 − 54	2e-5	1.580×10^{-5}	1.000×10^{-8} – 8.990×10^{-5}	0.871	0.000 – 1.540
RE2244 − 32	1.658	3.270×10^{-5}	1.000×10^{-8} – 5.020×10^{-5}	0.000	0.000 – 1.510
RE2353 − 24	2.448	1.000×10^{-8}	1.000×10^{-8} – 2.520×10^{-5}	0.715	0.000 – 1.080
RE0134 − 16	1.961	4.160×10^{-4}	3.710×10^{-4} – 4.600×10^{-4}	0.000	0.000 – 0.141
RE0348 − 00	1.532	6.370×10^{-4}	5.180×10^{-4} – 7.280×10^{-4}	0.333	0.000 – 0.895
RE0550 + 00	1.491	3.780×10^{-4}	2.660×10^{-4} – 4.990×10^{-4}	1.630	0.996 – 2.330
RE0827 + 28	1.991	9.860×10^{-4}	8.850×10^{-4} – 1.450×10^{-3}	0.365	0.170 – 2.420
RE1016 − 05	2.504	7.691×10^{-4}	5.902×10^{-4} – 8.831×10^{-4}	0.748	0.105 – 1.753
RE1340 + 60	0.858	6.680×10^{-4}	4.130×10^{-4} – 7.850×10^{-4}	0.034	0.000 – 2.250
RE1529 + 48	1.149	9.290×10^{-4}	8.930×10^{-4} – 9.590×10^{-4}	0.200	0.054 – 0.493
RE1614 − 08	0.571	6.430×10^{-4}	3.380×10^{-4} – 7.940×10^{-4}	2.000	0.620 – 5.200
RE1746 − 70	1.001	5.770×10^{-4}	3.420×10^{-4} – 6.700×10^{-4}	0.000	0.000 – 0.808
RE2004 − 56	1.302	8.930×10^{-4}	8.110×10^{-4} – 9.620×10^{-4}	0.059	0.000 – 0.576
RE2013 + 40	2e-5	5.741×10^{-4}	3.936×10^{-4} – 7.430×10^{-4}	4.130	2.880 – 5.503
RE2127 − 22	1.179	8.630×10^{-4}	7.870×10^{-4} – 9.160×10^{-4}	0.270	0.062 – 0.748
RE2334 − 47	4.013	9.890×10^{-3}	9.770×10^{-3} – 1.000×10^{-2}	0.026	0.000 – 0.083

Note:
The table is divided into the two subgroups, seperated by a line: The first subgroup are the objects in HGIa (consistent with pure H) and the second are the objects in HGIb (not consistent with pure H).

Table 4.3: Summary of Stratified Fitting Results for which a fit was obtained (SGI).

Target	χ^2_r	M_H ($\times 10^{-13} M_\odot$)	1σ bounds	N_H ($\times 10^{19}$ cm^{-2})	1σ bounds
RE0003 + 43	1.240	0.109	0.055 – 0.311	5.356	4.292 – 6.672
RE0007 + 33	0.272	3.613	2.289 – 27.149	8.175	7.521 – 8.786
RE0053 − 32	1.870	12.727	5.413 – 12.727	0.541	0.405 – 0.697
RE0148 − 25	1.151	4.810	1.347 – 7.667	0.000	0.000 – 0.622
RE0237 − 12	0.001	1.692	0.456 – 1.829	1.607	1.261 – 1.990
RE0512 − 41	0.581	2.246	1.431 – 46.605	1.862	1.547 – 2.119
RE0521 − 10	0.576	0.185	0.126 – 0.604	0.010	0.000 – 0.263
RE0550 − 24	1.054	7.451	1.898 – 63.300	7.263	6.013 – 8.095
RE0552 + 15	0.448	16.396	3.255 – 16.396	0.234	0.109 – 0.384
RE0605 − 48	4.491	1.940	1.140 – 16.424	2.053	1.509 – 2.805
RE0632 − 05	3.583	0.719	0.455 – 1.929	2.514	2.273 – 2.790
RE0645 − 16	1.164	0.627	0.238 – 0.627	1.192	0.998 – 1.401
RE0654 − 02	1.095	2.507	0.873 – 2.507	1.026	0.858 – 1.223
RE0715 − 70	0.030	3.561	1.782 – 31.711	2.607	2.290 – 2.939
RE0723 − 27	1.606	9.032	2.602 – 18.924	0.795	0.535 – 1.077
RE0902 − 04	3.222	5.921	2.238 – 9.105	0.050	0.000 – 0.537
RE0907 + 50	0.042	1.168	0.460 – 2.780	1.143	0.414 – 1.611
RE1019 − 14	4.600	7.389	2.431 – 12.872	2.171	1.811 – 2.567
RE1024 − 30	0.251	0.225	0.140 – 0.691	1.094	0.763 – 1.446
RE1029 + 45	0.569	7.909	1.989 – 14.255	1.185	0.914 – 1.468
RE1036 + 46	0.515	7.958	1.765 – 7.958	0.349	0.174 – 0.548
RE1043 + 49	0.423	5.975	3.204 – 43.451	1.686	1.442 – 1.889
RE1044 + 57	0.759	12.872	2.515 – 12.872	0.791	0.598 – 1.019
RE1100 + 71	5.398	3.125	2.136 – 6.487	2.599	2.207 – 3.008
RE1112 + 24	3.561	14.341	2.075 – 14.341	2.686	2.399 – 2.994
RE1128 − 02	3.163	0.612	0.389 – 1.220	1.250	0.736 – 1.974
RE1257 + 22	0.246	27.605	3.731 – 27.605	0.475	0.328 – 0.628
RE1316 + 29	2.258	12.968	3.415 – 33.812	0.516	0.347 – 0.682
RE1431 + 37	0.471	24.422	2.949 – 24.422	4.251	3.799 – 4.864
RE1623 − 39	0.355	6.263	3.830 – 6.263	0.177	0.015 – 0.365
RE1638 + 35	1.157	11.043	3.808 – 21.195	4.085	3.794 – 4.412
RE1650 + 40	1.491	1.049	0.672 – 12.731	3.407	2.625 – 4.706
RE1726 + 58	0.170	1.897	0.336 – 2.460	11.400	11.400 – 12.360
RE1800 + 68	0.269	8.981	2.115 – 22.608	7.214	6.726 – 7.542
RE1847 − 22	0.312	1.282	0.805 – 7.319	4.447	3.690 – 5.355
RE1943 + 50	5.241	9.422	1.710 – 13.856	4.649	4.135 – 5.271
RE2009 − 60	3.784	2.835	1.163 – 7.542	2.102	1.780 – 2.432
RE2018 − 57	1.931	10.628	1.992 – 10.628	2.296	1.743 – 3.071
RE2024 + 20	1.093	5.732	1.334 – 14.964	7.197	6.129 – 8.295
RE2029 + 39	3.745	5.296	2.470 – 8.009	0.116	0.000 – 0.585

Table 4.3: continued

Target	χ_r^2	M_H ($\times 10^{-13} M_\odot$)	1σ bounds	N_H ($\times 10^{19}$ cm^{-2})	1σ bounds
RE2154 − 30	4e-4	0.126	0.468 − 3.697	1.402	0.898 − 1.856
RE2156 − 41	0.204	2.710	1.927 − 18.910	4.048	3.648 − 4.217
RE2156 − 54	0.016	2.604	1.749 − 27.190	1.378	1.097 − 1.688
RE2244 − 32	1.166	0.757	0.467 − 1.686	0.988	0.481 − 1.751
RE2353 − 24	2.043	4.708	1.107 − 4.708	0.781	0.498 − 1.152
RE0029 − 63	0.618	0.432	0.343 − 0.566	2.528	2.119 − 2.986
RE0108 − 35	1.693	0.942	0.651 − 1.565	0.000	0.000 − 0.397
RE0134 − 16	1.526	0.798	0.697 − 0.943	2.451	2.146 − 2.832
RE0230 − 47	0.686	0.088	0.047 − 0.093	1.358	0.735 − 1.727
RE0235 + 03	0.042	0.025	0.025 − 0.026	0.094	0.050 − 0.151
RE0322 − 53	0.463	1.984	1.085 − 3.960	1.115	0.685 − 1.468
RE0350 + 17	1.194	0.022	0.013 − 0.034	0.852	0.633 − 1.170
RE0348 − 00	0.060	0.002	0.002 − 0.002	2.261	1.753 − 2.826
RE0550 + 00	0.568	1.232	0.923 − 1.631	4.743	4.364 − 4.743
RE0558 − 37	3.372	0.028	0.028 − 0.030	0.814	0.704 − 1.086
RE0827 + 28	4.347	0.210	0.186 − 0.259	6.945	6.106 − 8.351
RE0831 − 53	1.480	0.715	0.398 − 1.232	0.652	0.000 − 1.317
RE1058 − 38	1.972	0.811	0.502 − 1.098	0.567	0.126 − 0.924
RE1126 + 19	1.156	0.190	0.140 − 0.194	0.963	0.642 − 1.190
RE1148 + 18	3.350	0.945	0.549 − 1.173	1.334	0.734 − 1.665
RE1236 + 47	3e-4	0.486	0.392 − 0.649	1.351	0.967 − 1.810
RE1340 + 60	0.338	0.816	0.572 − 1.755	3.172	2.055 − 5.599
RE1529 + 48	2.304	0.516	0.464 − 0.611	4.285	3.669 − 5.197
RE1614 − 08	1.227	1.057	0.816 − 1.859	6.700	5.648 − 6.700
RE1746 − 70	2.217	0.005	0.004 − 0.007	1.318	0.566 − 2.918
RE2004 − 56	0.131	0.788	0.338 − 0.909	3.839	2.229 − 5.081
RE2112 + 50	1.704	0.532	0.441 − 0.674	1.210	0.873 − 1.598
RE2127 − 22	0.749	0.578	0.520 − 0.671	4.375	3.847 − 5.032
RE2312 + 10	0.367	0.265	0.195 − 0.277	1.877	1.463 − 2.130
RE2324 − 54	0.771	1.236	0.870 − 1.540	1.516	1.102 − 1.790
RE2334 − 47	0.617	0.060	0.056 − 0.066	0.419	0.210 − 0.748

Note:
The table is divided into the two subgroups, seperated by a line: The first subgroup are the objects in SGIa (consistent with pure H) and the second subgroup are the objects in SGIb (not consistent with pure H).

Table 4.4: Summary of Objects for which no fits were possible (HGII and SGII).

Target	Model Structure		T_{eff}	log g	Spectral Type	Observed Metals
	Homogeneous: HGII	*Stratified*: SGII				
RE0029 − 63	no fit		60595	7.97	DA	
RE0108 − 35	no fit		28580	7.90	DA	
RE0138 + 25		no fit	38964	9.00	DA	
RE0151 + 67	no fit	no fit	30120	7.70	DA	yes
RE0230 − 47	no fit		63400	7.43	DA	
RE0235 + 03	no fit		62947	7.53	DA	yes
RE0457 − 28	no fit	no fit	58080	7.90	DA	yes
RE0505 + 52	no fit	no fit	57340	7.48	DA	yes
RE0558 − 37	no fit		70275	7.37	DA	
RE0623 − 37	no fit	no fit	62280	7.22	DA	yes
RE0720 − 31	no fit	no fit	53630	7.64	DAO	
RE0831 − 53	no fit		29330	7.79	DA	
RE0841 + 03	no fit	no fit	36605	7.69	DA	
RE1016 − 05		no fit	53650	8.04	DAO	
RE1032 + 53	no fit	no fit	44980	7.68	DA	
RE1033 − 11	no fit	no fit	22790	7.57	DA	
RE1058 − 38	no fit		27970	7.88	DA	
RE1126 + 19	no fit		55640	7.62	DA	
RE1148 + 18	no fit		25107	7.81	DA	
RE1236 + 47	no fit		55570	7.57	DA	
RE1738 + 66	no fit	no fit	88010	7.79	DA	
RE1820 + 58	no fit	no fit	45330	7.73	DA	
RE1847 + 01	no fit	no fit	28744	7.72	DA	
RE1943 + 50	no fit		33500	7.86	DA	
RE2013 + 40		no fit	47057	7.74	DAO	
RE2024 − 42	no fit	no fit	28597	8.54	DA	
RE2112 + 50	no fit		38866	7.84	DA	
RE2207 + 25	no fit	no fit	24610	8.16	DA	
RE2210 − 30	no fit	no fit	28268	7.60	DA	
RE2214 − 49	no fit	no fit	65600	7.42	DA	yes
RE2312 + 10	no fit		57380	7.86	DA	
RE2324 − 54	no fit		45860	7.73	DA	

Chapter 5

Conclusions and Future Prospects

5.1 The ROSAT Sample

Through the use of the ROSAT all sky survey it has been possible to examine the photospheric structure and composition of DA stars across most of the hot DA temperature range ($> 20,000$K). In order to utilize the EUV/X-ray data it was necessary to determine the effective temperature, surface gravity and V magnitude for each of the 89 stars in the sample. Thus, the ROSAT sample is complete down to V$\approx$ 17.0 and is selected purely on the basis of detection in the EUV and soft X-ray regions of the electromagnetic spectrum.

Any biases introduced as a result of such an EUV selection were investigated in chapter 3 by comparing the mass and surface gravity distributions with those of BSL (Bergeron, Saffer & Liebert 1992). The masses were determined using the evolutionary models of Wood (1990) for DA stars with pure carbon interiors and an envelope composition of $\log(M_{He})/M_* = -4$. It was found that the ROSAT sample has a similar mass distribution to that of BSL but with a larger proportion of higher mass stars. These high mass stars were also evident in the surface gravity distribution which showed correspondingly larger numbers of high gravity objects. It is not clear why ROSAT should present a bias toward detection of high mass DAs but through comparison of these objects with the evolutionary models it appears that they are unusual and it was suggested that they may possibly be a result of white dwarf merging. The only other difference between the ROSAT sample and that of BSL was a lower peak (0.1 dex) in the surface gravity distribution. This is due to ROSAT detecting hotter and therefore younger stars than those in

BSL (which has a far lower proportion of hot stars and extends down to $T_{eff} = 13,350$K).

5.2 Atmospheric Structure and Composition

From modelling the ROSAT count rates with H+He models (chapter 4) it is not possible to properly distinguish between a homogeneous and a stratified structure for DA white dwarf atmospheres, the main reason being due to the the photometric nature of the ROSAT data. Considering only known DAs, of the 68 stars which were succesfully modelled by a stratified structure only 54 could also be represented by a homogeneous model with only one DA (RE0138+25) being consistent with a homogeneous atmosphere but not stratified. Although this might suggest that a stratified atmosphere is the more suitable description for the majority of stars, the difficulty in separating the problem of heavy element contamination from that of H/He stratification, which both affect the higher energy bands the most, results in some ambiguity in any conclusions. As an example, RE2334-47 is homegenously modelled with a helium abundance at the model boundary of He/H= 10^{-2}. Such an abundance is obviously unrealistic due to the simultaneous prediction of a strong HeII (4686 Å) line which is not observed. Conversely, a stratified structure with a thin hydrogen layer reproduces the count rates well and does not predict the optical helium line. However, with a temperature of 56,682K this object lies in a region where similar stars have been observed to contain heavy elements which may explain the ROSAT flux deficits (figure 4.13) and which also qualatitively agree with radiative levitation calculations. Until a complete analysis of the EUVE spectrum of this object is performed the result found here must be regarded as preliminary.

The compositional results are broadly similar to those of Barstow *et al.* (1993) and Diamond (1993) where stars below 40,000K are consistent with a pure hydrogen atmosphere while those hotter than this contain some form of opacity with helium apparently making little or no contribution (only 13 stars require the presence of helium if homogeneously mixed). However, due to the larger sample size, it was found that of the order of 10 objects which may be modelled as pure hydrogen are hotter than 40,000K. Previously HZ43 ($T_{eff} = 49,000$K) was thought to be unique in being the only star above 40,000K with a pure hydrogen envelope. When comparing the absolute fluxes from these stars with a pure hydrogen model several show a negligible flux deficit. Follow up spectroscopic observations are required to investigate more thoroughly the possibility of these stars containing no trace helium or heavier elements. Radiative levitation calculations imply that significant abundances of trace elements should be evident in these stars if no other process such as a wind was acting to remove them from the atmosphere.

The improved sample size has also allowed the identification of an absorption component in the atmospheres which only becomes evident above $\approx 54,000$K and has a striking affect on the emergent fluxes. Initial comparisons with radiative levitation theory imply that this is most probably caused by the levitation of iron, which has a large absorption cross-section and can only occur in this temperature range. However, contrary to the predictions of radiative levitation theory, the level of opacity and, therefore, the inferred heavy element abundance does not appear to be strongly dependent on the surface gravity. Interestingly, the dispersion in the observed opacity for stars of this temperature is very large which, together with the hot objects which appear to be pure hydrogen is difficult to explain without invoking some competing physical process such as mass-loss. Although circumstellar features are seen in some DA spectra no detectable winds have been found in DA white dwarfs. Recently however, the 70,000K DO star RE0503-289 has been found to undergo episodic mass outflow Barstow & Sion (1994). If winds are detected in DA white dwarfs the results obtained here will hopefully provide observational constraints against which more refined theoretical predictions of radiative levitation with or without mass-loss can be tested in the future.

5.3 White Dwarf Evolution

The most important parameter in distinguishing white dwarf evolutionary theories is the thickness of the hydrogen layers in DA stars. The mixing theory requires that the layer masses of the majority of DAs should be small ($< 10^{-15}\ M_{\odot}$). As mentioned in chapter 1, one of the cornerstones of this model was the constraint on the layer mass derived from pulsation studies of ZZ Ceti stars. Until the conflict between these results and the recent work by Fontaine *et al.* (1994) which show the pulsations to be independent of layer mass is resolved, analyses of DA spectra with thin hydrogen layer models must be used with a degree of caution.

The analysis of two of the three DAO stars in the ROSAT sample appear to be in agreement with the findings of Bergeron *et al.* (1994) showing the atmospheres to be homogeneous rather than stratified (with neither structure able to represent RE0720-38). Together with the fact that helium appears to be a minimal contributor to the overall photospheric opacity at any temperature and the absence of helium in the EUVE spectra studied by Barstow, Holberg & Koester (1994) of four hot DAs creates a problem in linking the DAs to the related DOs and hybrid DAOs which have clearly visible helium features. It is possible that the timescale for the helium to settle below the photosphere is so short that very few hot DAs which do show opacity from heavier elements will reveal helium.

Of the objects which could be modelled by a stratified structure, all except the unusually high mass stars have $M_H > 10^{-15}$ with the majority having $M_H > 10^{-14}$. Such hydrogen layers are too thick to allow convection to transform the DAs into DBs around 30,000K. However, as it is not possible at this moment to quantify the role of heavier elements this implication is somewhat inconclusive. In keeping with the theory, the thinnest layers are observed in the youngest and therefore hottest stars with a tendency for decreasing layer mass with decreasing temperature. As radiative levitation is at its most efficient at these temperatures it is impossible to measure the layer mass accurately using only H+He model atmospheres. Thus, only when stratified models which include heavier elements can successfully reproduce the fluxes from these objects can the evolutionary questions be properly addressed. This will never be achieved with photometric data of the type obtained by ROSAT due to the large increase in the number of free parameters. However, spectroscopic observations in the EUV such as those taken with the EUVE satellite hold great potential for discovering the precise role of heavy elements in these objects as discussed below.

5.4 The Future

The EUVE observatory was launched in June 1992 with spectrscopic guest observations commencing six months later. The extreme ultraviolet spectrometer covers the wavelength range 70 – 760Å which is split into three using sparate gratings; the short (SW 70 – 190Å), the medium (MW 140 – 380Å) and the long (LW 280 – 760Å) wave bands each with typical spectral reso-

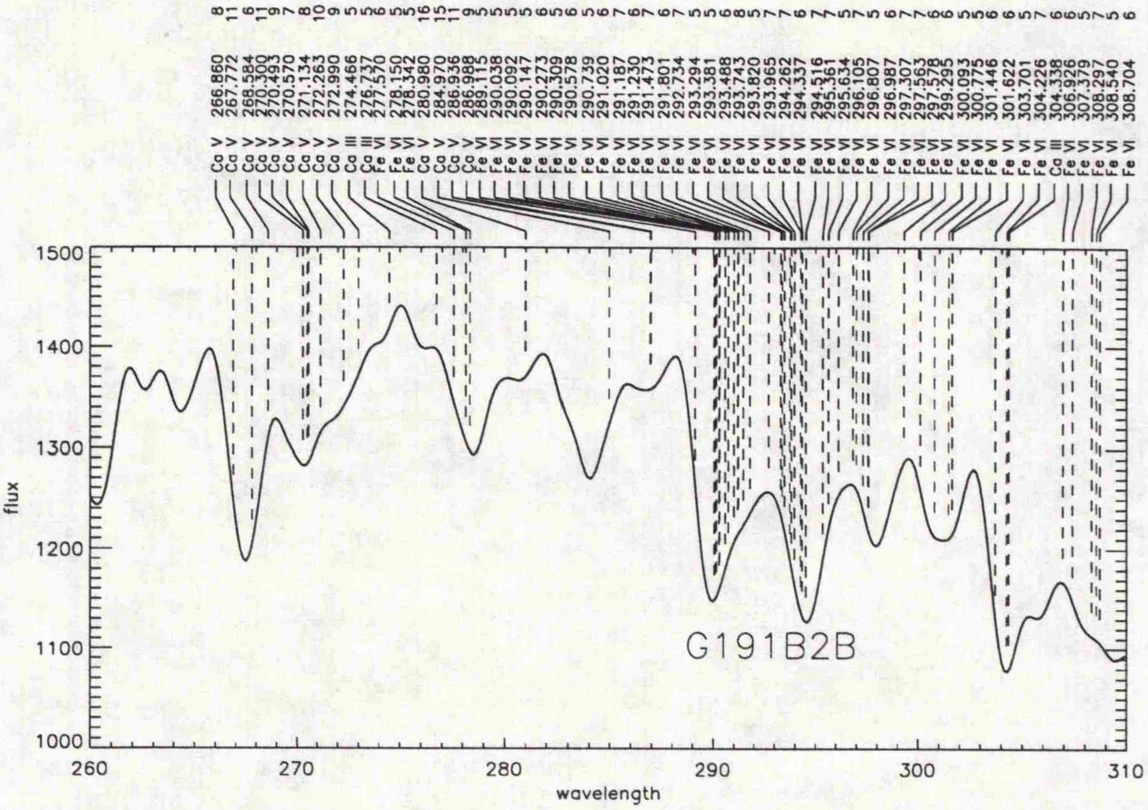

Figure 5.1: EUVE Medium Wave Archive Calibration spectrum of G191-B2B. Shown at the top are the mean laboratory wavelengths of several possible Iron (Fe) and Calcium (Ca) transitions for abundances relative to hydrogen of 10^{-5} expected to produce absorption lines with an equivalent width $\geq$ 5mÅ for the temperature and gravity of this star. From Burleigh (1995)

lutions of 0.5Å, 1.0Å and 2.0Å respectively. The most up-to-date description of the instrument and its performance can be found in the EUVE Episode 2 Guest observer Handbook (EUV 1993).

Several EUVE spectra of bright hot DAs are now available and are being analysed by various groups. Succesful modelling of these spectra requires the inclusion of heavy elements which account for the EUV opacity reported in the work presented here. With the introduction of a much larger number of transitions into the models non-LTE effects are found to be essential for correctly describing the ionisation balance of these elements (Lanz & Hubeny 1995). As a result, the most advanced non-LTE model code 'TLUSTY' developed by Hubeny (1988) and improved by Hubeny & Lanz (1995) is presently being used by the Leicester group to attempt to model the spectral shape besides absorption lines and edges found in the EUVE observations. However, there are problems associated with this work. As there are thousands of possible transitions from many elements in the EUV many of the observed absorption features are formed from blends of different lines. For example, figure 5.1 shows part of a MW calibration spectrum of G191-B2B (Burleigh 1995). Shown at the top of the figure are the mean laboratory wavelengths of possible Fe and Ca lines taken from TLUSTY for abundances relative to hydrogen of 10^{-5} each and for which the equivalent width is expected to be greater than 5mÅ for the temperature and gravity of this star. Bearing in mind that only two elements are included in this figure the problem is readily apparent. Despite this complexity, it is interesting to note that for this spectrum of all the model elements, only Fe has transitions coinciding with the features at 290Å and 295Å.

The approach used is to initially include only those elements which are expected to be found in the temperature range of the object under investigation from radiative levitation calculations and from positive identification from other wavebands. Each element is added to the modelling in turn until the best fit is acheived thereby making the analysis computationally practicable. Of course, in the case of some very hot stars such as G191-B2B all elements are required including Fe. For this reason the models take a very long time to converge on a single solution which may not be unique. However, with improved refinements in the fitting technique interesting results should be available in the very near future.

Appendix A

Model Fitting Technique

A.1 The χ^2 statistic

Determination of the effective temperature and surface gravity of each star (chapter 3) requires modelling the Balmer lines of the optical spectrum. In order to estimate the helium abundance (or hydrogen layer mass) in the white dwarf atmosphere (chapter 4) the ROSAT data must also be succesfully modelled by a synthetic spectrum. In both cases, the method employed to find the most adequate representation of the data was that of minimising χ^2 (see for example Bevington & Robinson 1992).

The χ^2 statistic is given by,

$$\chi^2 = \sum_{i=1}^{N} \frac{(x_i - \nu_i)^2}{\sigma_i^2} \tag{A.1}$$

where x_i are a sample of random variables normally and independently distributed with means ν_i and variances σ_i. The probability density function of this statistic is well documented and is known as the χ^2-distribution for ν degrees of freedom, $f(\chi^2, \nu)$. In the context of model fitting the above equation becomes,

$$\chi^2 = \sum_{i=1}^{N} \frac{(D_i - F_i)^2}{\sigma_i^2} \tag{A.2}$$

where D_i is the number of observed counts in the channel i, F_i is the number of model predicted counts and σ_i^2 is the variance of the counts in channel i. The parameters of the model are adjusted until the value of χ^2 is minimized (χ^2_m) yielding the best model representation of the data. The fit can then be rejected at a certain significance level α, if χ^2_m exceeds the α-point of

Table A.1: Variation of $\chi^2(p, C)$ with number of free parameters p, and confidence C.

Confidence	$\chi^2(p,C)$			
C	$p=1$	$p=2$	$p=3$	$p=4$
0.20 (0.25σ)	0.06	0.45	1.00	1.65
0.68 (1.00σ)	1.00	2.30	3.50	4.70
0.90 (1.60σ)	2.71	4.61	6.25	7.78
0.99 (2.60σ)	6.63	9.21	11.30	13.30

the $f(\chi^2, \nu)$ distribution defined by,

$$\alpha \equiv \int_{\Upsilon}^{\inf} f(\chi^2, \nu) d\chi^2 \tag{A.3}$$

where $\Upsilon = \chi^2(\alpha, \nu)$. (With composite models as used here, N data channels are being modelled by p free parameters giving $\nu = N - p$ degrees of freedom and $\chi_r^2 = \chi^2/\nu$ is the reduced χ^2). The best fit is then only rejected if the χ_m^2 has a value greater than that corresponding to the 10% significance level of the true χ^2 distribution. (i.e. $\chi_m^2 > \chi_T^2(0.1, \nu)$; Lampton, Margon & Bowyer (1976)).

A.2 Error Range Determination

Once a best model fit to the data is achieved it is possible to determine a confidence region for the best fit parameters. To do this the technique of Lampton, Margon & Bowyer (1976) was employed. They used analytical methods to show that for a best fit model with p free parameters and a χ_m^2, for the adjustable parameters to be known to a given confidence C, they must lie within a region of parameter space bounded by $\chi^2 = \chi_m^2 + \Delta\chi^2$ where the values of $\Delta\chi^2$ for various values of p and C are tabulated in table A.1. Therefore in practice, once the best fit is achieved, each free parameter is incremented in turn and a fit made at that value until the value of χ^2 increases by the relevant value in table A.1. This is then taken to be the error range for that parameter to within a certain confidence. This can also be visualised as a process of finding the edges to a confidence region. Consider a model with two free parameters a and b. It is fitted to some data and a best fit is achieved with $\chi^2 = \chi_m^2$. If the parameters are to be known to 68% confidence, the allowed variation in parameter space can be visualised as an ellipse of constant $\chi^2 = \chi_m^2 + 2.3$ (fig A.1). The parameter bounds are then the limits in each

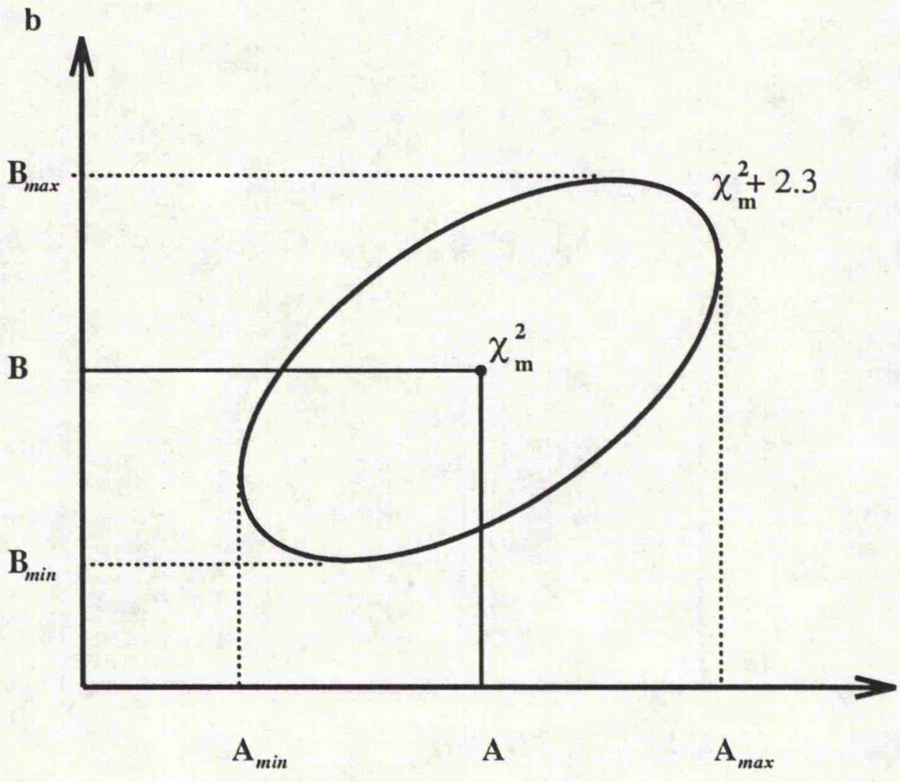

Figure A.1: Schematic of the 1σ confidence region for a model with two free parameters a and b. The centre of the ellipse indicates the best fit values. To know to the parameters to 68% confidence, they must lie within the edges of the projected ellipse.

parameter dimension of the ellipse.

In the work presented here the parameters were stepped until $\Delta\chi^2 = 2.71$ (i.e. 90% confidence for one degree of freedom). However, although there is one degree of freedom in the fitting, there are two 'interesting' free parameters for which an error range is required in both fitting the optical data and the ROSAT data. Therefore this value of $\Delta\chi^2$ actually corresponds to a confidence level of 74% ($\approx 1\sigma$).

References

Aannestad, P. A. & Sion, E. M., 1985. *Astron. J.*, **90**, 1832.

Argyle, R. W., Meyer, C. J., Pike, C. D. & Jorden, P. R., 1988. *A User Guide to the JKT CCD Camera*, ING User Manual XVIII.

Aschenbach, B., 1988. *Applied Optics*, **27**, 1404.

Barstow, M. A. & Pounds, K. A., 1988. In: *Hot thin plasmas in astrophysics*, Pallavicini, R., ed., NATO ASI, p. 359.

Barstow, M. A. & Sansom, A. E., 1990. *Proc. SPIE Int. Soc. Opt. Eng.,*, **1344**, 244.

Barstow, M. A. & Sion, E. M., 1994. *Mon. Not. R. astr. Soc.*, **271**, L52.

Barstow, M. A. *et al.*, 1993. *Mon. Not. R. astr. Soc.*, **264**, 16.

Barstow, M. A., Holberg, J. B., Marsh, M. C., Tweedy, R. W., Burleigh, M. R., Fleming, T. A., Koester, D., Penny, A. J. & Sansom, A. E., 1994. *Mon. Not. R. astr. Soc.*, **271**, 175.

Barstow, M. A. *et al.*, 1995a. *Mon. Not. R. astr. Soc.*, **272**, 531.

Barstow, M. A., O'Donoghue, D., Kilkenny, D., Burleigh, M. R. & Fleming, T. A., 1995b. *Mon. Not. R. astr. Soc.*, **273**, 711.

Barstow, M. A., Holberg, J. B. & Koester, D., 1994. *Mon. Not. R. astr. Soc.*, **268**, L35.

Barstow, M. A., 1989. In: *White Dwarfs*, Wegner, G., ed., Springer-Verlag, Berlin, p. 156.

Barstow, M. A., 1990. *Mon. Not. R. astr. Soc.*, **243**, 182.

Bergeron, P., Wesemael, F., Beauchamp, A., Wood, M. A., Lamontagne, R., Fontaine, G. & Liebert, J., 1994. *Astrophys. J.*, **432**, 305.

Bergeron, P., Saffer, R. A. & Liebert, J., 1992. *Astrophys. J.*, **394**, 228.

Bevington, P. R. & Robinson, D., 1992. *Data Reduction and Error Analysis for the Physical Sciences*, McGraw-Hill.

Böhm-Vitense, E., 1989. *Introduction To Stellar Astrophysics, Volume 2: Stellar Atmospheres,* Cambridge University Press: Cambridge.

Bruhweiler, F. C. & Kondo, Y., 1986. *Astrophys. J.*, **269**, 657.

Burleigh, M. R., 1995. *private communication*, .

Caloi, F., 1989. *Astr. Astrophys.*, **221**, 27.

Chandrasekhar, S., 1931. *Astrophys. J.*, **74**, 81.

Chandrasekhar, S., 1939. *An Introduction To The Study Of Stellar Structure*, Cambridge University Press: Cambridge.

Chayer, P., Pelletier, C., Fontaine, G. & Wesemael, F., 1993. In: *White Dwarfs: Advances in Observation and Theory*, Barstow, M. A., ed., Kluwer, Dordrecht, p. 261.

Chayer, P., Fontaine, G. & Wesemael, F., 1989. In: *White Dwarfs*, Wegner, G., ed., Springer-Verlag, Berlin, p. 253.

Chayer, P., Fontaine, G. & Wesemael, F., 1995. *Astrophys. J. Suppl.*, in press.

Cheselka, M., Holberg, J. B., Watkins, R. & Collins, J., 1993. *Astron. J.*, **106**, 2365.

Cruddace, R., Paresce, F., Bowyer, S. & Lampton, M., 1974. *Astrophys. J.*, **187**, 497.

Diamond, C. J., 1993. *PhD thesis*, University of Birmingham.

Draper, P. W. *CCDPACK - CCD Data Reduction Package.* Starlink User Note 139.2, 1992.

Dreizler, S. & Werner, K., 1993. *Astr. Astrophys.*, **278**, 199.

Drilling, J. & Schönberner, D., 1985. *Astr. Astrophys. Letts.*, **146**, L23.

EUVE Guest Observers Handbook, 2^{nd} edition. EUVE Guest Observer Center, Berkely, 1993.

Finley, D. S., Koester, D. & Basri, G., 1995. in preperation, .

Finley, D., 1988. *PhD thesis*, University of California, Berkeley.

Fleming, T. A., Barstow, M. A., Sansom, A. E., Holberg, J. B., Liebert, J. & Tweedy, R. W., 1993. In: *White Dwarfs: Advances in Observation and Theory*, Barstow, M. A., ed., Kluwer, Dordrecht, p. 155.

Fleming, T. A. *et al.*, 1995. *Astron. J.*, in preperation.

Fleming, T. A., Liebert, J. & Green, R. F., 1986. *Astrophys. J.*, **308**, 176.

Fontaine, G. & Wesemael, F., 1987. In: *Proc IAU Colloq. 95: Conference on Faint Blue Stars*, Hayes, D. S., Liebert, J. & Philip, A. G. D., eds., L.davies Press:Schenectady, p. 319.

Fontaine, G., Brassard, P., Wesemael, F. & Tassoul, M., 1994. *Astrophys. J. Letts.*, **428**, L61.

Fowler, R. H., 1926. *Mon. Not. R. astr. Soc.*, **87**, 114.

Green, R. F., Schmidt, M. & Liebert, J., 1986. *Astrophys. J. Suppl.*, **61**, 305.

Greenstein, J. L. & Sargent, A., 1974. *Astrophys. J. Suppl.*, **28**, 157.

Greenstein, J. L. *Stars and Stellar Systems,* Vol 6, *Stellar Atmospheres*, p. 676. Chicago: University of Chicago Press, 1960.

Greenstein, J. L., 1984. *Astrophys. J.*, **276**, 602.

Greenstein, J. L., 1986. *Astrophys. J.*, **304**, 334.

Hamada, T. & Salpeter, E. E., 1961. *Astrophys. J.*, **134**, 683.

Hardie, R. H. *Astronomical Techniques*, p. 178. University of Chicago Press, 1962.

Heber, U., 1986. *Astr. Astrophys.*, **155**, 33.

Holberg, J. B., Sandel, B. R., Forrester, W. T., Broadfoot, A. L., Shipman, H. L. & Barry, D. C., 1980. *Astrophys. J. Letts.*, **242**, L119.

Holberg, J. B. *et al.*, 1993. *Astrophys. J.*, **416**, 806.

Holberg, J. B., Hubeny, I., Barstow, M. A., Lanz, T., Sion, E. M. & Tweedy, R. W., 1994. *Astrophys. J.*, **425**, L105.

Hubeny, I. & Lanz, T., 1995. *Astrophys. J.*, **439**, 875.

Hubeny, I., 1988. *Comp. Phys. Comm.*, **52**, 103.

Hunger, K., Gruschinske, J., Kudritzki, R. P. & Simon, K. P., 1981. *Astr. Astrophys.*, **95**, 244.

Iben, I. & Macdonald, J., 1985. *Astrophys. J.*, **296**, 540.

Iben, I. & Renzini, A., 1983. *Ann. Rev. Astron. Astrophys.*, **21**, 271.

Iben, I. & Tutukov, A. V., 1984. *Astrophys. J.*, **282**, 615.

Iben, I., 1984. *Astrophys. J.*, **277**, 333.

Johnson, H. L. *Basic Astronomical Data*, p. 204. University of Chicago Press, 1963.

Jordan, S. & Koester, D., 1986. *Astr. Astrophys.*, **65**, 367.

Jordan, S., Koester, D., Wulf-Mathies, C. & Brunner, H., 1987. *Astr. Astrophys.*, **185**, 253.

Kahn, S., Wesemael, F., Liebert, J., Raymond, J. C., Steiner, J. E. & Shipman, H. L., 1984. *Astrophys. J.*, **278**, 255.

Kidder, K. M., 1991. *PhD thesis*, University of Arizona.

Koester, D. & Schönberner, D., 1986. *Astr. Astrophys.*, **154**, 125.

Koester, D. & Weidemann, V., 1980. *Astr. Astrophys.*, **81**, 145.

Koester, D., 1976. *Astr. Astrophys.*, **52**, 415.

Koester, D., 1989. *Astrophys. J.*, **342**, 999.

Koester, D., 1991. In: *Proc. IAU Symp. 145, Evolution of Stars: The Photospheric Abundance Connection.*, Michaud, G. & Tutukov, A., eds., Kluwer, Dordrecht, p. 435.

Lampton, M., Margon, B., Paresce, F., Stern, R. & Bowyer, S., 1976. *Astrophys. J. Letts.*, **203**, L71.

Lampton, M., Margon, B. & Bowyer, S., 1976. *Astrophys. J.*, **208**, 177.

Landolt, A. U., 1983. *Astron: J.*, **88**, 439.

Landolt, A. U., 1992. *Astron. J.*, **104**, 340.

Lanz, T. & Hubeny, I., 1995. *Astrophys. J.*, **439**, 905.

Liebert, J., Dahn, C. C. & Monet, D. G., 1988. *Astrophys. J.*, **332**, 891.

Liebert, J., Wesemael, F., Hansen, C. J., Fontaine, G., Shipman, H. L., Sion, E. M., Winget, D. E. & R, F, G., 1986. *Astrophys. J.*, **309**, 241.

MacDonald, J. & Vennes, S., 1991. *Astrophys. J.*, **371**, 719.

Margon, B., Liebert, J., Gatewood, G., Lampton, M., Sprinrad, H. & Bowyer, S., 1976. *Astrophys. J.*, **209**, 525.

Mason, K. O. *et al.*, 1995. *Mon. Not. R. astr. Soc.*, **274**, 1194.

McCook, G. & Sion, E. M., 1987. *Astrophys. J.*, **65**, 603.

Menzies, J. W., Cousins, A. W. J., Banfield, R. M. & Laing, J. D., 1989. SAAO Circular, **13**, 1.

Michaud, G. & Fontaine, G., 1984. *Astrophys. J.*, **283**, 657.

Morvan, E., Vauclair, G. & Vauclair, S., 1976. *Astr. Astrophys.*, **163**, 145.

Napiwotzki, R. & Schönberner, D., 1991. In: *White Dwarfs.*, Vauclair, G. & Sion, E., eds., Kluwer, Dordrecht, p. 39.

Napiwotzki, R., Barstow, M. A., Fleming, T. A., Holweger, H., Jordan, S. & Werner, K., 1993. *Astr. Astrophys.*, **278**, 478.

Napiwotzki, R., 1995. In: *White Dwarfs.*, Koester, D. & Werner, K., eds., Springer-Verlag, p. 132.

Paczynski, B., 1970. *Acta. Astron.*, **20**, 47.

Paerels, F. B. S. & Heise, J., 1989. *Astrophys. J.*, **339**, 1000.

Page, C. G. *NIPS: New Image Point Search Program.* University of Leicester X-ray Astronomy Group, 1990.

Petre, R., Shipman, H. L. & Canizares, C. L., 1986. *Astrophys. J.*, **304**, 356.

Pfeffermann, E. *et al.*, 1987. *Proc. SPIE Int. Soc. Opt. Eng.,*, **733**, 519.

Pounds, K. A. *et al.*, 1993. *Mon. Not. R. astr. Soc.*, **260**, 77.

Pye, J. P., McGale, P. A., Allen, D. J., Barber, C. R., Bertram, D., Denby, M., Page, C. G., Ricketts, M. J., Stewart, B. C. & West, R. G., 1995. *Mon. Not. R. astr. Soc.*, **274**, 1165.

Reimers, D. & Koester, D., 1982. *Astr. Astrophys.*, **116**, 341.

Reimers, D., 1981. In: *Physical Processes in Red Giants*, Iben, I. & Renzini, A., eds., Dordrecht:

Reidel, p. 269.

Renzini, A. & Voli, M., 1981. *Astr. Astrophys.*, **94**, 175.

Rumph, T., Bowyer, S. & Vennes, S., 1994. *Astron. J.*, **107**, 2108.

Schatzmann, E., 1958. *White Dwarfs*, Amsterdam: North Holland.

Schönberg, A. & Chandrasekhar, S., 1942. *Astrophys. J.*, **96**, 161.

Schönberner, D., 1983. *Astrophys. J.*, **272**, 708.

Shafer, R. A., Haberl, F., Arnaud, K. A. & Tennant, A. F., 1991. *XSPEC Users Guide: ESA TM-09*, ESA Publications Division, Noordwijk.

Shapiro, S. L. & Teukolsky, S. A., 1983. *Black Holes, White Dwarfs and Neutron Stars: The Physics of Compact Objects*, New York: Wiley.

Shipman, H. L., Thejll, P., Bhatia, S. & Liebert, J., 1991. In: *White Dwarfs.*, Vauclair, G. & Sion, E., eds., Kluwer, Dordrecht, p. 229.

Shipman, H. L., Liebert, J. & Green, R., 1987. *Astrophys. J.*, **315**, 239.

Shipman, H. L., 1976. *Astrophys. J.*, **206**, L67.

Shipman, H. L., 1989. In: *White Dwarfs.*, Wegner, G., ed., Springer-Verlag, Berlin, p. 220.

Sims, M. R. *et al.*, 1990. *Opt. Eng.*, **26**, 649.

Sion, E. M., Greenstein, J. L., Landstreet, J., Liebert, J., Shipman, H. L. & Wegner, G., 1983. *Astrophys. J.*, **269**, 253.

Sion, E. M., 1984. *Astrophys. J.*, **282**, 612.

Thorstensen, J. R., Vennes, S. & Bowyer, S., 1995. *Astrophys. J.*, in press.

Trümper, J., 1984. *Physica Scripta*, **T7**, 209.

Tweedy, R. W., Holberg, J. B., Barstow, M. A., Bergeron, P., Grauer, A. D., Liebert, J. & Fleming, T. A., 1993. *Astron. J.*, **105**, 1938.

Vauclair, G. & Reisse, C., 1977. *Astr. Astrophys.*, **61**, 415.

Vauclair, G., 1989. In: *White Dwarfs*, Wegner, G., ed., Springer-Verlag, Berlin, p. 176.

Vennes, S. & Fontaine, G., 1992. *Astrophys. J.*, **401**, 288.

Vennes, S., Pelletier, C., Fontaine, G. & Wesemael, F., 1988. *Astrophys. J.*, **331**, 876.

Vennes, S., Chayer, P., Fontaine, G. & Wesemael, F., 1989. In: *White Dwarfs*, Wegner, G., ed., Springer-Verlag, Berlin, p. 373.

Vennes, S., Chayer, P., Thorstensen, J. R., Bowyer, S. & Shipman, H. L., 1992a. *Astrophys. J. Letts.*, **392**, L27.

Vennes, S., Chayer, P., Thorstensen, J. R., Bowyer, S. & Shipman, H. L., 1992b. *Astrophys. J.*, **392**, L27.

Vennes, S., Thejll, P. & Shipman, H., 1991. In: *White Dwarfs*, Vauclair, G. & Sion, E., eds., Kluwer, Dordrecht, p. 235.

Weidemann, V. & Koester, D., 1983. *Astr. Astrophys.*, **121**, 77.

Werner, K. & Dreizler, S., 1994. *Astr. Astrophys.*, **286**, L31.

Wesemael, F., Auer, L. H., Horn, H. M. V. & Savedoff, M. P., 1980. *Astrophys. J. Suppl.*, **43**, 159.

Wesemael, F., Green, R. & Liebert, J., 1985. *Astrophys. J. Suppl.*, **58**, 379.

Wesemael, F., Henry, R. C. & Shipman, H. L., 1984. *Astrophys. J.*, **287**, 868.

Wilkinson, E., Green, J. C. & Cash, W., 1992. *Astrophys. J. Letts.*, **397**, L51.

Willingale, R., 1995. *Mon. Not. R. astr. Soc.*, in preperation.

Winget, D. E., Robinson, E. L., Nather, R. E. & Fontaine, G., 1982. *Astrophys. J. Letts.*, **262**, L11.

Winget, D. E. *et al.*, 1987. *Astrophys. J. Letts.*, **315**, L77.

Winget, D. E., 1993. In: *White Dwarfs: Advances in Observation and Theory*, Barstow, M. A., ed., Kluwer, Dordrecht, p. 449.

Wolter, H., 1952. *Opt. Eng.*, **10**, 94.

Wood, M. A., 1990. *PhD thesis*, University of Texas At Austin.

Wood, M. A., 1992. *Astrophys. J.*, **386**, 539.

Zombeck, M. V., 1990. *Handbook of Space Astronomy and Astrophysics*, Cambridge University Press, Cambridge.